FINAL ISSUE

REACTOR MATERIALS

A Quarterly Technical Progress Review

Prepared for DIVISION OF TECHNICAL INFORMATION, U. S. ATOMIC ENERGY COMMISSION,
by BATTELLE MEMORIAL INSTITUTE, COLUMBUS LABORATORIES

Fall 1970

● VOLUME 13

INDEX ISSUE ● NUMBER 3

TO THE READERS

We regret to announce that economic necessities compel us to terminate *Reactor Materials* with this issue.

In order that its coverage of the field of reactor materials will not be completely abandoned, AEC has arranged to have Battelle Memorial Institute prepare a review article on the subject for each quarterly issue of *Reactor Technology,* beginning with the Fall 1970 issue, Vol. 13, No. 4.

Reactor Materials has made a significant contribution to the progress of nuclear technology. To the editors and to the staff members of Battelle Memorial Institute who have assisted them during the past 13 years, I wish to express my appreciation and that of the AEC for a job consistently well done.

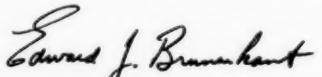

Edward J. Brunenkant, *Director*
Division of Technical Information

REACTOR MATERIALS

Vol. 13, No. 3 Fall 1970

Contents

Metallurgy of Common Cladding and Structural Materials (Section I)	Specialized Reviews	107
	Zirconium Alloys	107
	Stainless Steels	109
	Nickel-Base Alloys	110
	Pressure-Vessel Steels	111
Metallurgy of Refractory Metals (Section II)	Niobium Alloys	114
	Creep of Refractory Alloys	115
	Molybdenum Alloys	116
	Tungsten Alloys	116
	Vanadium-Base Cladding Alloys	117
Diffusion Studies (Section III)	Diffusion in Nuclear Fuels	118
	Diffusion in Refractory Metals	118
	Diffusion in Structural Metals and Miscellaneous Metallic Systems	120
	Diffusion of Interstitials and Gases in Metals	121
Radiation Effects in Structural Materials (Section IV)	Stainless Steels and Nickel Alloys	124
	Pressure-Vessel Steels	126
	Miscellaneous Alloys	127
	Basic Mechanisms of Radiation Damage in Nonfuel Materials	129
Nonfueled Refractories (Section V)	Structural Ceramics	132
	Niobium Carbide	132
	Rare-Earth Oxides	132
	Concrete	133
Corrosion of Base-Metal Alloys in Aqueous and Gaseous Media (Section VI)	Reviews and Miscellaneous Studies	135
	Corrosion of Aluminum	135
	Corrosion of Ferrous Alloys	135
	Corrosion of Nickel-Base Alloys	137
	Corrosion of Zirconium Alloys	137
Oxidation of Refractory Metals (Section VII)	Oxidation of Uncoated Refractory Metals	139
	Protection of Refractory Metals by Coating	140

Corrosion by Liquid Metals and Fused Salts (Section VIII)

Corrosion by Sodium 143
Corrosion in Rankine-Cycle Space Power Systems 148
Solubility of Materials in Liquid Metals 149
Liquid-Metal Corrosion Review 149
Containment of Molten Uranium Fuels . . 150
Corrosion by Fused Fluoride Salts 150

Cladding Behavior in Loss-of-Coolant Accidents (Section IX) 153

Index Volume 13 155

Superintendent of Documents, U. S. Government Printing Office, Washington, D. C. 20402

REACTOR MATERIALS

has been published for the past 13½ years under the auspices of the USAEC Division of Technical Information, as one of a series of progress-review periodicals covering various aspects of nuclear technology. Owing to technical-publication budget restrictions, *Reactor Materials* is being discontinued with this issue.

To the readers of this journal, the Editors extend sincere appreciation for your interest. Also, to those of you who have expressed regret at losing the journal, we would like to point out that publication of the remaining three Technical Progress Reviews (see back cover) will continue and that *Reactor Technology* will contain frequent articles dealing with reactor materials.

E. M. Simons
D. L. Keller

BATTELLE MEMORIAL INSTITUTE
COLUMBUS LABORATORIES

Issued by the U. S. Atomic Energy Commission. Use of funds for printing this publication approved by the Director of the Bureau of the Budget on May 12, 1969.

TECHNICAL PROGRESS REVIEWS

The United States Atomic Energy Commission publishes the Technical Progress Reviews to meet the needs of industry and government for concise summaries of current nuclear developments. Each journal digests and evaluates the latest findings in a specific area of nuclear technology and science. *Nuclear Safety* is a bimonthly journal; the other two are quarterly journals.

Isotopes and Radiation Technology
P. S. Baker, A. F. Rupp, and associates
Isotopes Information Center, Oak Ridge National Laboratory

Nuclear Safety
Wm. B. Cottrell, W. H. Jordan, J. P. Blakely, and associates
Nuclear Safety Information Center, Oak Ridge National Laboratory

Reactor Technology
Prepared in cooperation with the American Nuclear Society

All are available from the U. S. Government Printing Office. See the back cover for ordering instructions.

NOTICE

This journal was prepared under the sponsorship of the U. S. Atomic Energy Commission. Neither the United States nor the U. S. Atomic Energy Commission, or any of their employees, contractors, subcontractors, or their employees, makes any warranty, express or implied, or assumes any legal liability or responsibility for the accuracy, completeness, or usefulness of any information, apparatus, product, or process disclosed, or represents that its use would not infringe privately owned rights.

Availability of Reports Cited in This Review

United States Atomic Energy Commission (USAEC) reports are available at certain libraries that maintain collections of these reports. They are also sold by the following governmental and international organizations: (1) Clearinghouse for Federal Scientific and Technical Information (CFSTI), U. S. Department of Commerce, Springfield, Va. 22151 ($3.00 for printed copy and $0.65 for microfiche); (2) International Atomic Energy Agency (IAEA), Vienna, Austria; and (3) National Lending Library, Boston Spa, England.

Other U. S. Government agency reports identified in this journal are generally available from CFSTI.

Reports from other countries are available at some libraries in the United States and from IAEA and the originating country. **United Kingdom Atomic Energy Authority (UKAEA)** reports are sold by Her Majesty's Stationery Office, London. **Atomic Energy of Canada Limited (AECL)** reports are sold by the Scientific Document Distribution Office, Atomic Energy of Canada Limited, Chalk River, Ontario, Canada. UKAEA and AECL reports issued after March 1, 1967, are sold by CFSTI to purchasers in the United States and its territories.

Private-organization reports should be requested from the originator.

The views expressed in this publication do not necessarily represent those of the United States Atomic Energy Commission, its divisions or offices, or of any Commission advisory committee or contractor.

Section

I

Reactor Materials

Metallurgy of Common Cladding and Structural Materials

By M. Kangilaski

SPECIALIZED REVIEWS

Thermal–Mechanical Treatment

The Defense Metals Information Center (DMIC) has reviewed the available Soviet literature on thermal–mechanical treatment of metals. The report[1] presents theoretical aspects of thermal–mechanical treatment as well as specific data on alloy steels, stainless steels, nickel-base alloys, titanium alloys, aluminum alloys, copper alloys, and refractory metals.

LMFBR Component Materials

A comprehensive report[2] on the limitations and requirements of component materials for liquid-metal-cooled fast breeder reactor (LMFBR) applications has been issued. Major materials requirements identified were associated with the need for mechanical-property design data; the problems and materials limitations resulting from corrosion and mass transfer in sodium; the evaluation and selection of wear-resistant materials for guide, bearing, and seal applications; the development of techniques to weld reliable tube-to-tube-sheet joints; and the radiation-induced swelling and ductility loss of structural materials exposed to a fast-neutron-flux environment.

ZIRCONIUM ALLOYS

The proceedings of the American Society for Testing and Materials (ASTM) conference on zirconium held in Philadelphia in November 1968 have been published[3] as ASTM Special Technical Publication No. 458. This book is a collection of 25 papers on zirconium and its alloys. The specific topics covered include: texture, fabrication and properties, engineering properties, corrosion, hydriding, and general testing techniques. Zircaloys and Zr–Nb alloys for use as fuel-cladding and pressure-tube materials for nuclear reactors were discussed at a British seminar.[4] The discussions covered creep, radiation growth, yield phenomena, hydride precipitation, corrosion, and metallurgical problems encountered in processing. The elastic, short-term tensile, creep, and fatigue properties of Zircaloy-2, Zircaloy-4, Zr–2.5 Nb, and Zr–2.5 Nb–0.5 Cu have been reviewed by the Canadians as a guide for design purposes.[5]

In Yugoslavia the effect of cooling rate (up to 500°C/sec) on transformation temperature and on the room-temperature structure of Zircaloy-2 was investigated.[6] A continuous cooling diagram consisting of two curves was constructed from the data obtained by thermal analysis. Within the upper curve region, the products of the transformation reaction are grain-boundary alpha precipitates and Widmanstätten alpha plates. In the region of the lower curve, the transformed structure resulting from slow cooling consists of Widmanstätten alpha plates and an intermetallic precipitate distributed mainly between the plates. It was assumed that the transformation that takes place at intermediate cooling rates ultimately occurs as a bainitic reaction. Products of this reaction are always mixed with the martensitic phase, which appears in the form of fine, preferentially oriented alpha plates clustered into colonies.

The effects of texture on the mechanical properties of Zircaloy tubing have been shown to be significant.[7] A relation has been established which allows one to predict the final texture based on various independently controllable fabrication variables. The parameters considered are reduction in area (R_A); reduction in outside diameter (R_{OD}); reduction in wall thickness (R_W); and reduction in inside diameter (R_{ID}), together with Q ratio (R_W/R_{ID}) and D ratio (inside diameter/outside diameter). Combinations of these parameters control all reductions and size changes that the tubing undergoes during a fabrication sequence, and a graphical method is used to correlate the above parameters. It was found experimentally that preferential wall thinning (ironing, or increasing D ratio) produces a sheet rolling texture; preferential diameter reduction (sinking, or decreasing D ratio) produces a basal-poles-tangential texture; and equal amounts of the two (constant D ratio) produce a fiber texture.

It was found that Zircaloy becomes extremely brittle when exposed to steam at high temperatures (which would be expected to occur following a loss-of-coolant accident).[8] Tests were made by exposing reactor-grade Zircaloy-2 in 2-in.-long tubes (0.634-in. outside diameters with 30-mil wall thicknesses) to steam at various times and temperatures. After exposure the specimens were tested in compression in the diametral direction, and the results are shown in Fig. I-1. Metallographic examination of the

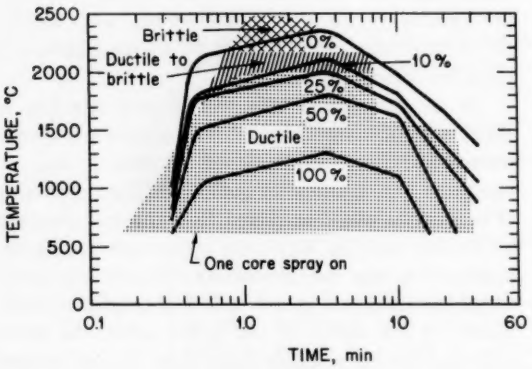

Fig. I-1 Zircaloy embrittlement behavior superimposed on fuel rod time–temperature profiles for spray cooling of the Browns Ferry boiling-water reactor (percentages refer to percent of rods above the indicated temperature).[8]

exposed tubes indicated that the embrittlement was due to pickup of considerable oxygen when the specimens were held in steam above the alpha → beta transformation temperature (862°C).[9]

Both uniaxial tensile tests and biaxial tube-burst tests were performed at Bettis[10] on recrystallized Zircaloy tubing at temperatures ranging from room temperature to 1900°F (1035°C). Some results of these tests are shown in Fig. I-2. It appears that a reasonable estimate of biaxial yield behavior can be obtained from uniaxial tests. Above about 800°F (425°C), a slight strengthening effect was noted with increasing pressurizing rate in the biaxial tests.

Canadian investigators measured the amounts of hydride precipitated in the grain boundaries and in the matrix of annealed Zircaloy as a function of quenching temperature.[11] It has been shown that as the quenching temperature is decreased, both intergranular and intragranular precipitation increase. However, below 150°C quenching temperature, precipitation within the grains ceases and all further precipitation is intergranular.

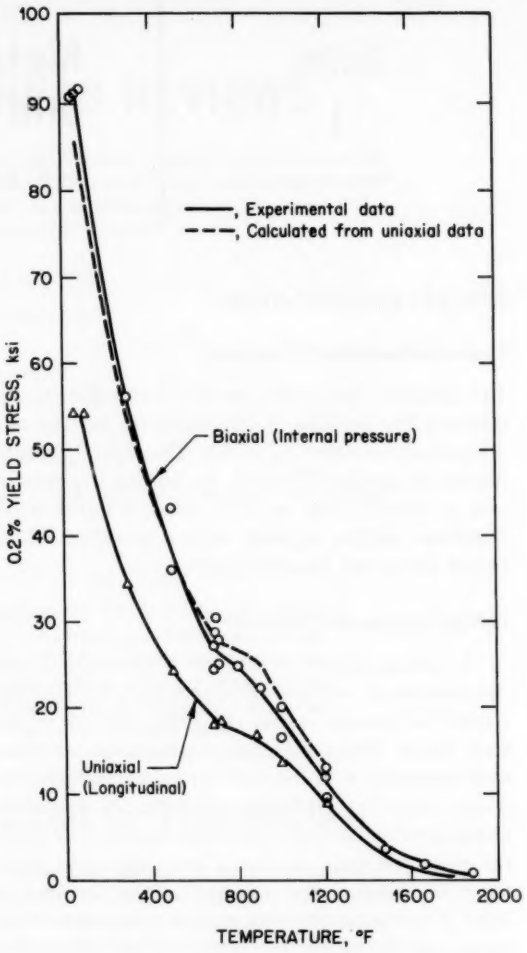

Fig. I-2 Yield strength of recrystallized Zircaloy-4 tubing under uniaxial and biaxial stresses.[9]

It has been found that the crystallographic orientation of zirconium hydride platelets in fine-grained Zircaloy tubing can be determined by microhardness impressions.[12] When the basal plane of a grain is parallel to the polished surface, a spherical indentor produces a circular impression. However, if the basal plane tilts out of the surface, the impression takes on an oval shape with the major axis coinciding with the trace of the basal plane in the surface.

Cracking in end-cap welds of Zircaloy-2-sheathed UO_2 fuel pins was found[13] to be caused by excessive hydrogen contamination near the welds. Density changes associated with the resulting massive hydrides cause stresses severe enough to crack the welds.

In a study of the effect of rolling temperature on the texture of Nb–2.5 Zr, it was found[14] that the final texture developed depended on:

1. The relative amounts of the alpha- and beta-zirconium phases present during deformation.

2. The deformation modes in each phase.

3. The crystallographic relation between any deformed beta-zirconium phase and its transformation product.

If the cold work was done at room temperature, the majority of the grains had their basal planes parallel to the plane of the sheet. However, if the rolling was done at a temperature where a large amount of the material was in the beta phase, the majority of the grains had their basal planes transverse to the plane of the sheet.

Canadian investigators have compared[15] the mechanical properties of Ozhennite 0.5 (Zr–0.2 Sn–0.1 Fe–0.1 Ni–0.1 Nb) with those of Zircaloy-2. Ozhennite 0.5 exhibited somewhat lower strength than Zircaloy-2, but its ductility was significantly higher at all testing temperatures. Room-temperature tensile properties of four new zirconium-base alloys are given in Table I-1.[16] Soviet investigators[17] found that the combined addition of 4 to 5 wt.% of tantalum and vanadium to zirconium results in a reduction in creep rate by a factor of 10 in the temperature range 400 to 700°C. Optimum creep properties were obtained in the alloy containing 2.5 wt.% each of tantalum and vanadium.

French investigators[18] found that the presence of the niobium in a Zr–8 Nb alloy causes the body-centered beta phase to be partially preserved at room temperature. Thus the alloy would contain the hexagonal omega and alpha phases along with the body-centered beta phase.

The results of an X-ray parametric study[19] of the solid solubility of aluminum in zirconium, shown in Fig. I-3, suggest that the solubility is significantly higher than previous studies have indicated.

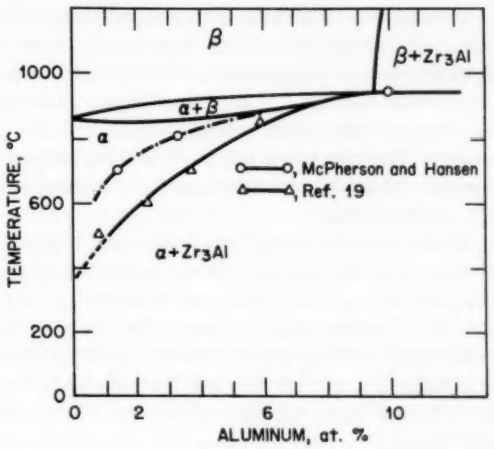

Fig. I-3 Solvus curve in the Zr–Al system.

STAINLESS STEELS

Burst tests were performed by General Electric[20] at 1100 and 1300°F (595 and 705°C) on thin-walled 316 stainless-steel tubes to evaluate the effects of both artificial and natural defects. The following conclusions were drawn:

1. The orientation of the defect is important, with longitudinal defects causing rupture at the defect and circumferential and diagonal defects having no influence on the location of tube failure.

2. The rupture strength is not substantially reduced, even by defects as deep as 25% of the tube-wall thickness.

3. Ductility at rupture is significantly reduced by longitudinal defects.

Table I-1 Room-Temperature Mechanical Properties of Zirconium-Base Alloys[16]

Alloy	Hydrogen content, ppM	Grain size, ASTM No.	Ultimate strength, kg/mm²	0.2% offset yield strength, kg/mm²	Elongation in 4 in., %
Zr–1.2 Cu–0.3 Fe	18	10*	48	34	17
Zr–0.7 V–0.75 Fe	19	11*	54	45	14
Zr–2.5 Nb–0.5 Ta	17	10*	48	36	20
Zr–0.2 Sn–0.09 Fe–0.07 Ni–0.14 Nb	7	9†	34	22	24

*Deformed structure. †Fully annealed structure.

It has been established that nondestructive ultrasonic critical-angle reflectivity tests can be used to determine the relative amount of cold work in 316 stainless-steel tubing.[21] Figure I-4 illustrates the relation among cold work, critical angle, and microhardness. The major advantages of this technique are its speed, accuracy, and independence of variations in physical dimensions.

Workers at Oak Ridge[22] used planetary swaging to produce 316 stainless-steel tubes having an average grain size of only 2 μ. The extensive network of grain boundaries in this material should provide sinks for vacancies produced during irradiation. The annihilation of vacancies before they can agglomerate into voids is expected to minimize swelling of stainless steel during irradiation.

Workers at General Electric[23] investigated hot hardness, tensile and creep-rupture strength, and bend and impact ductility of Fe–Cr–Al–Y alloys. The alloys studied had chromium contents of 5 to 24 wt.%, aluminum contents of 4 to 6 wt.%, and yttrium contents of 0.77 to 1.46 wt.%. It was found that significant improvements in strength and creep properties could be obtained by the solid-solution additions of Mo, Nb, W, or Ta. However, it was concluded that the strength properties of all the alloys were inferior to those of 304 stainless steel at all testing temperatures. Because of their good oxidation resistance, it appears that the use of these alloys should be limited to applications involving low stresses in an oxidizing atmosphere at temperatures of 950 to 1200°C.

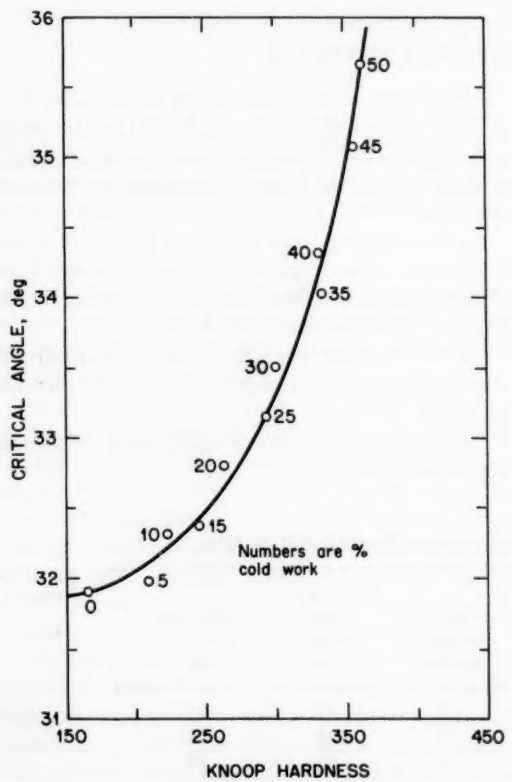

Fig. I-4 Correlation of cold work and microhardness of 316 stainless steel with critical ultrasonic reflectivity angle.[21]

NICKEL-BASE ALLOYS

The addition of titanium to Hastelloy N, followed by a long heat-treatment at 650°C, results in precipitation of fine MC particles at or near the grain boundaries.[24] Such precipitates have a decidedly greater strengthening effect than do M_2C precipitates within the grains. Table I-2 illustrates the improvement in creep properties of Hastelloy N with increasing titanium content.

Table I-2 Effect of Titanium Content on the 40,000-Psi, 650°C Stress-Rupture Properties of Hastelloy N (Ref. 24)

Titanium content, wt.%	Rupture life, hr	Creep rate, %/hr	Fracture strain, %
0.15	26–217	0.005–0.09	5.7–13.7
0.30	41–515	0.004–0.08	6.4–27.6
0.45	125–850	0.006–0.097	6.5–42.1
1.2	1200–2470	0.004–0.02	21.0–54.0

The precipitation behavior of Inconel 625 solid-solution hardened by molybdenum and niobium was investigated.[25] At temperatures between 550 and 750°C, fine precipitates of the tetragonal-phase $Ni_3(Nb,Al,Ti)$ segregate, and the result is increased hardness and strength. This phase is metastable. After prolonged times at temperatures above 650°C, it overages to $Ni_3(NbMo)$ with an orthorhombic structure and an acicular shape. Overaging is accompanied by an increase in creep rate, whereas hardness and yield strength are less influenced by overaging. In alloys without aluminum and titanium, there is no tetragonal $Ni_3(Nb,Al,Ti)$ phase to precipitate. Consequently such alloys exhibit nearly no hardness increase after exposure at high temperatures and less creep strength than alloys with aluminum and titanium additions.

Tungsten was found[26] to influence the precipitation and transformation behavior of gamma prime in Ni–Cr alloys. Increasing the tungsten content was found to retard the transformation of metastable gamma prime (Ni_3Ti) to the stable eta (Ni_3Ti). The presence of tungsten also suppressed the formation of M_7C_3 and increased the tendency toward $M_7C_3 \rightarrow M_{27}C_6$ reaction.

The nickel-base superalloy Inconel 718 has several unique strength characteristics, but conflicting reports exist as to the nature of the strengthening precipitate in this material.[27] A comprehensive study of its principal precipitates was therefore conducted using dark-field electron microscopy and electron and X-ray diffraction. It was shown that the major strengthening phase in this alloy was a disk-shaped body-centered tetragonal (bct) (DO_{22}) precipitate rather than the face-centered cubic (Ll_2) gamma prime found in most nickel-base superalloys. The latter phase was detected but in smaller quantities. On exposure to moderately high temperature (650 to 815°C), both precipitate phases coarsened, but the bct phase was still predominant. After 16 hr at 870°C, the gamma prime was taken into solution, whereas the remaining bct phase coarsened further. It appears that the deterioration of properties above ~650°C resulted from coarsening and partial solution of the two ordered phases. Fully heat-treated samples that were deformed both at room temperature and at elevated temperatures exhibited planar deformation banding, a slip mode characteristic of nickel-base superalloys.

Studies have shown that Ni_3Nb precipitation behavior follows a predictable pattern with increased strain. Additional studies were initiated[28] to further the understanding of Ni_3Nb precipitation under strain conditions, as well as the effects of such conditions on the stability of gamma prime and the formation of sigma or other phases often considered detrimental to performance. Samples of Inconel 718 from a production heat were treated above the Ni_3Nb precipitation range and subsequently strained between zero and 35% reduction of area at 815°C. Light and electron microscopy and X-ray diffraction studies were performed on samples in the as-strained condition; after a 950°C gamma-prime solution treatment; after a 950°C treatment followed by a double aging, gamma-prime precipitation treatment; and after a fully aged plus 675°C, 500-hr exposure. It was found that the quantity of Ni_3Nb which precipitated during the 950°C treatment step increased markedly with the degree of strain, that gamma-prime stability is not significantly affected by either strain or the quantity of Ni_3Nb precipitate, and that sigma and similar phases do not form during prolonged exposure at the upper end of the useful temperature range for this alloy, even at the highest strain level investigated.

Uniform, fine grain size is generally preferred in forgings of Alloy 718 for optimum properties.[29] However, owing to limitations imposed by forging equipment, forging size, and forging configuration, it is often impossible to produce this desired grain size. Instead, some grain duplexing or grain coarsening occurs in certain areas throughout the forging. Stress-rupture tests were conducted before exposure and after exposing specimens at 675°C and 50,000 psi or 705°C and 50,000 psi for 500 hr. Three types of specimens were used: uniform fine grain size (ASTM 7 or finer), duplex grain size, and uniform coarse grain size (ASTM 5 or coarser). These grain sizes were obtained in forgings with a simple pancake configuration using varying forging techniques. The results of the rupture tests conducted before exposure showed an excellent correlation with grain size. After exposure, rupture ductility increased and strength decreased owing to overaging. In duplexed samples the controlling factor appears to be the amount and size of the coarse grain. The optimum grain size for the best balance of rupture properties appears to be ASTM 6 or 7.

A detailed study has been made[30] of the effect of boron on the structure and the properties of the austenitic alloy Fe–42 Ni–16 Cr–3 Mo–1.5 Ti–1.25 Al. It was found that boron improves the stress-rupture life by decreasing the minimum creep rate, by delaying the appearance of tertiary creep, and by increasing the strain in this last stage of creep. Structural studies on boron-doped specimens showed differences in the form of the deformation in regions adjacent to the creep fracture. The final morphology of the precipitated grain-boundary carbides was not modified by the presence of boron, but its effect was to slow down precipitation. The growth of the gamma-prime phase $Ni_3(Ti,Al)$, which causes the structural hardening, was also measured.

PRESSURE-VESSEL STEELS

It has been demonstrated that two newly developed Swedish steels 2RM2 (13 Cr–6 Ni–0.06 C) and 2RM0 (13 Cr–6 Ni–1.5 Mo–0.06 C) have ideal properties for nuclear pressure vessels.[31] These steels have high yield strengths, low ductile-to-brittle transition temperatures, and good resistance to irradiation embrittlement. Because of their low carbon content, the steels are also easily weldable.

The notched high-strain behavior of carbon steel, 2.25 Cr–1 Mo steel, and 304 stainless steel at both room temperature and 290°C was investigated by General Electric.[32] Of the three steels the stainless steel exhibited the greatest change between room temperature and 290°C in its low-cycle-fatigue properties. The tensile properties and life-to-crack initiation of notched specimens decreased as the temperature was increased. The strain-controlled, smooth-bar, low-cycle-fatigue life improved at the higher temperatures, but the average crack growth rate measured on notched bars with load control increased. The low-cycle-fatigue crack initiation and growth properties of 2.25 Cr–1 Mo alloy steel were essentially constant between room temperature and 290°C. Crack initiation in carbon steel occurred at a lower number of cycles at 290°C than at room temperature. The effect was larger at high stresses than at lower stresses.

Load-controlled push–pull and bending low-cycle-fatigue tests were conducted in Japan on ASTM A-302B steel under room and elevated temperatures in order to investigate the effect of mean stress on low-cycle-fatigue deformation behavior.[33] This phenomenon is considered to be an important factor in the design of nuclear reactors, steam turbine casings, and chemical equipment because in these devices cyclic stress or strain is superposed on a stationary stress, and deformation of structural members progresses in the stationary-stress direction as a result of each stress repetition. This phenomenon is similar to thermal-stress ratcheting. It was found that low-cycle-fatigue deformation could be evaluated by the increment of mean strain during one cycle of stress and strain repetition. Low-cycle-fatigue deformation increased with mean stress and stress amplitude. Push–pull stresses produced almost 50% greater low-cycle-fatigue deformation than did the same stresses applied in reversed bending.

REFERENCES

1. J. G. Dunleavy and J. W. Spretnak, Soviet Technology on Thermal–Mechanical Treatment of Metals, Report DMIC-Memo-224, Defense Metals Information Center, Battelle–Columbus, Nov. 15, 1969.
2. A. A. Bauer and J. G. Conner, A Survey of LMFBR Component Materials Limitations and Requirements, USAEC Report BMI-1901, Battelle–Columbus, January 1970.
3. *Application Related Phenomena in Zirconium and Its Alloys,* Proceedings of ASTM Conference, Philadelphia, Pa., November 1968, American Society for Testing and Materials, Special Technical Publication No. 458, 1969.
4. J. H. Gittus, Zirconium Discussion, *J. Inst. Metals,* **97**: 60-63 (February 1969).
5. Atomic Energy of Canada Limited, unpublished data.
6. D. Drobnjak, The Kinetics of Transformation and Structural Changes in Zircaloy-2 During Continuous Cooling, *Bull. Boris Kidric Inst. Nucl. Sci., Ceram. Met.,* **19**(4): 35-43 (September 1968).
7. D. O. Hobson, Texture Control in Zircaloy Tubing, *Trans. Amer. Nucl. Soc.,* **12**(2): 571-572 (November 1969).
8. R. Herzel and R. H. Meservly, The Brittle Behavior of Zircaloy Under Emergency-Core-Cooling Conditions, *Trans. Amer. Nucl. Soc.,* **12**(1): 356-357 (June 1969).
9. M. J. Graber and W. F. Zelezny, Metallurgical Evaluation of Zircaloy Exposed to Emergency-Core-Cooling Conditions, *Trans. Amer. Nucl. Soc.,* **12**(1): 355-356 (June 1969).
10. C. C. Busby and K. B. Marsh, High Temperature Deformation and Burst Characteristics of Recrystallized Zircaloy-4 Tubing, USAEC Report WAPD-TM-900, Westinghouse Electric Corp., Bettis Atomic Power Laboratory, January 1970.
11. Atomic Energy of Canada Limited, unpublished data.
12. J. J. Kearno, Micro-Sphere Probe of the Crystallographic Orientation of Hydrides in Fine-Grained Zircaloy Tubing, *J. Nucl. Mater.,* **33**: 114-118 (1969).
13. A. S. Bain, Mechanism Causing Hydride Defects at End-Cap Welds of Zircaloy-Sheathed UO_2, *Trans. Amer. Nucl. Soc.,* **12**(1): 99-100 (June 1969).
14. B. A. Cheadle, S. A. Aldridge, and C. E. Ells, The Effect of Temperature During Deformation on the Development of Texture in Zirconium Alloy Rolled Sheet, *J. Nucl. Mater.,* **34**: 119-124 (January 1970).
15. M. G. Wright, Short Term Mechanical Properties of Ozhennite 0.5, Canadian Report AECL-3287, April 1969.
16. Research Establishment, Risø, Denmark, Metallurgy Department Annual Progress Report for Period Ending March 31, 1969, Danish Report RISØ-199, May 1969.
17. E. M. Tararayeva and O. S. Ivanov, Properties of Zirconium Alloys with Ta and V (in Russian), *Izv. Akad. Nauk SSSR, Metal.,* No. 4: 170-179 (1968).
18. P. Van Effenterre, G. Cizeron, and P. Lacombe, Study of the Structural Transformations in the Zirconium–Niobium Alloy Containing 8 Wt. Percent Nb, *J. Nucl. Mater.,* **31**: 269-278 (July 1969).
19. S. N. Tiwari and K. Tangri, The Solid Solubility of Aluminum in α-Zirconium, *J. Nucl. Mater.,* **34**: 92-96 (January 1970).
20. T. Lauritzen, A. Montes, and A. Conti, The Influence of Surface Defects on Short-Term Mechanical Properties of Austenitic Stainless Steel Tubing, USAEC Report GEAP-13550, General Electric Company, Breeder Reactor Development Operation, December 1969.
21. F. L. Becker and R. L. Trantow, Nondestructive Evaluation of Cladding Cold Work and Grain Size, *Trans. Amer. Nucl. Soc.,* **12**(2): 540 (November 1969).
22. G. A. Reimann and W. R. Martin, Improved Processes for the Fabrication of 316 Stainless-Steel Tubing, *Trans. Amer. Nucl. Soc.,* **12**(2): 567-570 (November 1969).
23. J. L. Bartas, R. J. Perkins, and F. C. Robertshaw, Mechanical Properties of Fe–Cr–Al–Y Alloys, USAEC Report GEMP-711, General Electric Company, Missile and Space Division, July 1969.

24. C. E. Sessions, R. E. Gehlbach, S. W. Cook, and H. E. McCoy, Correlation of the Creep Behavior of a Nickel Alloy with Precipitate Distribution, *Trans. Amer. Nucl. Soc.*, **12**(2): 570-571 (November 1969).
25. F. Garzarvolli, A. Gerscha, and K. P. Francke, Investigations on the Precipitation Behavior and the Mechanical Properties of the Alloy Inconel 625 (in German), *Z. Metallk.*, **60**: 643-652 (August 1969).
26. A. Havalda, Influence of Tungsten on the γ' to η Transformation and Carbide Reactions in Nickel-Base Superalloys, *ASM, Trans. Quart.*, **62**: 581-589 (September 1969).
27. D. F. Paulonis, J. M. Oblak, and D. S. Duvall, Precipitation in Nickel-Base Alloy 718, *ASM, Trans. Quart.*, **62**: 611-622 (September 1969).
28. R. S. Cremisio, The Effect of Thermomechanical History on the Stability of Alloy 718, *J. Metals*, **21**: 55-61 (November 1969).
29. J. P. Stroup and R. A. Heacox, Effect of Grain Size Variations on the Long Time Stability of Alloy 718, *J. Metals*, **21**: 46-54 (November 1969).
30. E. G. Richards and P. L. Twigg, Influence of Boron on the Creep-Resistance Properties of an Austenitic Nickel–Chromium Alloy Hardened by Structural Precipitation (in French), paper presented at the Eleventh Symposium on Metallurgy (Creep), Saclay, France, June 22–23, 1967, Metallurgy Colloquia Special Procedure Publications, pp. 97-102, French University Presses, Paris, 1968.
31. L. Hellner, Alloy Steels for Pressure Vessels, *Nucl. Eng.*, **13**(144): 426-428 (May 1968).
32. E. E. Krempl, The 550°F Notched High Strain Behavior of Three Low-Strength Structural Steels, USAEC Report GEAP-10090, General Electric Company, Atomic Power Equipment Department, August 1969.
33. H. Yamanouchi and Y. Asada, Effect of Mean Stress on Low-Cycle Fatigue Deformation Behavior (in Japanese), *Mitsubishi Juko Giho*, **6**: 439-446 (July 1969).

Section II

Reactor Materials

Metallurgy of Refractory Metals

By J. H. Peterson

NIOBIUM ALLOYS

Oxidation-Resistant Niobium Alloys

Westinghouse Astronuclear has concluded a program[1] aimed at the development of a fabricable, moderately oxidation-resistant niobium alloy for potential application as a protective cladding to back up the primary protective coating on high-strength niobium-alloy turbine blades. One feature of this program was the development of a model to predict the maximum surface recession allowable in a cladding alloy while still providing adequate protection to the core alloy for target times up to 50 hr at temperatures to 2200°F (1200°C). On the basis of this model, the maximum oxidation-rate constants for the cladding-alloy candidate at 2000 and 2200°F were set at values of 5.6 and 4.0 mils/(hr)$^{1/2}$, respectively.

Of numerous alloys investigated, the best oxidation resistance was demonstrated by a Nb–15 Ti–10 Ta–10 W–2 Hf–3 Al alloy, designated as B-1, which showed surface recession-rate constants of roughly 2.5 and 1.5 mils/(hr)$^{1/2}$ at 2200 and 2000°F, respectively. The surface oxide formed on exposing the B-1 alloy in flowing air at temperatures through 2400°F (1315°C) was quite adherent, although some spalling occurred on cooling below 1500°F (815°C). Further improvement in the alloy's oxidation resistance at 2000 and 2200°F was afforded through the use of a 1-hr, 2400°F oxidation exposure either prior to or during a 40-hr exposure period at the lower temperatures. A brief comparative evaluation indicated that the weight-gain behavior of the B-1 alloy at 2200°F for times to 64 hr was approximately equivalent to that shown by several experimental variations of Wah Chang's new oxidation-resistant WC-3015 alloy.

The Wah Chang 3015 alloy is also a niobium-base alloy designed for structural application in a high-temperature, oxidizing environment.[2] Composition of the alloy can be tailored, within the recommended ranges below, to meet varying requirements.

Element	Range, wt.%
Hf	28–30
Zr	1–2
W	13–16
Ta	0–4
Ti	0–5
C	0.07–0.33

In an oxidizing atmosphere, the unusually high hafnium content of this alloy favors the promotion of a tight, oxidation-resistant scale (based on 6HfO–Nb_2O_5). Optimum oxidation resistance (e.g., oxide penetration to a depth of about 0.030 in. in 24 hr in static air at 2400°F) is achieved by adding 5 wt.% titanium, at the expense of some reduction in hot strength above 1500°F. Optimum hot strength is achieved by eliminating the titanium and maintaining the tungsten, zirconium, and carbon additions near the upper limits shown above. Some preliminary tensile and stress-rupture properties for several compositional variations of the alloy are given in Table II-1.

Carbide Precipitation in D-43 Alloy

The precipitation behavior of niobium alloy D-43 (Nb–10 W–1 Zr–0.1 C) has been investigated at the Air Force Materials Laboratory.[3a] The formation of the precipitate phases in this alloy was studied by metallography and X-ray diffraction analysis of chemically extracted phases. Complete solution of carbide phases occurred at and above 1650°C. The time and temperature dependence of precipitation of the equilibrium carbide phase, a zirconium-rich monocarbide (Zr,Nb)C, was shown to be influenced by the cooling rate after solution annealing. This effect is apparently caused by nonequilibrium niobium carbides that precipitate during cooling from high annealing temperatures. The reduced room-temperature ductility of alloy D-43 in the solution-annealed condition was attributed

Table II-1 Mechanical Properties of Several WC-3015 Alloy Variations,[2] Tested as Bar or Rod Annealed 6 Hr at 2400°F

Test temp., °F	Tensile properties: Ultimate strength, ksi	Yield strength, ksi	Elongation, %
	Nb–30 Hf–13.5 W–5 Ti–1 Zr–0.1 C		
RT	133	129	28
1400	112	83.1	8
	Nb–29 Hf–14.5 W–1 Zr–0.1 C		
RT	129	122	33
1400	113	77.3	10
	Nb–29 Hf–13.5 W–1 Zr–0.3 C		
RT	142	128.3	4
1400	114	80.9	14

Stress-Rupture Properties at 2200°F and 20 ksi Stress

Life, hr	Reduction of area, %	Elongation, %
	Nb–30 Hf–13.5 W–5 Ti–1 Zr–0.1 C*	
18.9	62.6	57.4
	Nb–29 Hf–14.5 W–1 Zr–0.1 C	
31.0	39.8	43.1
	Nb–29 Hf–13.5 W–1 Zr–0.3 C	
30.0	73.5	29.6

*Annealed 1 hr at 3200°F plus 1 hr at 2400°F.

to the precipitation of what appeared to be Nb_2C at grain boundaries. The improvement of room-temperature ductility during aging seems to be related to the dissolution of the carbide phase at grain boundaries. Precipitation of metastable niobium carbides prior to the formation of (Zr,Nb)C depletes the matrix of carbon supersaturation and therefore reduces the driving force for (Zr,Nb)C precipitation. The nucleation of the (Zr,Nb)C particles seems to be strongly dependent on the availability of carbon, and the result is a nonuniform distribution of stable (Zr,Nb)C precipitates. Evidence of increasing carbide solutioning was found after heating at temperatures above 1200°C; hence coagulation of equilibrium carbides can be expected in this temperature range.

CREEP OF REFRACTORY ALLOYS

The high-temperature creep data for six refractory-metal alloys that are potential structural materials for space power systems have been analyzed by NASA–Lewis.[4] The materials are the tantalum alloys T-111 (Ta–8 W–2 Hf) and T-222 (Ta–10 W–2.5 Hf–0.01 C), the molybdenum alloys TZM (Mo–0.5 Ti–0.08 Zr–0.03 C) and TZC (Mo–1.2 Ti–0.25 Zr–0.15 C), and the niobium alloys D-43 (Nb–10 W–1 Zr–0.1 C) and Nb–1 Zr. The method of least squares was used to analyze statistically experimental creep data reported by other investigators. The form of the creep-rate equation is based on the generally accepted theory that creep is a function of time, temperature, stress, and structure. Stress is expressed as a power function and temperature as an exponential function. The empirical constants determined for the stress and temperature terms agreed with those reported by other investigators for similar refractory materials undergoing high-temperature creep. The correlating equations cover a temperature range of 1256 to 1922°K (1800 to 3000°F) and a stress range of 3.4×10^6 to 5.5×10^8 N/m² (500 to 80,000 psi). The variability associated with each equation is expressed in terms of its standard deviation. Since the standard deviation is quite different for each material, it is important that this factor be considered when applying the equations. The creep-rate equations resulting from the least-squares analysis are as follows:

$$\text{T-111: } \dot{\epsilon} = 3.776 \times 10^{-20}\, \sigma^{3.692} \times \exp(-397{,}075/RT)$$

$$\text{T-222: } \dot{\epsilon} = 1.094 \times 10^{-28}\, \sigma^{4.995} \times \exp(-458{,}902/RT)$$

$$\text{TZM: } \dot{\epsilon} = 7.083 \times 10^{-20}\, \sigma^{3.333} \times \exp(-321{,}475/RT)$$

$$\text{TZC: } \dot{\epsilon} = 1.036 \times 10^{-55}\, \sigma^{7.880} \times \exp(-402{,}628/RT)$$

$$\text{D-43: } \dot{\epsilon} = 3.863 \times 10^{-35}\, \sigma^{5.549} \times \exp(-353{,}944/RT)$$

$$\text{Nb–1 Zr: } \dot{\epsilon} = 4.333 \times 10^{-35}\, \sigma^{5.988} \times \exp(-370{,}856/RT)$$

where $\dot{\epsilon}$ = creep rate, hr^{-1}
σ = stress, N/m^2
R = gas constant = 8.3143 joules/(gram mole) (°K)
T = absolute temperature, °K

The uncertainty in the creep rates predicted by these equations is quite different for each alloy and must be considered when using the correlations. The range of uncertainty expressed as the ratio of maximum to minimum creep rates for ±1 standard deviation, from the correlating equation, is 2.9 for D-43, 4.4 for Nb–1 Zr, 6.7 for T-111, 20.8 for T-222, 30.4 for TZC, and 163.7 for TZM. The greater this ratio, the less reliable is the correlation. For comparison, the ratio for a standard commercial stainless steel is 2. The large variation reflects the inherent nonuniformity of the refractory metals at this stage of their commercial development. The reasons for this nonuniformity would include small differences in chemical composition, the type of heat-treatment, and the amount of work the test specimen receives. A comparison of the creep properties of the six alloys indicated that TZC is significantly superior in creep resistance, followed by T-222, T-111, and TZM which have similar creep properties, D-43 which is less creep resistant, and Nb–1 Zr which has very poor creep resistance.

The NASA work indicates that the variability in the creep rate of the molybdenum-base alloys is most affected by differences in chemical composition, heat-treatment, and the amount of work received by the test specimen. At Oak Ridge,[5] Stephenson has studied the effect of fabrication variables on the creep-rupture properties of TZM (Mo–0.5 Ti–0.08 Zr–0.03 C), Nb–TZM (Mo–1.5 Nb–0.5 Ti–0.08 Zr–0.05 C), and TZC (Mo–1.2 Ti–0.25 Zr–0.15 C) at 982, 1093, 1204, and 1315°C for rupture times up to 1000 hr. The creep tests were performed in vacuum creep furnaces operating at pressures $\leqslant 2 \times 10^{-7}$ torr. After-test chemical analyses showed no significant changes in interstitial content. The creep-rupture properties of TZM, fabricated according to current mill practice, were determined in the stress-relieved and in the recrystallized conditions to provide control data. Specimens of TZM, Nb–TZM, and TZC fabricated according to each of two experimental fabrication schedules were then tested. The schedules differed in terms of in-process annealing temperatures and warm-working temperatures. The data presented in this study indicate that fabrication variables have a profound effect on the longtime creep-rupture properties of these alloys. Because of the comprehensive nature of this investigation, it is recommended that the reference be consulted to determine the specific effects of the different fabrication schedules on the creep-rupture properties.

MOLYBDENUM ALLOYS

Battelle–Columbus investigators[3b] studied the deformation and fracture characteristics of TZM (Mo–0.5 Ti–0.1 Zr–0.001 to 0.019 C) over the temperature range 200 to 1850°C, with emphasis on evaluating the influence of strain rate, structural condition, and carbon content on the mechanical behavior. Three alloys, containing 10, 100, and 190 ppM carbon were evaluated in both the wrought-stress-relieved and recrystallized conditions at tensile strain rates of 0.01, 2, and 600 min^{-1}. The yield and ultimate strengths of the wrought-stress-relieved alloys decreased continuously with increasing temperature. However, for recrystallized alloys, it was found that dynamic strengthening occurred in the temperature range around 1000 to 1650°C. This resulted in strength peaks, which were much more pronounced in the two higher carbon alloys than in the alloy containing 10 ppM carbon. This effect is attributed to dynamic precipitation of carbides during deformation. Associated with the strength peaks was a marked ductility decrease caused by severe grain-boundary cracking. This effect is rationalized in terms of the relative shear strengths of the matrix and the grain boundaries. In the range of approximately 1000 to 1650°C, grain-boundary sliding leads to intergranular cracking, and the cracks propagate rapidly to failure. At higher temperatures the cracks still form, but dynamic recrystallization assists in blunting them, allowing relatively large deformations before failure.

TUNGSTEN ALLOYS

Structure of Arc-Cast Tungsten

The grain size of vacuum-arc-cast tungsten can be reduced significantly by the addition of small amounts of molybdenum. Barr and Klaphaak[6] have shown that the optimum addition is about 4 wt.% molybdenum to ingots with low residual-carbon contents and slightly below 4 wt.% for ingots containing 100 to 150 ppM carbon. The as-cast grain orientation of vacuum-arc-cast tungsten ingots was found to be sensitive to the rate of melting. High melting rates tended to produce an essentially radial columnar growth, whereas low melting rates tended to produce columnar growth predominantly parallel to the ingot axis. Low-carbon unalloyed tungsten was not successfully extruded at

temperatures in the range of 2200 to 2600°F (1200 to 1425°C). Low-carbon tungsten with a grain-refining addition of 3.72 wt.% molybdenum was, however, successfully extruded at 2400 and 2600°F (1315 and 1425°C).

Nitrogen in Tungsten

The mechanisms controlling the internal nitriding of tungsten-base alloys containing hafnium have been studied[7] by the Air Force Materials Laboratory. It was shown that W, W–Re, and W–Re–Mo alloys containing as much as 3 at.% hafnium in solid solution are subject to internal nitriding when exposed to nitrogen gas at temperatures above about 1500°C. The hafnium nitride particles that are formed as a result of nitriding precipitate as plates on (001) matrix planes, and this platelike habit is retained up to at least 2000°C. At 1 atm nitrogen pressure and temperatures between 1500 and 2000°C, the kinetics of internal nitriding were found to be controlled exclusively by the diffusion of nitrogen in the base metal or alloy matrix. The simple theoretical model developed by Wagner for the diffusion-controlled kinetics of internal oxidation provides an adequate description of the internal nitriding behavior. Permeation constants for nitrogen in tungsten derived from the measured internal-nitriding rates are found to be in good agreement with values obtained from direct steady-state permeation measurements. From published solubility data, the diffusion coefficient for nitrogen in tungsten, $D = D_0 \exp(-Q_D/RT)$, was evaluated from the relation $P = ND$, where P is the permeation constant and N is the solubility at 1 atm pressure. The results yield $D_0 \approx 1.2 \times 10^{-2}$ cm^2/sec and $Q_D \approx 32.2$ kcal/mole.

VANADIUM-BASE CLADDING ALLOYS

A comparison between austenitic stainless steel and vanadium and vanadium-base alloys for reactor applications has been made by Argonne.[8] On the basis of thermal expansivities, thermal conductivities, densities, and mechanical properties, computer-fitted polynomial expressions are presented that define the linear thermal-expansion behavior of vanadium, titanium, chromium, certain V–Ti and V–Ti–Cr alloys, and 304 and 316 stainless steels between 0 and 1000°C. The mean expansion coefficients for the vanadium-base alloys differ only slightly from those for unalloyed vanadium (plus or minus 6%) and are 65 to 80% lower than the mean expansion coefficients for the austenitic stainless steels. Densities of the vanadium-base alloys and the austenitic stainless steels were determined at 25°C by liquid displacement. The V–Ti alloys show a nonlinear decrease in density with increasing titanium for titanium contents greater than 30 wt.%. The V–Ti–Cr alloys exhibit a nonlinear change in density for compositions containing greater than 15 wt.% titanium and greater than 5 wt.% chromium.

A comparison of the mechanical and thermal properties of two vanadium-base alloys and two austenitic stainless steels was made to determine their relative usefulness as reactor fuel jackets for service between 500 and 700°C. This comparison shows that vanadium-alloy fuel jackets would be subjected to only one-third the thermal stresses generated in austenitic-stainless-steel jackets during reactor excursions between 500 and 700°C under conditions where the fuel is not in intimate contact with the jacket. This difference in thermal stresses in the two jacket materials is the result of the 37% higher tensile strength, 40% higher thermal conductivity, and 70% lower thermal expansivity exhibited by the vanadium alloys as compared with the austenitic stainless steels.

REFERENCES

1. J. A. Comie and R. C. Goodspeed, Development of Ductile Oxidation Resistant Columbium Alloy, Report AFML-TR-69-64, Westinghouse Astronuclear Laboratory, July 1969.
2. Wah Chang Corp., Albany, Oregon, Trade Brochure No. WC-3015.
3. F. Benesovsky (Ed.), Proceedings of the 6th International Seminar on High Temperature Materials, Fundamentals and Developments, Reutte/Tirol, Austria, June 24–28, 1968, Metallwerk Plansee AG, 1969.
   a. F. Ostermann and F. Bollenrath, On the Precipitation Behavior of Niobium Alloy D-43(Nb–10 W–1 Zr–0.1 C), pp. 317-340.
   b. B. A. Wilcox, A. Gilbert, and B. C. Allen, Elevated Temperature Deformation and Fracture of a Precipitation Hardened Molybdenum Alloy, pp. 208-227.
4. W. L. Maag and W. F. Mattson, Statistical Analysis of High-Temperature Creep-Rate Data for Alloys of Tantalum, Molybdenum, and Columbium, Report NASA-TN-D-5424, National Aeronautics and Space Administration, Lewis Research Center, September 1969.
5. R. L. Stephenson, The Effect of Fabrication Variables on the Creep-Rupture Properties of Molybdenum-Base Alloys, *Trans. Met. Soc. AIME*, 245: 997-1001 (May 1969).
6. R. O. Barr and D. J. Klaphaak, Effect of Molybdenum on the Grain Size and Workability of Arc-Cast Tungsten, *Met. Soc. Conf.*, 41: 727-735 (1967).
7. D. J. Iden, Internal Nitriding of Tungsten-Base Alloys, *Acta Met.*, 17: 1483-1499 (December 1969).
8. F. L. Yaggee, E. R. Gilbert, and J. W. Styles, Thermal Expansivities, Thermal Conductivities, and Densities of Vanadium, Titanium, Chromium, and Some Vanadium-Base Alloys (A Comparison with Austenitic Stainless Steel), *J. Less-Common Metals*, 19: 39-51 (September 1969).

Section

III

Reactor Materials

Diffusion Studies

By A. N. Ashurst

DIFFUSION IN NUCLEAR FUELS

Ceramic Fuels

The effects of density and grain size in starting samples of UO_2 and the evaporation of actinide elements on the diffusion of these elements in UO_2 were investigated[1] using ^{237}U and ^{233}Pa as tracers. Lattice diffusion and evaporation reportedly cause anomalous concentrations of diffusants near the surface and nonlinear concentration profiles. Away from the surface, the profiles were linear and characteristic of grain-boundary diffusion. The near-surface concentrations increased with higher densities and larger grain sizes in the starting material, except when evaporation of the diffusants overrode these effects.

The diffusion of ^{233}U in UO_2 single crystals prepared by floating-zone techniques was studied[2] by alpha-energy degradation from 1620 to 2010°C. The tracer was vacuum deposited onto polished surfaces of UO_2 and diffusion annealed under hydrogen. The authors summarized their data in the Arrhenius equation

$$D = 6.8 \times 10^{-5} \exp(-98{,}300/RT) \quad \text{cm}^2/\text{sec}$$

The diffusion coefficients are 10 to 1000 times smaller than previously reported, independently determined values, although the activation energies for diffusion agree reasonably well. Attempts were made to determine the influence of crystal size. The discrepancy was concluded to be due to the influence of grain-boundary diffusion, which apparently was neglected or underestimated in the prior work.

Diffusion of thorium in MgO was studied[3] using a ^{228}Th tracer that was diffused into crystals of MgO for 20 hr at 1585°C. A linear concentration profile was produced at depths between 0.4 μ and 3 μ in one specimen, yielding a diffusion coefficient of 4.6×10^{-14} cm^2/sec. This is four orders of magnitude smaller than the published value. Another specimen treated identically produced a curved concentration profile. These data are preliminary, but the author suggests that the thin-film analysis used may not apply because of suspected extremely low solubility of thorium in MgO.

Carbon self-diffusion in nearly stoichiometric UC was determined[4] in the range 1338 to 1772°K using ^{14}C-tagged UC tracer deposited onto polished surfaces by electron-beam vapor deposition. Residual surface activity after each diffusion anneal was measured by beta scintillator. The data gave calculated values of 0.1 cm^2/sec for the frequency factor and 62,500 ± 2000 cal/mole for the activation energy for diffusion.

Metallic Fuels

Diffusion couples of U–5 Fs alloy with 304L and 316 stainless steels were annealed for up to 10,000 hr at 550 to 650°C. The width of the diffusion zone was determined metallographically. Penetration-time log-scale profiles were linear and agreed well with data reported in the literature. The dependence of penetration coefficients on temperature is shown in Fig. III-1. The authors found that diffusion penetration into the fuel alloy was greater than that into the steels. High silicon and aluminum contents generally had no effect on compatibility between the fuel alloy and 304L stainless steel up to 650°C.

Two compositions of delta-stabilized Pu–Zr alloys containing 4.2 and 11.4 wt.% zirconium were[6] diffusion annealed between 351 and 475°C for between 12 and 203 days. X-ray-intensity profiles were obtained with an electron microanalyzer monitoring zirconium L_α radiation. Interdiffusion coefficients calculated by the Grube method followed the Arrhenius-type equation

$$D = 5.89 \times 10^{-6} \exp(-20{,}000/RT) \quad \text{cm}^2/\text{sec}$$

DIFFUSION IN REFRACTORY METALS

The effect of crystallographic orientation on the surface self-diffusion of molybdenum was studied[7] between 1600 and 2400°C. Surface diffusion coeffi-

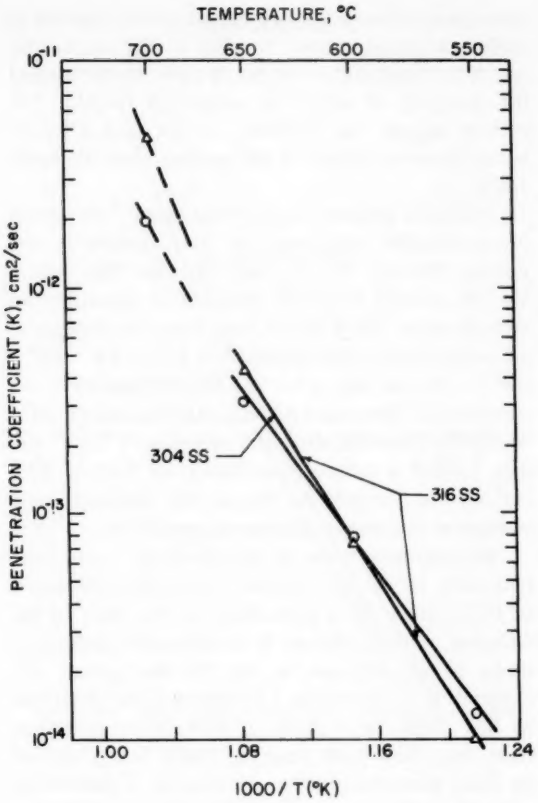

Fig. III-1 Diffusion penetration of stainless steels into U–5 Fs alloy.[5]

cients were calculated using Gjostein's iterative procedure to correct for small volume-diffusion contributions at the higher annealing temperatures. Results for bicrystals were compared with those for molybdenum sheet in the Arrhenius plots of Fig. III-2. The author notes that surface diffusion coefficients were independent of direction in the (001) plane, as expected, and that diffusion was slower on (011) planes. Differences in the activation energies indicated an anomalous variation with orientation. Diffusion of molybdenum in sheet form with a mild (001) preferred orientation or of bicrystals whose orientations range over the stereographic triangle was represented by the equation

$$D_s = 0.39 \exp(-51{,}500/RT) \quad \text{cm}^2/\text{sec}$$

The author points out that the constants in this equation suggest that surface diffusion occurred by vacancy or adatom migration.

In a Soviet study[8] of interdiffusion between tantalum and tungsten, group couples were diffusion annealed at 2000°C for 48 hr. The diffusion coefficients were composition dependent, and those for tantalum in tungsten decreased sharply with increasing tungsten content from 10 to 50 wt.% but increased gradually with increased tungsten content from 60 to 90 wt.%.

Lattice diffusion coefficients for niobium, tantalum, and tungsten isotopes in tungsten were measured[9] at 1300 to 2400°C using standard tracer methods in combination with anodic-film sectioning techniques. The data were summarized in the following Arrhenius-type equations:

$$D(\text{Nb}) = 3.01 \exp(-137{,}600/RT) \quad \text{cm}^2/\text{sec}$$

$$D(\text{Ta}) = 3.05 \exp(-139{,}900/RT) \quad \text{cm}^2/\text{sec}$$

$$D(\text{W}) = 1.88 \exp(-140{,}300/RT) \quad \text{cm}^2/\text{sec}$$

The authors emphasized the need for sensitivity and completeness in the data used for the determination of both lattice and short-circuit diffusion parameters. When lattice diffusion coefficients were being measured, even in single crystals, it was found that the section thickness had to be kept smaller than $\sqrt{(DT)}$ to minimize the effects of short-circuit paths. A unique diffusion coefficient could not be developed from the data generated in the region of the profile governed by short-circuit effects.

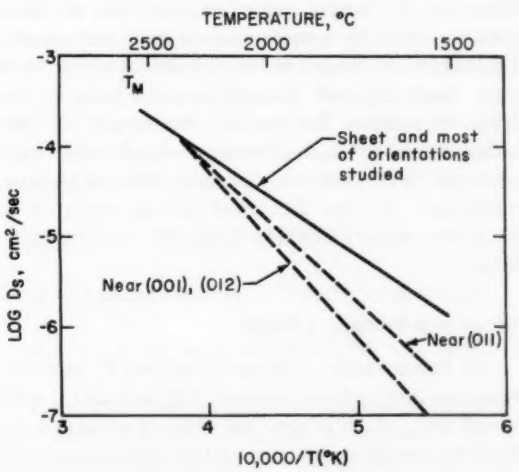

Fig. III-2 Effect of crystallographic orientation on the surface self-diffusion of molybdenum.[7]

DIFFUSION IN STRUCTURAL METALS AND MISCELLANEOUS METALLIC SYSTEMS

Diffusion in Zirconium

A Soviet study[10] indicated that the diffusion of beryllium in zirconium and titanium is characterized by the unusually high diffusion constants of 2 to 5 x 10^{-5} cm^2/sec at the melting point of the base.

The results of a Canadian study of self-diffusion and solute diffusion in zirconium were summarized[11] in two parts. The diffusion coefficient of ^{60}Co in the body-centered cubic (bcc) beta phase of 99.99% pure polycrystalline zirconium was measured at 920 to 1700°C. The Arrhenius plot of log D vs. $1/T$ shows some evidence of positive curvature above 1600°C, but below that it is strictly linear and can be represented by:

$$D = (3.26 \pm 2.77) \times 10^{-3} \times \exp(-21{,}820 \pm 900/RT) \quad cm^2/sec$$

Anomalies in the concentration profiles were noted in experiments at temperatures below 1200°C.

The effects of cobalt additions on the diffusion rates of ^{95}Zr and ^{60}Co in bcc zirconium were measured[12] for cobalt concentrations between 0.0 and 2.0 at.% at an annealing temperature of 993°C. The diffusion coefficient of zirconium is markedly increased by adding between 0.4 and 2.0 at.% cobalt, whereas that of ^{60}Co is slightly decreased. An analysis of the results in terms of the deduced correlation factor for the cobalt solute indicates that diffusion does not occur by a single vacancy mechanism alone. The results are described by a model in which both single vacancies and dislocations contribute to the diffusion process. The vacancy component for the zirconium self-diffusion, however, is much larger than predicted from empirical relations. The dislocation component can be accounted for in terms of a dislocation density between 2 x 10^5 and 2 x 10^8 lines/cm^2.

Diffusion in Refractory Metals

An Italian study of diffusion between commercial aluminum and niobium between 500 and 630°C was carried out[13] to determine the limit of utilization of these two metals in intimate contact. Surface layers of niobium were produced either by vapor deposition under vacuum or by reduction of $NbCl_5$. Examination of the samples after heat-treatment showed that interaction between the two metals can be regarded as unlikely at temperatures below 500°C. The microprobe and X-ray analyses of the penetration bands revealed the presence of only one compound, $NbAl_3$. The authors suggest that niobium can act as a diffusion barrier between aluminum and various materials up to 500°C.

Diffusion processes were investigated[14] by means of quantitative electron-probe microanalysis in the systems Mo–Al, Nb–Al, and Mo–Nb. The system Mo–Nb showed a smooth variation of concentration with distance. The diffusion coefficient was dependent on concentration and amounted to 0.7 to 3.0 x 10^{-14} cm^2/sec. In the case of Mo–Al, the diffusion zone was composed of the phases Al_8Mo_3, Al_4Mo, and $Al_{12}Mo$. Within the phase Al_8Mo_3 after annealing at 525°C, the data yielded a diffusion coefficient of 8.47 x 10^{-6} cm^2/sec. In the Nb–Al system, the diffusion zone consists of the intermetallic compound $NbAl_3$.

Molybdenum is one of the fission products most frequently found as a metallic inclusion in irradiated $(U,Pu)O_2$ fuels. As a preliminary to the study of the diffusion of molybdenum in stainless-steel cladding, a study of its diffusion in the Fe–Mo system was undertaken.[15] The method employed is that described by Jost (*Diffusion in Solids, Liquids, Gases,* Academic Press, Inc., New York, page 72, 1960). It was verified by X-ray microanalysis that the kinetics of dissolution of the precipitates are not influenced by the diffusion. Formulas are given for relating the coefficient of diffusion, the solubility of molybdenum in iron, the concentration of the two-phase alloy used, and the displacement of the interface zone with respect to the two phase–one phase system. As the temperature is increased, the solubility increases rapidly and variations in the coefficient of chemical diffusion with concentration become significant.

A study of the isotope effect for diffusion in vanadium between 960 and 1817°C was conducted[16] using ^{55}Fe and ^{59}Fe tracers. Specimens annealed above 1200°C were lathe sectioned, and those annealed at the lower temperatures were chemically sectioned. Log-scale penetration profiles were linear, and plots of log D vs. $1/T$ yielded straight lines having a change in slope near 1350°C, as shown in Fig. III-3. The authors determined the relative rates of diffusion in vanadium for the two isotopic species and then showed the change in the isotope effect with temperature. The greatest rate of change in the isotope effect occurred at about 1400°C. The authors interpret the results as indicating that two mechanisms of diffusion operated in the vanadium: mainly single-vacancy motion at low

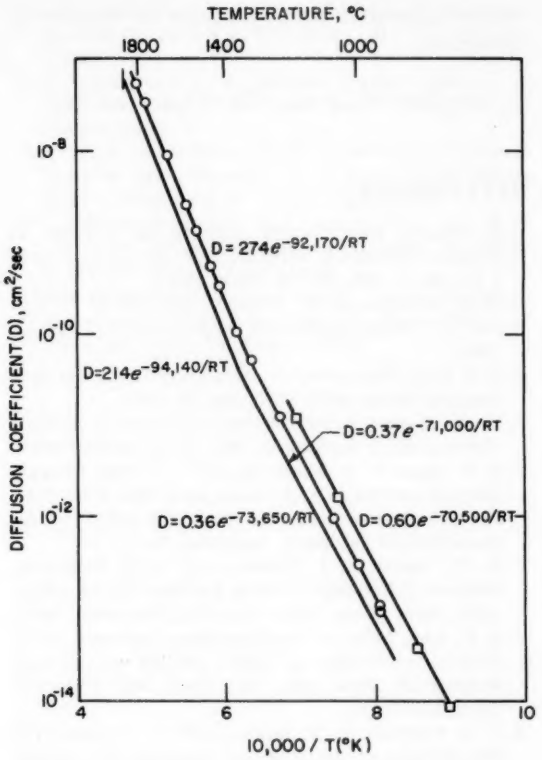

Fig. III-3 Diffusion of ^{59}Fe in vanadium.[16] ○, ^{59}Fe in vanadium (Coleman et al.); □, ^{59}Fe in vanadium (Peart); —, ^{48}V in vanadium (Peart).

temperatures and mainly divacancy motion at high temperatures.

Diffusion in Superalloys

The diffusion of titanium in Hastelloy N was studied[17] to predict the maximum loss by diffusion of titanium from the alloy in a typical molten-salt breeder reactor at 700°C. The diffusion of ^{44}Ti was examined at temperatures of 800 to 1250°C by lathe or grind sectioning and measuring the loss in activity by gamma spectroscopy. The data were described by the Arrhenius-type equation:

$$D = 15.3 \exp(-73{,}000/RT) \quad \text{cm}^2/\text{sec}$$

A complete determination of interdiffusion coefficients in the ternary system Fe–Co–Ni was made[18] at 1315°C. The data are presented in contour maps showing the variation of cross and direct interdiffusion coefficients with composition. The authors show that the diffusion process can be described with just two interdiffusion coefficients, a direct one and a cross-diffusion coefficient.

DIFFUSION OF INTERSTITIALS AND GASES IN METALS

Volume and grain-boundary diffusion were studied in Ta–C couples at 1600 to 1900°C and in Zr–C couples at 1100 to 1700°C.[19] Volume-diffusion coefficients determined from electron-microprobe data were described by the equations:

$$D_{\text{vol.(C-Ta)}} = 8.54 \times 10^{-4} \times \exp(-52{,}500/RT) \quad \text{cm}^2/\text{sec}$$

$$D_{\text{vol.(C-Zr)}} = 1.4 \times 10^{-6} \times \exp(-30{,}000/RT) \quad \text{cm}^2/\text{sec}$$

Grain-boundary effects were graphically separated from volume-diffusion effects for the Zr–C system, and grain-boundary diffusion coefficients were determined by applying Fisher's equations. Diffusion was described by the following equation:

$$D_{\text{g.b.(C-Zr)}} = 2.35 \times 10^{-1} \times \exp(-24{,}100/RT) \quad \text{cm}^2/\text{sec}$$

The diffusion of carbon in hafnium was investigated[20] at 1120 to 2130°F (605 to 1165°C). Log-scale concentration profiles were linear. Diffusion coefficients were calculated from the formula $D = 0.1086/r \tan a$, where r is time and $\tan a$ is the slope of line of ln I vs. x^2; I is intensity of isotope activity and x is distance (in centimeters). In the alpha phase, diffusion was described by the equation:

$$D_\alpha = 74 \times 10 \exp(-74{,}600/RT) \quad \text{cm}^2/\text{sec}$$

In the beta phase, diffusion followed the expression:

$$D_\beta = 4.2 \times 10^{-2} \exp(-40{,}000/RT) \quad \text{cm}^2/\text{sec}$$

The permeability of hydrogen through alpha palladium from 300 to 709°K was determined[21] by a low-pressure technique that was not surface limited but rather diffusion controlled, as indicated by the data which showed a square-root dependence on pressure and reciprocal dependence on thickness. Palladium was

heated in oxygen at 400°C to ensure a diffusion-controlled process with a subsequent reduction in hydrogen. Permeability was described by the equation:

$$J = 1.80 \times 10^{-3} P^{\frac{1}{2}} \times \exp(-3745/RT) \quad \text{cm}^3 \text{ (STP)/(sec)(cm)}$$

for pressures (P) of 2.9×10^{-5} to 5.0×10^{-3} cm Hg. Taking the solubility of Favreau et al.,[22]

$$c = 3.65 \times 10^{-1} P^{\frac{1}{2}} \exp(2000/RT)$$

the diffusion coefficient was calculated to be

$$D = 4.94 \times 10^{-3} \exp(-5745)/RT) \quad \text{cm}^2/\text{sec}$$

Diffusion coefficients of hydrogen in aluminum were determined[23] from hydrogen-gas extraction curves for pure aluminum over a temperature range of 570 to 630°C. The diffusivity of hydrogen in aluminum was described by the equation:

$$D = 2.0 \times 10^{-2} \exp(-12{,}000/RT) \quad \text{cm}^2/\text{sec}$$

Single-crystal nickel alloy and polycrystalline nickel and iron alloys containing small amounts of silicon were subjected to internal oxidation to determine[24] the diffusivity of oxygen in nickel and alpha iron between 800 and 1300°C. Penetration depths were determined microscopically. Allowances were made for the absorption of oxygen in the reaction with silicon. The following activation energies and pre-exponential factors were derived:

Alloy	Temp., °C	Activation energy, cal/gram atom	Preexponential factor, cm^2/sec
Ni–0.058 Si	800–1200	73,900	7.9×10^4
Ni–0.48 Si	900–1300	74,400	9.5×10^4
Fe	700–850	39,900	4.0×10^{-1}

The diffusivity of nitrogen in molybdenum was determined[25] by a quenching technique, coupled with liquid-helium resistivity measurements to monitor the presence of the gas. The high-purity, zone-refined molybdenum specimens were initially charged with 300 torrs nitrogen at 1850°C and quenched in mercury. Nitrogen evolution was then induced between 1500 and 2000°C. Semilog plots of diffusivity vs. inverse temperature yielded a straight line described by the equation:

$$D = 3.0 \times 10^{-3} \exp(-1.20 \text{ eV/kt}) \quad \text{cm}^2/\text{sec}$$

REFERENCES

1. H. Furuya, Some Factors Affecting the Diffusion of Actinide Elements in UO_2, *Sci. Rep. Res. Inst., Tohoku Univ., Ser. A.*, **20:** 167-175 (March 1969).
2. D. K. Reimann and T. S. Lundy, Diffusion of ^{233}U in UO_2, *J. Amer. Ceram. Soc.*, **52**(9): 511-512 (Sept. 21, 1969).
3. A. D. King, Progress Report: Diffusion of Thorium in MgO, Canadian Report AECL-3477, Sept. 30, 1969.
4. R. A. Krakowski, Self-Diffusion of Carbon in Uranium Monocarbide, *J. Nucl. Mater.*, **32:** 120-125 (August 1969).
5. S. T. Zegler, H. V. Rhude, Jr., and J. A. Lahti, Compatibility of Uranium–5 Wt.% Fission Alloy with Types 304L and 316 Stainless Steel, USAEC Report ANL-7596, Argonne National Laboratory, September 1969
6. M. R. Harvey, A. L. Rafalski, and D. H. Riefenberg, Chemical Diffusivities of Delta Stabilized Pu–Zr Alloys, *ASM, Trans. Quart.*, **62**(4): 1014-1015 (December 1969).
7. B. C. Allen, Effect of Crystallographic Orientation on the Surface Free Energy and Surface Self-Diffusion of Solid Molybdenum, *Trans. Met. Soc. AIME*, **245:** 2089-2096 (September 1969).
8. I. A. Tregubov, L. N. Kuzina, and O. S. Ivanov, The Interdiffusion of Tantalum and Tungsten, *Dokl. Chem. Technol. Proc. Acad. Sci. USSR*, **180-181:** 83-84 (May–August 1968), translated from *Dokl. Akad. Nauk SSSR*, **180**(2): 423-424 (May 1968).
9. R. E. Pawel and T. S. Lundy, Tracer Diffusion in Tungsten, *Acta Met.*, **17:** 979-988 (August 1969).
10. L. V. Pavlinov, G. V. Grigor'ev, and G. O. Gromyko, Diffusion of Beryllium in Zirconium and Titanium (in Russian), *Izv. Akad. Nauk SSSR, Metal.*, No. 3: 207-209 (May–June 1969).
11. G. V. Kidson and G. J. Young, Self and Solute Diffusion in Zirconium. I. The Diffusion of ^{60}Co in β Zr, *Phil. Mag.*, **20:** 1047-1056 (November 1969).
12. G. V. Kidson and J. S. Kirkaldy, Self and Solute Diffusion in Zirconium. II. The Effect of Cobalt Additions on the Diffusion of ^{95}Zr and ^{60}Co in β-Zirconium, *Phil. Mag.*, **20:** 1057-74 (November 1969).
13. F. Brossa, G. Musso, and E. W. Schleicher, Study of Diffusion Between Aluminum and Niobium (in Italian), Abstracted in *Euratom Inform.* (Düsseldorf), **7**(12): 778 (December 1969).
14. S. Steeb and R. Keppeler, Diffusion Investigations in the Systems Mo–Nb, Mo–Al, and Nb–Al by Means of a Microprobe (in German), *Z. Naturforsch., A*, **24:** 1601-1606 (October 1969).
15. J. P. Pivot, A. Van Graeynest, and D. Calais, Chemical Diffusion in the System Iron–Molybdenum (in French), *J. Nucl. Mater.*, **31:** 342-344 (July 1969).
16. M. G. Coleman, C. A. Wert, and R. F. Peart, Isotope Effect for Diffusion of Iron in Vanadium, *Phys. Rev.*, **175**(3): 788-795 (November 1968).

17. C. E. Sessions and T. S. Lundy, Diffusion of Titanium in Modified Hastelloy N, *J. Nucl. Mater.*, **31**: 316-322 (July 1969).
18. A. Vignes and J. P. Sabatier, Ternary Diffusion in Fe–Co–Ni Alloys, *ASM, Trans. Quart.*, **245**: 1795-1802 (August 1969).
19. H. Suzuki and S. Kimura, Study on Diffusion of Carbon in Tantalum and Zirconium by X.M.A., *Tokyo Kogyo Daigaku Gakuho*, No. 90: 105-115 (March 1969).
20. G. Ya. Meshcheryako, R. A. Andriyevskiy, and V. N. Zagryazbin, Diffusion of Carbon in Hafnium, *Fiz. Metal. Metalloved.*, **25**(1): 176-178 (1968).
21. S. A. Hoffler, J. B. Hudson, and G. S. Ansell, Hydrogen Permeation Through Alpha-Palladium, *Trans. Met. Soc. AIME*, **245**: 1735-1740 (August 1969).
22. R. L. Favreau, R. E. Patterson, D. Randall, and O. N. Salmon, The Solubility of Hydrogen and Tritium in Palladium Black, USAEC Report KAPL-1036, Knolls Atomic Power Laboratory, Apr. 15, 1954.
23. S. Matsuo and T. Hirata, Diffusion of Hydrogen in Aluminum, (in Japanese), *J. Jap. Inst. Metals*, **31**: 590-595 (1967); also, *Trans. Nat. Res. Inst. Metals (Tokyo)*, **11**(2): 22-26 (1969).
24. R. Barlow and P. J. Grundy, The Determination of the Diffusion Constants of Oxygen in Nickel and α-Iron by an Internal Oxidation Method, *J. Mater. Sci.*, **4**: 797-801 (1969).
25. J. H. Evans and B. L. Eyre, The Heat of Solution and Diffusivity of Nitrogen in Molybdenum, *Acta Met.*, **17**: 1109-1115 (August 1969).

Section
IV
Reactor Materials

Radiation Effects in Structural Materials

By M. Kangilaski

The proceedings of the fourth international symposium on the effects of radiation on structural materials have been published[1] by the American Society for Testing and Materials (ASTM) as Special Technical Publication No. 457. This meeting was held in San Francisco in June 1968. The book includes 22 papers on the effects of radiation on different materials.

STAINLESS STEELS AND NICKEL ALLOYS

The General Electric Company[2] has compiled and analyzed all data published up to November 1968 on the mechanical properties of irradiated 304 and 316 stainless steels and has suggested property limits for current use by designers. Data were available from tensile, creep, and burst tests on tubing. Revision of these limits in the light of new data is to be expected.

For use at total fluences above 10^{22} neutrons/cm^2, the following property limits are suggested:

- Yield stress at 0.2% offset:
  44,000 psi at 500°C
  31,000 psi at 600°C
  20,000 psi at 700°C
- Ultimate stress:
  58,000 psi at 500°C
  46,000 psi at 600°C
  30,000 psi at 700°C
- Uniform elongation: less than 1%
- Total elongation: less than 1%
- Minimum creep rate: unchanged to slightly increased by irradiation
- Time to rupture: reduced significantly by irradiation
- Creep strain to fracture: as low as 1%

Tensile tests have been performed[3] on specimens of solution-annealed 316 stainless steel irradiated in the Experimental Breeder Reactor II (EBR-II) to total fluences ranging from 2.8×10^{21} to 8.6×10^{21} neutrons/cm^2. Results of these tests are summarized in Table IV-1. At low testing temperatures radiation caused significant increases in yield strength, but elongation was not affected. At higher testing temperatures the yield-strength increases were smaller, but elongation was significantly reduced by the elevated-temperature embrittlement.

Creep-rupture properties of Incoloy 800 were determined by Oak Ridge[4] at 650°C. The specimens were irradiated to a fast fluence of 1.6×10^{21} neutrons/cm^2 at temperatures ranging from 350 to 650°C. Before irradiation the specimens had been annealed at 800, 1040, and 1150°C. Figure IV-1 shows that the preirradiation anneal at 1150°C results in the shortest 650°C rupture life and lowest ductility after irradiation at 550°C and above. Irradiation at lower temperatures produced displacement-type radiation damage, which is not so detrimental.

Void concentration in irradiated 304 stainless steel as a function of irradiation temperature and of fluence has been measured (Fig. IV-2).[5] The results indicate that the void density increases with increasing fast fluence and that at a given fluence more voids are produced in the 370 to 380°C range than in the 460 to 470°C range.

At a given irradiation temperature, the mean void diameter increases with increasing fluence, but the maximum void diameter appears to reach a limiting size after 10^{22} neutrons/cm^2. This limiting size is a function of irradiation temperature, being 220 Å at 370°C and 300 Å at 470°C. Postirradiation annealing at 600°C converted the dislocation loops to a dislocation network, and the smallest voids (diameters <150 Å) began to disappear.[6] As the annealing temperature was increased, the dislocation and void densities both decreased. After a 1-hr anneal at 900°C, the voids were completely removed, and the dislocation density was reduced to that of an unirradiated annealed specimen. The increase in void size and decrease in void density are illustrated in Fig. IV-3.

Table IV-1 Tensile Properties of 316 Stainless Steel Irradiated[3] in the EBR-II

Irradiation conditions	Property, psi or %	Test temperature, °C						
		315	426	482	538	593	648	760
Unirradiated controls as solution annealed (1063°C for 1 hr)	YS	19,800	21,000	19,300	18,300	17,100	17,200	16,000
	UTS	69,300	68,300	59,400	63,700	51,700	43,700	23,200
	E_U	44.9	48.7	56.1	48.0	30.0	22.7	16.1
	E_T	50.1	54.9	57.5	51.6	40.8	37.6	73.4
$8.6 \pm 1.3 \times 10^{21}$ neutrons/cm^2 (total) at 470°C	YS	32,000	31,300	29,100	33,800	33,600	30,900	23,900
	UTS	71,300	72,200	67,600	63,300	54,100	43,900	26,500
	E_U	24.7	22.7	28.9	18.1	11.0	4.6	2.4
	E_T	30.3	27.6	33.7	19.4	12.1	5.1	5.6
$6.0 \pm 1.2 \times 10^{21}$ neutrons/cm^2 (total) at 410°C	YS				41,800	34,400	27,500	16,100
	UTS				73,800	60,100	44,400	24,000
	E_U				21.8	24.8	11.1	12.2
	E_T				29.0	29.6	12.7	13.7
$2.8 \pm 0.8 \times 10^{21}$ neutrons/cm^2 (total) at 410°C	YS	22,000	23,500	17,600	19,300	20,600	18,900	14,000
	UTS	69,800	71,900	69,700	66,900	54,900	41,200	22,500
	E_U	43.4	46.4	41.3	38.4	26.8	13.6	5.7
	E_T	48.5	51.3	51.9	51.0	30.6	15.7	11.1
$2.8 \pm 0.8 \times 10^{21}$ neutrons/cm^2	YS	23,400	24,700	24,700	22,600	17,300	16,200	13,700
	UTS	73,000	72,200	72,000	69,000	54,400	39,400	22,600
	E_U	46.0	43.5	42.0	36.7	30.0	14.8	5.8
	E_T	50.6	50.4	52.0	47.9	32.7	18.1	11.7

German investigators have found[7] that irradiation at 100°C results in significant reductions in rupture life of Inconel 625 and Inconel 718 when tested at 650°C. However, the rupture life of 16/13 stainless steel, which contains 1.3 wt.% molybdenum and 0.87 wt.% niobium, was increased significantly by irradiation. These test results are illustrated in Figs. IV-4 and IV-5. Irradiation also decreased the minimum creep rate of the 16/13 stainless steel at 650°C by one to two orders of magnitude. This reduction is attributed to the presence of defects produced during the 100°C irradiation and not annealed out during testing at 650°C.

The effect of directional cold working on the embrittlement of 16/13 stainless steel irradiated at 50°C to 3×10^{20} neutrons/cm^2 and tensile tested between 500 and 800°C was also studied.[8] Below a 600°C test temperature, the transverse and longitudinal ductilities were about equal, whereas at 700 and 750°C the longitudinal ductility was significantly better. At 800°C, with recrystallization taking place, the anisotropy almost disappeared—especially in heavily worked specimens. These trends were exhibited by unirradiated controls as well as by the irradiated specimens, although the elongations of the latter were consistently lower.

The formation and stability of voids introduced in high-purity nickel by irradiation with neutrons in the temperature range 50 to 575°C have been studied.[9] Octahedral-shaped voids form during irradiation at temperatures ≥260°C ($0.30T_m$). The size of the voids increases and the density decreases with increasing irradiation temperature, but the volume fraction of voids is relatively independent of temperature. If nickel is irradiated at a low temperature (50°C) and subsequently annealed at an elevated temperature, stacking-fault tetrahedra are formed; voids do not develop. The voids present in the nickel irradiated at temperatures >260°C coarsen during isothermal annealing at 600°C by the process of large voids growing at the expense of smaller voids. At higher annealing temperatures, the voids anneal heterogeneously and are completely annealed at 800°C.

A study was made to determine whether high-temperature neutron irradiation modifies intragranular precipitation processes in a 16 Cr–12 Ni–1 Nb steel.[10] Both matrix and stacking-fault NbC particles precipi-

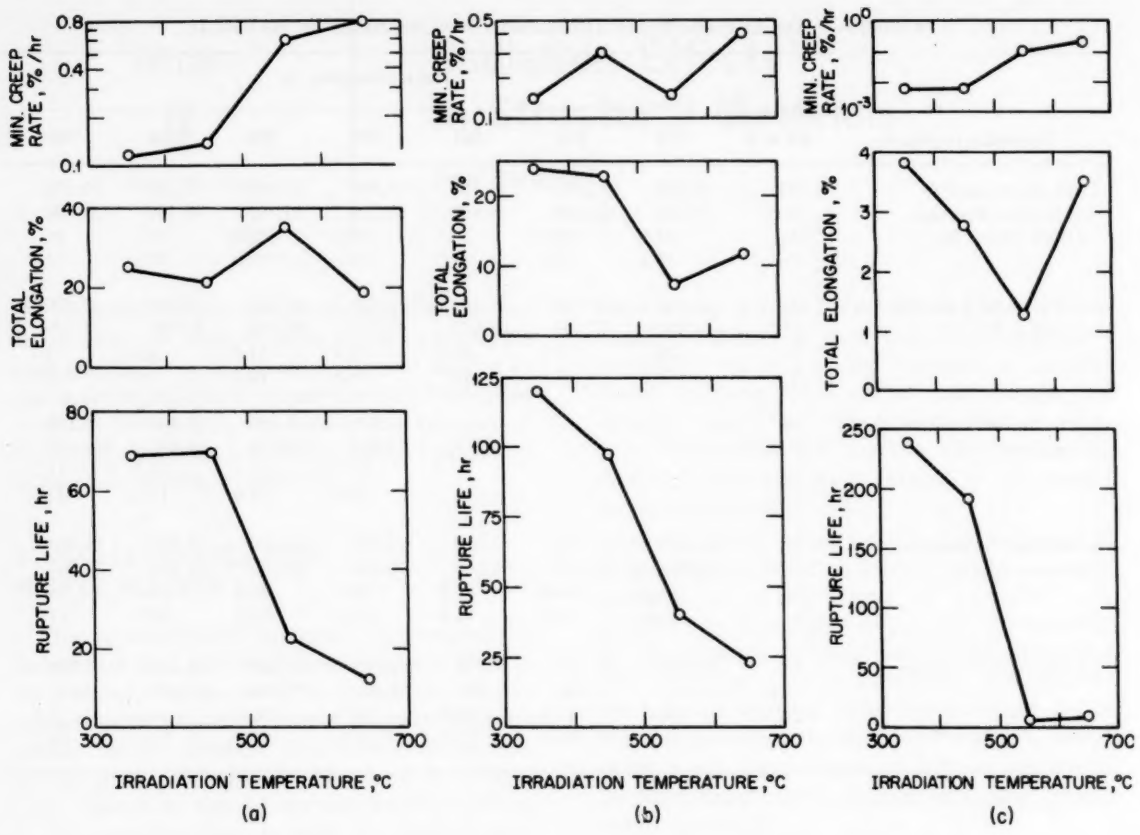

Fig. IV-1 Creep-rupture properties of Incoloy 800 containing 0.1 wt.% titanium and 0.12 wt.% carbon, tested in air at 650°C after irradiation at indicated temperature to 1.6×10^{21} neutrons/cm^2 (fast).[4] (*a*) 800°C preirradiation anneal. (*b*) 1040°C preirradiation anneal. (*c*) 1150°C preirradiation anneal.

tated during irradiation but not during thermal aging at the irradiation temperature. The amount and type of precipitate depended critically on the preirradiation heat-treatment. After a solution treatment and irradiation, the matrix-precipitate density generally increased near incoherent boundaries; but, when the steel was aged immediately after solution treatment and then irradiated, a precipitate-free zone formed at each of the boundaries as a result of solute denudation. Matrix precipitation was not observed in the unirradiated control specimens. It is apparent that irradiation-produced vacancies are important in facilitating the nucleation of matrix NbC precipitates, provided that the solute supersaturation is sufficiently high. Although the nucleation of stacking-fault NbC was enhanced by irradiation, its presence was confined to material with a solute concentration much higher than that required for matrix precipitation. The irradiated specimens were always stronger than the thermal controls, and precipitates were formed. The proportional limit at 650°C increased from a control value of 20 ksi to 50 ksi after irradiation. Helium bubbles were often attached to the NbC precipitates.

PRESSURE-VESSEL STEELS

Canadian investigators established that the ductile-to-brittle transition temperatures that are determined on a 3.5 wt.% nickel steel by breaking subsize Izod specimens are somewhat lower than those determined by breaking Charpy V-notch specimens.[11] For example, when both types of specimens were tested after irradiation at <120°C to 2.5×10^{19} neutrons/cm^2 (>1 MeV), the radiation-induced increase in transition

temperature of the Izod specimens was 190°C, as compared with 220°C from the Charpy tests. However, a larger difference was noted between the actual Charpy and Izod transition temperatures of both the unirradiated specimens (−50 vs. −104°C) and the irradiated specimens (170 vs. 86°C).

Figure IV-6 illustrates the relative effects of irradiation and aging at elevated temperatures on the impact properties of 12 Ni–5 Cr–3 Mo maraging steel.[12] It is seen that at a temperature of 550°F (290°C) radiation damage accounts for more than half the increase in transition temperature, the remainder being caused by thermal aging. However, at 740°F (395°C) the thermal treatment accounts for all of the embrittlement, since the increase in transition temperature is the same in irradiated specimens as in unirradiated specimens after 1900 hr.

Japanese investigators[13] have compared the response of A-302B and aluminum-killed steel base metal, weld metal, and the heat-affected zone to a fast fluence of 6×10^{18} neutrons/cm^2. It was found that the transition-temperature increases were 67°C in A-302B base metal, 107°C in its weld metal, and 95°C in its heat-affected zone. The change in impact properties due to neutron irradiation was larger in aluminum-killed steel than in A-302B steel.

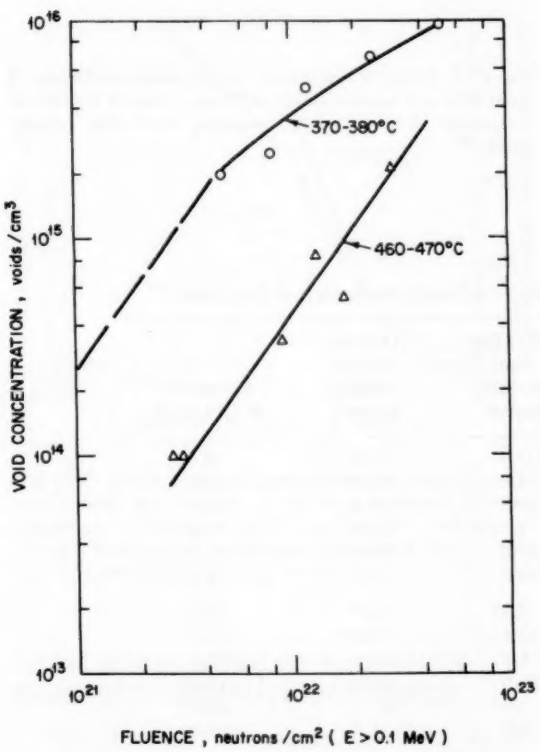

Fig. IV-2 Effect of irradiation temperature and fluence on void density in 304L stainless steel.[5]

MISCELLANEOUS ALLOYS

The results of room- and elevated-temperature tensile tests in vacuum ($<1.8 \times 10^{-5}$ torr) on tantalum and Ta–10 W specimens before and after irradiation at ~70°C are summarized in Tables IV-2 and IV-3. The specimens exhibited the usual displacement type of radiation damage at low testing temperatures but did not undergo elevated-temperature embrittlement as do stainless steels and nickel-base alloys.

The effect of postirradiation annealing on room-temperature hardness and void distribution of irradiated vanadium was studied at Oak Ridge.[4] Figure IV-7 illustrates that the microhardness is directly related to the void density observed by transmission electron microscopy.

The effects of irradiation on the hot hardness of alloys based on Mo, W, Nb, Ta, V, and Fe have been compiled into a single report by workers at General Electric.[15]

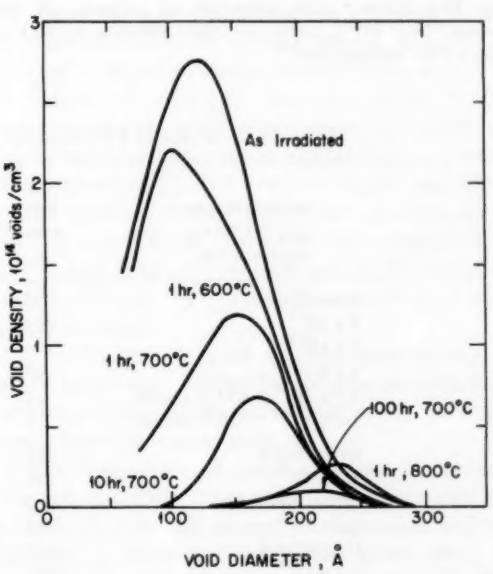

Fig. IV-3 Effect of postirradiation annealing on the void size distribution in a 304L stainless-steel specimen irradiated at 430°C to 1.4×10^{22} neutrons/cm^2.[6]

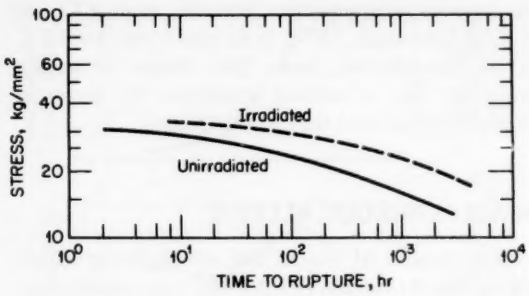

Fig. IV-4 Stress-rupture properties of 16/13 CrNi steel at 650°C before and after irradiation at 100°C to 0.81×10^{22} neutrons/cm^2.[7]

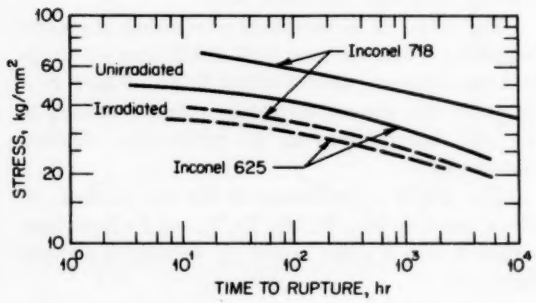

Fig. IV-5 Stress-rupture properties of Inconel 625 and Inconel 718 at 650°C before and after irradiation at 100°C to 0.81×10^{22} neutrons/cm^2.[7]

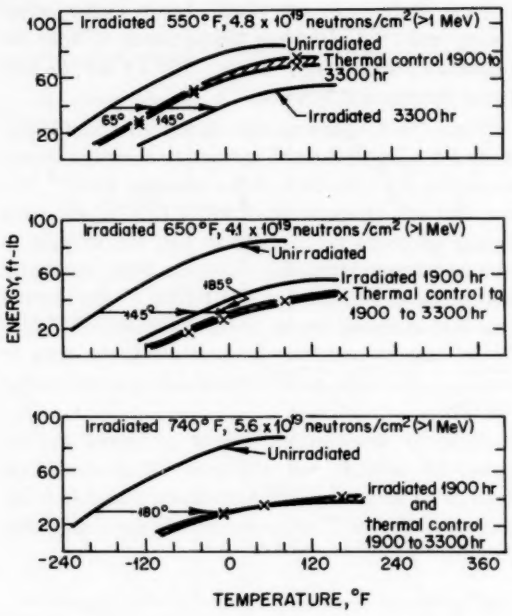

Fig. IV-6 Effect of temperature on the relative influences of irradiation and heat-treatment on Charpy V-notch ductility of 1-in.-thick 12 Ni–5 Cr–3 Mo maraging steel plate (160-ksi yield).[12]

Table IV-2 Effect of Fast-Neutron Irradiation on Tensile Properties of Tantalum[14]

Neutron fluence ($E_n \geq 1$ MeV), neutrons/cm^2	Test temp., °C	0.2% offset yield strength, kg/mm^2	Ultimate tensile strength, kg/mm^2	Elongation in 2.54 cm, %
Unirradiated	25	25.2	29.9	43.5
8×10^{18}	25	32.0	41.3*	14.8
2×10^{19}	25	29.7	37.3	29.6
1.2×10^{20}	25	†	48.9*	5.0
1.2×10^{20} + 450°C anneal	25	47.3	47.3	11.0
1.2×10^{20} + 750°C anneal	25	49.9	50.5	6.5
Unirradiated	450	8.93	27.0	22.0
1.2×10^{20}	450	32.1	32.6*	12.0
Unirradiated	750	6.2	18.8	34.0
1.2×10^{20}	750	26.5	27.2*	15.0
Unirradiated	1050	3.9	10.6	>40.0‡
1.2×10^{20}	1050	5.6	11.7	>40.0‡

*Upper yield point represents point of maximum load.
†Specimen strain did not reach 0.2% offset point.
‡Specimen not tested to failure.

Table IV-3 Effect of Fast-Neutron Irradiation on Tensile Properties of Ta–10 W Alloy[14]

Neutron fluence ($E_n \geq 1$ MeV), neutrons/cm^2	Test temp., °C	0.2% offset yield strength, kg/mm^2	Ultimate tensile strength, kg/mm^2	Elongation in 2.54 cm, %
Unirradiated	25	48.9	54.2	35.0
8×10^{18}	25	*	73.5†	4.1
2×10^{19}	25	*	77.4†	2.0
1.2×10^{20}	25	*	90.7	1.0
1.2×10^{20} + 450°C anneal	25	76.9	84.6†	2.0
1.2×10^{20} + 750°C anneal	25	67.2	70.0†	9.0
Unirradiated	450	26.9	39.4	22.0
1.2×10^{20}	450	53.1	53.7†	nil
Unirradiated	750	17.9	33.2	23.0
1.2×10^{20}	750	‡	36.1	15.0
Unirradiated	1050	13.2	22.6	38.0
1.2×10^{20}	1050	14.8	23.5	>40.0§

*Specimen strain did not reach 0.2% offset point.
†Upper yield point represents point of maximum load.
‡Extensometer malfunctioned.
§Specimen not tested to failure.

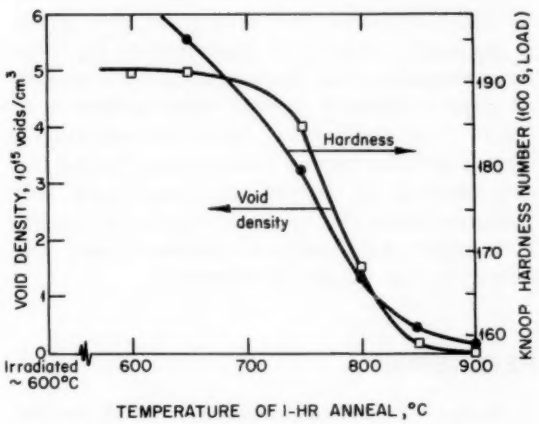

Fig. IV-7 Effect of postirradiation annealing temperature on void density and hardness of unalloyed vanadium following irradiation in EBR-II at 630°C to 1.7×10^{22} neutrons/cm^2 (total).[4] Void density and hardness as irradiated were 5×10^{15} cm^{-3} and 206 to 219 KHN, respectively.

BASIC MECHANISMS OF RADIATION DAMAGE IN NONFUEL MATERIALS

The influence of neutron irradiation of the Portevin–Le Chatelier effect (serrated yielding) in hydrogenated palladium has been investigated.[16] It had been found previously that the presence of hydrogen caused serrated yielding in palladium. The results of tensile tests on palladium specimens in various conditions are shown in Fig. IV-8. Serrated yielding appears only in the unirradiated hydrogenated specimen, suggesting that irradiation suppresses serrated yielding. The interstitial hydrogen is apparently trapped by the radiation-induced point defects, leaving the dislocations unlocked and preventing serrated yielding.

Samples of zirconium containing 0.03 wt.% ^{10}B were irradiated at 350°C until 3.4 cm^3 of helium per cubic centimeter of zirconium was produced as a result of (n,α) reactions.[17] The irradiated sample was subsequently annealed at temperatures ranging from 700 to 1000°C. It was found that no gas was released below 700°C, and about 50% was released by the anneal at 1000°C. The anneal at 1000°C resulted in a 12% density decrease.

The Japanese[18] found that the grain growth in Al–Li alloys was inhibited by the presence of helium bubbles at 550°C. Heat-treating unirradiated specimens caused appreciable grain growth.

The dependence of the yield stress of vacuum-annealed and hydrogen-purified iron polycrystals on neutron fluence and annealing temperature and the influence of these two parameters on the effect of static strain aging have been investigated.[19] The radiation hardening was found to depend sensitively on the interstitial impurities nitrogen and carbon. This may be explained by both a nucleation of precipitation

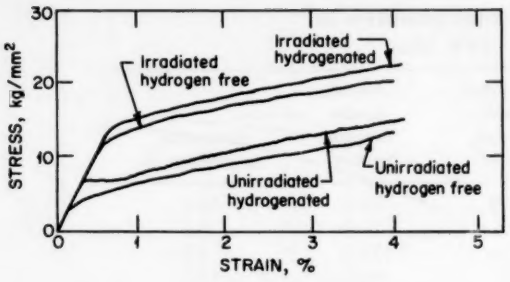

Fig. IV-8 Influence of radiation damage on the Portevin–Le Chatelier effect in hydrogenated palladium (0.15 at.% hydrogen; testing temperature = −196°C; $\epsilon = 1.37 \times 10^{-4}$/sec).[16]

and a trapping of the impurities at radiation-produced intrinsic defects. The radiation-enhanced precipitation predominates in the relatively impure iron samples at low fluences and may be eliminated by annealing at 190°C. The trapping becomes effective at higher fluences or in higher purity iron. Below 400°C two recovery stages for the yield stress are observed, one between 200 and 260°C and the other between 320 and 400°C. These may be explained by the detrapping of nitrogen and carbon, respectively. The static strain aging was found to be reduced by neutron irradiation. It reappears after annealing at temperatures at which the precipitates are thought to be redissolved and the carbon and nitrogen atoms to be detrapped.

Annealed tungsten wire was irradiated to a fast fluence of 10^{17} neutrons/cm^2 (>1 MeV), and specimens for field-ion microscopy were prepared from the wire.[20] Vacancies would be identified in certain regions of the field-ion microscope image, and the size and shape of small clusters of vacancies could be found by careful field evaporation. Using the field-evaporation technique, the investigators followed the clustering of vacancies in specimens that were unirradiated, irradiated, and given certain postirradiation heat-treatments. The only interstitial defects seen arose from impurities. Specimens examined after being annealed in stage III (~400°C) showed fewer single vacancies, and there was a simultaneous increase in the number of small vacancy clusters. It is concluded that stage III annealing in tungsten may be associated with the migration of single vacancies to small clusters, rather than the migration of defects.

The recovery of rhenium after neutron irradiation at ~390°K was studied[21] up to 1130°K by means of electrical-resistivity measurements at 4.2°K. Two irradiations were performed in the BR2 reactor at Mol: one up to a fluence of 7.6×10^{18} neutrons/cm^2 ($E > 1$ MeV) and the other up to fluences of 3.2×10^{19} neutrons/cm^2 (thermal) and 1.8×10^{18} neutrons/cm^2 ($E > 1$ MeV). The radiation-induced resistivity change is only partially recovered at 1130°K, where the annealing of defects is supposed to be complete. This effect is attributed to the transmutation of rhenium into osmium and tungsten. The annealing spectrum between 400 and 1130°K consists of several peaks, the main peak occurring at about 650°K ($0.19T_m$) preceded by a subpeak at about 620°K. The latter is more clearly resolved for the lower irradiation level. This is also the case for the minor peaks occurring at about 490 and 540°K. Toward higher temperature, continuous recovery occurs in the temperature interval 800 to 1000°K, whereas a small annealing stage has been observed at about $0.32T_m$. The $0.19T_m$ stage shows a peak shift toward lower temperatures for higher defect concentration. It is believed that this stage corresponds to stage III of the pure face-centered cubic metals.

It was shown experimentally that in metals irradiated by fast neutrons, heat capacity and thermal electromotive-force measurements (emf) are altered by the radiation-induced point defects and other defects in the crystal structure.[22] Measurements by differential thermal analysis showed that the heat capacity of copper increased by 8% after irradiation to 8×10^{17} fast neutrons/cm^2. These data were used for the calculation of vacancy concentration. Thermal emf data obtained for molybdenum demonstrated that irradiation alters the electronic capacity of metals. Furthermore, it is possible to calculate vacancy concentrations from changes in induced emf.

REFERENCES

1. *Irradiation Effects in Structural Alloys for Thermal and Fast Reactors,* a symposium presented at the 71st Annual Meeting of the ASTM, San Francisco, Calif., June 23–28, 1968, American Society for Testing and Materials, Special Technical Publication No. 457, 1969.
2. F. A. Comprelli, H. J. Busboom, and M. F. Gebhardt, Mechanical Properties of Irradiated Type 304 and Type 316 Stainless Steel in Fast Reactors, USAEC Report GEAP-10062, General Electric Company, Breeder Reactor Development Operation, June 1969.
3. A. L. Ward, Tensile Properties of Fast Reactor Irradiated AISI Type 316 Stainless Steel, *Trans. Amer. Nucl. Soc.*, 12(2): 584 (November 1969).
4. P. Patriarca and D. J. Rucker (Comps. and Eds.), Fuels and Materials Development Program Quarterly Progress Report for Period Ending June 30, 1969, USAEC Report ORNL-4440, Oak Ridge National Laboratory, October 1969.
5. E. E. Bloom and J. O. Stiegler, Recent Observations of

Irradiation Induced Void Formation in Austenitic Stainless Steels, *Trans. Amer. Nucl. Soc.*, **12**(2): 589 (November 1969).

6. J. O. Stiegler and E. E. Bloom, The Effects of Large Fast-Neutron Fluences on the Structure of Stainless Steel, *J. Nucl. Mater.*, **33**(2): 173-185 (November 1969).
7. H. Böhm, H. Hauck, W. Leo, and C. Wassilew, Postirradiation Creep-Rupture Properties of Austenitic Stainless Steel and Nickel-Base Alloys, *J. Nucl. Mater.*, **33**(3): 343-346 (December 1969).
8. H. Böhm, H. Hauck, and G. Hess, Influence of Cold Working and Recrystallization on the Radiation Induced High Temperature Embrittlement of Austenitic Steels, *J. Nucl. Mater.*, **33**(3): 347-351 (December 1969).
9. J. L. Brimhall and B. Mastel, Stability of Voids in Neutron Irradiated Nickel, *J. Nucl. Mater.*, **33**(2): 186-194 (November 1969).
10. J. P. Shepherd, Irradiation-Induced Precipitation in a Niobium Stabilized Stainless Steel, *Metal Sci. J.*, **3**: 229-234 (November 1969).
11. M. B. Watson and B. L. Wotton, Comparison of Transition Temperatures Indicated by Charpy V-Notch and Subsize Izod Impact Specimens for Irradiated 3½% and 9% Nickel Steel, Canadian Report AECL-3370, October 1969.
12. R. A. Dray, Jr., and J. R. Hawthorne, Behavior of Mechanical Properties in Neutron Irradiated 12 Ni–5 Cr–3 Mo Maraging Steel Plate and Companion Weld Metals, USAEC Report NRL-6945, Naval Research Laboratory, June 6, 1969.
13. T. Fujimur and C. Nakazaki, Neutron Irradiation Test on Reactor Pressure Vessel Steel (A-302B Steel) Weldment, *Yosetsu Gakkaishi*, **38**: 608-614 (June 1969).
14. General Electric Company, Nuclear Systems Programs, AEC Fuels and Materials Development Program, Eighth Annual Report, USAEC Report GEMP-1012, Part 1, Mar. 31, 1969.
15. J. L. Kamphouse, D. A. Myers, and J. Moteff, Hot-Microhardness Values for Metals and Alloys (Irradiated and Unirradiated), USAEC Report GEMP-716, General Electric Company, Nuclear Systems Programs, December 1969.
16. J. S. Blakemore, The Influence of Irradiation Damage on the Portevin–Le Chatelier Effect in Hydrogenated Palladium, *J. Nucl. Mater.*, **34**(1): 114-115 (January 1970).
17. E. F. Davydov and V. V. Kolesov, Some Results of Studying the Behavior of an Irradiated Zr–B Alloy During Annealing, *At. Energ. (USSR)*, **27**: 57-59 (July 1969).
18. K. Shiraishi and K. Fukaya, Grain Growth and Neutron Irradiation Effects in Al–Li Alloys, *J. Nucl. Sci. Technol. (Tokyo)*, **6**: 663-664 (November 1969).
19. G. P. Seidel, Neutron Radiation Hardening of Polycrystalline Iron, *Radiat. Eff.*, **1**: 177-190 (July 1969).
20. K. M. Bowkett and B. Ralph, Annealing of Radiation Damage in Tungsten Investigated by Field–Ion Microscopy, *Proc. Roy. Soc. (London), Ser. A*, **312**: 51-63 (Aug. 26, 1969).
21. H. Vandenborre, L. Stals, and J. Nikoul, High Temperature Recovery of Neutron Irradiated Rhenium, *Phys. Status Solidi*, **35**: 1009-1015 (October 1969).
22. K. S. Pedchenko, V. S. Karasev, and V. M. Trikula, Effect of Neutron Irradiation on Some Thermophysical Characteristics of Metals, *Inzh.-Fiz. Zh.*, **17**: 665-672 (October 1969).

Section V

Reactor Materials

Nonfueled Refractories

By D. R. Lankard

STRUCTURAL CERAMICS

Canadian workers are investigating the use of structural ceramics under tension in a nuclear environment.[1] The fracture behavior of Lucalox, Poco graphite, and KT SiC was studied in four-point bending tests and compared with that obtained on the zirconium alloy Ozhennite. The distribution of fracture-stress measurements in the ceramic materials was analyzed using Weibull statistics. The Weibull distribution function is based on a series failure model. Data of the type obtained in these analyses are useful in design concepts based on knowledge of the probability of failure of these brittle materials at a particular stress.

The ceramics investigated were thought to merit consideration for use in applications under tensile-stress conditions because of their demonstrated short-time strength at low probabilities of failure. Relative to other ceramics, Poco graphite and KT SiC show low variability of measured strength properties. Work-of-fracture values for the ceramics, approximately 5×10^{-4} erg/cm, are discussed in relation to their microstructure.

NIOBIUM CARBIDE

Workers at Los Alamos Scientific Laboratory[2] have studied the temperature dependence of Young's modulus and the shear modulus of polycrystalline $NbC_{0.969}$ with a density 95.8% of theoretical. Niobium monocarbide rods (¼-in. diameter) were hot pressed at 3050°C and 2400 psi for 10 min. The specimen was made by molybdenum-brazing two 2-in. lengths together at about 2625°C in argon.

The Young's modulus of $NbC_{0.969}$ follows Wachtman's equation and is best represented as $E = 4.6039 \times 10^{12} - 5.7289 \times 10^{8}\ T \exp(-200.5/T)$ dynes/cm^2 from 285 to 2173°K. The shear modulus of $NbC_{0.969}$ is best represented as $G = 1.9286 \times 10^{12} - 2.4848 \times 10^{8}\ T$ dynes/cm^2 from 284 to 2173°K. Above 2173°K the moduli decrease rapidly, possibly because of viscous grain-boundary slip.

The dilatometric linear thermal expansion of $NbC_{0.969}$ is 2.04% from 17 to 2447°C.

Niobium carbide–graphite composites are being investigated at Los Alamos[3] for their suitability in structural applications involving both elevated temperatures and thermal-shock conditions. Test specimens were prepared by hot-pressing graphite–NbC powder mixtures at 3000°C in an argon atmosphere. Data on the elastic and shear moduli of the composites, obtained as a function of carbide content using an ultrasonic pulse-echo technique, are shown in Fig. V-1.

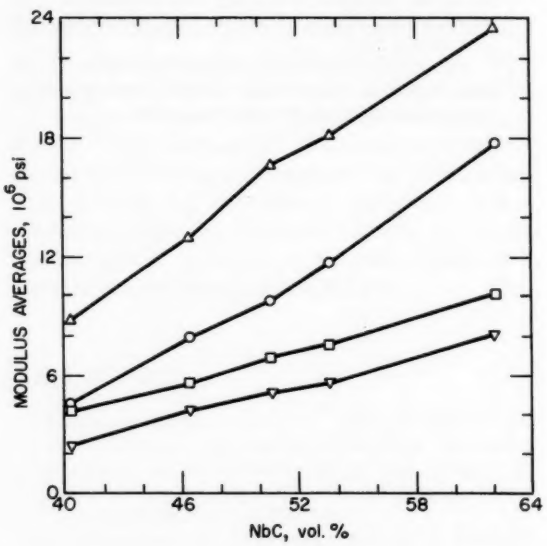

Fig. V-1 Effect of NbC content on elastic moduli of NbC–C composites.[3] ▽, shear modulus, weak direction; ○, Young's modulus, weak direction; □, shear modulus, strong direction; △, Young's modulus, strong direction.

RARE-EARTH OXIDES

Workers at the Iowa State University have reported on the room-temperature elastic properties[4] and

elevated-temperature elastic properties[5] of Y_2O_3, Dy_2O_3, Ho_2O_3, and Er_2O_3 as part of a continuing investigation of the elastic properties of rare-earth oxides. Bar-shaped specimens (¼ by ¼ by 4 in.) were isostatically pressed at 50,000 psi from powders prepared from calcined oxyacid salts of the rare earths. Specimens of varying porosity were produced by altering the firing temperature from 1700 to 2100°C.

Data obtained on the room-temperature elastic and shear moduli of the rare-earth oxides, using the sonic-resonance technique, were fitted to three different empirical relations that predict the porosity dependence of the two moduli. The results of this effort, presented in Tables V-1 and V-2, show how well each of the empirical equations describes the room-temperature elastic behavior of each of the rare-earth oxides studied and how the Young's and shear moduli of polycrystalline yttria, dysprosia, holmia, and erbia decrease with increasing porosity. The room-temperature Poisson's ratio of each oxide also decreases with increasing porosity in the porosity range studied.

The Young's and shear moduli of rare-earth oxide specimens from the room-temperature study (except dysprosia) were determined from room temperature to 1000°C, using the sonic-resonance technique. The Young's, shear, and bulk moduli of polycrystalline Y_2O_3, Ho_2O_3, and Er_2O_3 were shown to decrease linearly by about 11% from room temperature to 1000°C. This relation was observed in specimens having porosities ranging from 3.8 to 21.8%. The Poisson's ratio (μ) of the rare-earth oxides, calculated from the relation $\mu = \frac{E}{2G} - 1$, was not influenced by temperature up to 1000°C.

CONCRETE

Franklin Institute Research Laboratories has published a thorough review[6] of the current practices in the design and construction of prestressed-concrete and reinforced-concrete containments for both pressurized-water and boiling-water reactors for civilian power. The effects of operating and environmental

Table V-1 Values of Constants Obtained by Least-Squares Fitting of Empirical Equations Proposed for the Effect of Porosity on the Young's Modulus[4]

			Linear equation $E = E_0(1 - \alpha P)$			Spriggs equation $E = E_0 e^{-bP}$			Hasselman equation $E = E_0\left[1 - \frac{AP}{1 + (A-1)P}\right]$		
Material	Porosity range, %	No. of data points	E_0, kbars	α	Error,* %	E_0, kbars	b	Error,* %	E_0, kbars	A	Error,* %
Y_2O_3	4 to 22	17	1715.0	2.02	1.2	1798.1	2.81	2.0	1832.4	3.17	2.2
Dy_2O_3	3 to 19	22	1629.5	2.13	1.9	1678.6	2.81	1.4	1691.0	3.04	1.3
Ho_2O_3	1 to 18	21	1694.0	2.09	1.9	1728.6	2.62	1.9	1737.6	2.78	2.0
Er_2O_3	5 to 21	27	1752.1	2.11	2.2	1823.4	2.90	2.3	1844.1	3.23	2.4

*The standard error of estimate divided by the mean value of the Young's modulus.

Table V-2 Values of Constants Obtained by Least-Squares Fitting of Empirical Equations Proposed for Effect of Porosity on the Shear Modulus[4]

			Linear equation $G = G_0(1 - \alpha P)$			Spriggs equation $G = G_0 e^{-bP}$			Hasselman equation $G = G_0\left[1 - \frac{AP}{1 + (A-1)P}\right]$		
Material	Porosity range, %	No. of data points	G_0, kbars	α	Error,* %	G_0, kbars	b	Error,* %	G_0, kbars	A	Error,* %
Y_2O_3	4 to 22	17	665.0	1.97	1.6	694.2	2.70	2.0	703.1	2.96	2.1
Dy_2O_3	3 to 19	22	626.9	2.03	1.8	644.0	2.63	1.5	641.7	2.72	1.6
Ho_2O_3	1 to 18	21	656.4	2.04	1.8	669.2	2.55	2.0	672.8	2.69	2.4
Er_2O_3	5 to 21	27	677.8	2.10	1.9	704.9	2.86	2.1	712.8	3.17	2.1

*The standard error of estimate divided by the mean value of the shear modulus.

conditions on the structural behavior of containment structures are discussed. The loads that may act separately or be superimposed on the structure include dead load, live load, wind load, earthquake load, impact and lateral forces from cranes, steady-state thermal loads, and prestressing forces.

The modes of concrete-containment-vessel failure are examined as they relate to structural-design concepts. The methods and procedures of design analysis are discussed, including the computer approaches that have been utilized. One design approach has been through the use of structural-model testing.

The qualifications and properties of concrete are included as they relate to the fabrication and use of a containment vessel. Factors contributing to the deterioration of concrete in service are discussed, as are factors influencing such pertinent properties of concrete as permeability, shrinkage, elastic behavior, creep, and thermal properties.

Limitations of the codes and standards applied in the current technology are identified.

The University of Illinois[7] has been studying the structural response and modes of failure of prestressed-concrete reactor vessels. An objective of this work was to develop analytical techniques to predict the behavior and strength of these structures.

A series of tests on small-scale pressure vessels was conducted. The test vessels were of cylindrical configuration with flat end slabs, subjected to internal pressure only. Concrete used in the construction of the test vessels had compressive strengths ranging from 4955 to 7650 psi.

Several modes of failure were observed in the model vessels at maximum pressures ranging from 240 to 3690 psi, including both flexural and shear failures in the end slab. A computer program was developed which made it possible to predict crack patterns in the vessel, as well as strains and stresses before and after cracking of the concrete.

REFERENCES

1. R. Stevens and T. D. Clausen, Strength Distribution and Fracture Behavior of Structural Ceramics of Low Neutron Absorption Cross Section, Canadian Report AECL-3422, October 1969.
2. R. F. Brenton, C. R. Saunders, and C. P. Kempter, Elastic Properties and Thermal Expansion of Niobium Monocarbide to High Temperatures, *J. Less-Common Metals*, **19**: 273-278 (November 1969).
3. H. L. Brown and C. P. Kempter, The Composition Dependence of Elastic Properties of Niobium Carbide–Graphite Composites, *Planseeber. Pulvermet.*, **15**(3): 167-173 (December 1967).
4. W. R. Manning, O. Hunter, Jr., and B. R. Powell, Jr., Elastic Properties of Polycrystalline Yttrium Oxide, Dysprosium Oxide, Holmium Oxide, and Erbium Oxide: Room-Temperature Measurements, *J. Amer. Ceram. Soc.*, **52**(8): 436-442 (August 1969).
5. W. R. Manning and O. Hunter, Jr., Elastic Properties of Polycrystalline Yttrium Oxide, Holmium Oxide, and Erbium Oxide: High-Temperature Measurements, *J. Amer. Ceram. Soc.*, **52**(9): 492-496 (September 1969).
6. C. P. Tan, A Study of the Design and Construction Practices of Prestressed Concrete and Reinforced Concrete Containment Vessels, USAEC Report TID-25176, Franklin Institute Research Laboratories, August 1969.
7. S. L. Paul, M. A. Sozen, W. C. Schnobrich, B. I. Karlsson, and A. Zimmer, Strength and Behavior of Prestressed Concrete Vessels for Nuclear Reactors: Vols. I and III, *Structural Research Series* 346, University of Illinois.

Section VI

Reactor Materials

Corrosion of Base-Metal Alloys in Aqueous and Gaseous Media

By W. E. Berry

REVIEWS AND MISCELLANEOUS STUDIES

A compilation of papers on stress-corrosion cracking presented at Ohio State University in September 1967 has now been published.[1] The papers, authored by experts in the field, cover the theories, mechanisms, contributory factors, and sophisticated techniques for studying the phenomenon. The compilation contains some 45 papers on the stress-corrosion cracking of noble-metal alloys, Fe–Cr–Ni alloys, high-strength steels, aluminum alloys, and titanium alloys.

The corrosion rates of various materials in the Nuclear Power Demonstration (NPD) reactor primary circuit since its conversion from pressurized-water to boiling-water conditions have been summarized by Chalk River.[2] There was no increase in the corrosion rates after reactor conversion for 304 and 410 stainless steel, Monel 400, Inconel 600, Zircaloy-2, Zircaloy-4, or Zr–2.5 Nb alloy. Steel specimens exhibited higher rates after conversion than before. This was attributed to frequent shutdowns after conversion which could have allowed low-temperature oxygenated conditions in the test autoclave. The fact that there was little change in the corrosion rates of Monel 400 and Zr–2.5 Nb alloy was cited as indicating that the conversion to boiling, with ammonia additions, has not resulted in more oxidizing conditions.

The corrosion products formed on reactor materials in deoxygenated *p*H 10 (NH_4OH) water at 280°C have been examined in the scanning electron microscope by Battelle–Northwest.[3] The reactor materials were Zircaloy-2, Inconel 600, 304 stainless steel, and mild steel. Most of the product species were within the size range 0.2 to 2 μ. Corrosion products tended to become less crystalline and smaller as the water velocity increased from 0 to 30 ft/sec. Analyses of the products revealed that nickel and chromium were relatively mobile either within the corrosion film or in the fluid. Of the materials studied, Zircaloy-2 surfaces had the least amount of corrosion product deposited from foreign sources, and the iron-base alloys had the most.

CORROSION OF ALUMINUM

Du Pont has investigated the inhibiting effects of lithium silicate on the corrosion of aluminum cladding on fuel elements in Savannah River reactors.[4] Fuel tubes were treated to form a 1-μ-thick surface film of lithium aluminosilicate, and the heavy-water moderator was treated with a maximum of 0.5 ppM combined soluble and polymeric silica. After the surface treatment, the corrosion rate was about half that of the untreated alloy after 4 days, but the rate increased to about the same value after 10 days. Treated and untreated surfaces exhibited the same oxide thickness after long-term exposure (60 days). However, the addition of silica to the moderator decreased the corrosion rate of both treated and untreated aluminum surfaces. The silica addition also reduced the turbidity in the moderator by reducing the concentration of hydrated aluminum oxides to <0.5 ppM.

Rocketdyne has issued a final report[5] on the effects of point defects on the stress-corrosion cracking susceptibility of aluminum 7075 in the T6, T73, and intermediate heat-treated conditions. Point defects were introduced by irradiation to a fast-neutron dosage of 0.8×10^{19} neutrons/cm^2. Tensile specimens stressed to 25, 50, and 75% of their yield strength were subjected to alternate immersion in 3.5 wt.% NaCl solution. The irradiation caused a 50% reduction in the stress-corrosion cracking failure time of 7075-T6 but appeared to have no effect on failure of specimens in the other heat-treated conditions. Back-reflection ultrasonic monitoring detected crack initiation and propagation and revealed that crack initiation is the rate-controlling step, consuming ~90% of the total time to failure. The cracks were shown to initiate at several sites.

CORROSION OF FERROUS ALLOYS

Low-Alloy Steels

Means of protecting the nongrouted tendons of the prestressed-concrete reactor vessel of the Fort St. Vrain

Nuclear Generating Station have been investigated at Gulf General Atomic.[6] The steel wire conformed to ASTM Specification A421-65, Type BA. It was cold worked and thermalized (simultaneous stress and heat) to an ultimate tensile stress of 225 to 260 ksi. Marine atmosphere exposure tests at La Jolla, Calif., indicated that a suitable combination of protective coatings and wraps would protect the tendons from rusting during fabrication, shipment, installation, and operation in the reactor. Studies with bare and coated notched specimens revealed that the tendons were not susceptible to stress-corrosion cracking or hydrogen-stress cracking.

Precipitation-Hardening Stainless Steels

The stress-corrosion-cracking behavior of precipitation-hardening stainless steels has been studied at the George C. Marshall Space Flight Center.[7] Bent beams, loaded tensile specimens, and C rings were used to test the materials in the longitudinal and transverse directions of grain orientation. The stressed specimens were alternately immersed (10 min) in 3.5 wt.% NaCl solution and air dried (50 min) at room temperature. The results indicated that PH13-8Mo, PH14-8Mo, 15-5PH, A-286, Almar 362, and Unitemp 212 stainless steels were resistant to stress-corrosion cracking under these conditions in all heat-treatments studied. The PH15-7Mo and 17-7PH alloys were susceptible to stress-corrosion cracking in all conditions studied, except 17-7PH–CH900. The 17-4PH–H900 treated specimen cracked in the transverse grain direction. The AM-350 was susceptible to cracking in the SCT 850 condition but not in the SCT 1000 condition.

Austenitic Stainless Steels

The corrosion of irradiated 304 stainless-steel cladding on Experimental Breeder Reactor II (EBR-II) fuel pins during storage in fuel-storage-basin water has been investigated at the Idaho Nuclear Corp.[8] The cladding had been sensitized as the result of its residence at 500°C in the sodium-cooled reactor. Five fuel pins were stored for 2 years in the fuel-storage-basin water (groundwater containing 200 ppM $NaNO_3$ inhibitor) at the Idaho Chemical Processing Plant. Periodic leak testing of the pins and comparison of these results with similar tests using unclad irradiated pin segments revealed that no significant penetration of the cladding occurred during the 2 years of storage.

Laboratory tests conducted by Combustion Engineering and Ohio State University have shown that sensitized 304 and 316 stainless steels will exhibit intergranular attack in water containing fluorides, providing one or more of the following conditions exist: (1) applied or residual tensile stress; (2) cold work, with or without macro stress; (3) a crevice; (4) visible oxide film formed by exposure to air at elevated temperature.[9] Intergranular attack occurred over the temperature range 80 to 180°F (25 to 85°C) at *p*H 4.96 to 10.45 with fluoride levels of <1 to 542 ppM. The above-mentioned conditions did not cause intergranular attack of sensitized Inconel 600, Incoloy 800, 304L stainless steel, 347 stainless steel, or austenite–ferrite weld deposits or castings.

Surface treatments with lithium silicate have prevented stress-corrosion cracking of sensitized and intergranularly corroded 304 stainless steel in studies conducted at Savannah River.[10] The corrodent was 90°C water adjusted to *p*H 4.5 HNO_3 and containing 20 ppM chloride. Sensitized samples were overpickled in HNO_3–HF, stressed, and given one of the following treatments in 25 wt.% lithium silicate.

1. None.
2. Dipped, rinsed, and air dried.
3. Dipped and air dried (no rinse).
4. Boiled 0.5 hr in saturated NaCl solution, dipped in lithium silicate, rinsed and dried.
5. Boiled 0.5 hr in saturated NaCl, dipped in lithium silicate, and air dried, no rinse.

Upon exposure to the test medium at 90°C, cracks developed within 48 hr in the untreated samples. After 890 hr of exposure, there were cracks in 1 of 8 of the NaCl dipped-and-rinsed samples and in 0 to 8 of the samples given other treatments (total exposure 890 hr). The silicate also prevented rusting of the sensitized stainless steel.

The effect of alloy additions on the stress-corrosion cracking of Fe–Cr–Ni alloys in boiling $MgCl_2$ solutions has been studied at Ohio State University.[11] Nickel additions in the 5 to 15 wt.% range produced the usual maximum susceptibility to stress-corrosion cracking. Chromium additions in the range 10 to 15 wt.% to binary Fe–Ni alloys produced maximum resistance to cracking. Alloys containing 10 to 15 wt.% chromium and 10 to 15 wt.% nickel plus small additions of aluminum, beryllium, and copper were particularly resistant. Of the fourth-component additions to an Fe–20 Cr–15 Ni alloy, the elements of the platinum group (Pt, Ir, Os, Rh, Ru, Pd), group VA (N, P, As, Sb, Bi), and molybdenum produced the most deleterious effects. The most beneficial additions were Al, Be, C, Si, and possibly B.

Results of examinations of cracking failures in the upper-liquid-level line in the Elk River reactor have

been reported by Southwest Research Institute.[12] Three leaks were detected in the furnace-sensitized 304 stainless-steel pipe. They were intergranular and initiated on the inside diameter of the pipe at the toe of a socket weld and in a ground area on the inside diameter surface of the pipe. Secondary cracks 5 to 60 mils deep were also found on the inside diameter surface. Some intergranular cracking was found in a worked depression on the external surface of the pipe. All three cracks were located in the vicinity of weld deposits. It was concluded that stress corrosion caused the failures.

A review of the literature on the stress-corrosion cracking of iron, nickel, chromium, and their alloys in caustic solutions has been prepared by Ohio State University.[13] The review, prepared in support of the LMFBR Program, was based on the possibility that an accident or leak could permit oxidation or hydration of the sodium to produce NaOH–Na_2O–H_2O solutions. Accordingly the environment considered was primarily NaOH–H_2O over a broad temperature range. Information is presented in areas of thermodynamics, electrochemical kinetics, corrosion rates, stress-corrosion-cracking phenomena, structures of passive films, and inhibitors.

CORROSION OF NICKEL-BASE ALLOYS

Oak Ridge is studying the corrosion behavior of welds in several high-temperature alloys in steam at 595 and 650°C. Corrosion tests were conducted in loops installed in the Bartow Plant of Florida Power.[14] The weight gains of dissimilar-metal weldments of Incoloy 800 to Inconel 625, Hastelloy X, or IN-102 were $\lesssim$3.5 mg/cm^2 after 6000 hr at 650°C, and the oxide films were uniform and tenacious. The weight gains of weldments between similar metals of 304 stainless steel, Inconel 600, Incoloy 800, Inconel 625, Hastelloy X, and IN-102 were less than 0.65 mg/cm^2 after 6000 hr at 650°C. Stress-corrosion tests with U bends of the weldments on similar and dissimilar metals revealed no cracking after 4000-hr exposures at 595°C (steam contained <0.5 ppM chloride and <1 ppM oxygen).

CORROSION OF ZIRCONIUM ALLOYS

An English translation of a Soviet book entitled *Corrosion of Zirconium and Zirconium Alloys*, dated 1967, is now available.[15] The book covers both Western and Russian work on the corrosion and hydriding behavior of zirconium alloys under nuclear reactor conditions as influenced by alloying elements, heat-treatment, and other factors. Also discussed are the electrochemical behavior of zirconium in aqueous solutions and the influence of hydriding and radiation on the oxidation and mechanical properties of zirconium alloys. The translation has 174 pages and cites 310 references.

The effect of emergency core cooling on the behavior of Zircaloy-2 tubing has been studied at Idaho Nuclear.[16] As-received, pickled, prefilmed in 350°C steam, and pickled-plus-prefilmed specimens were exposed to steam while at 915 to 1315°C or during the entire heating and cooling cycles to these temperatures. The specimens were evaluated by visual, optical, and microprobe examinations, as well as by mechanical-property, weight, and electrical-resistivity changes. It was found that Zircaloy-2 underwent surface oxidation, oxygen absorption, grain growth, phase transformation, zirconium oxide precipitation, and embrittlement, depending on the time–temperature cycle. The loss of ductility (embrittlement) increased as a function of the time spent in the two-phase alpha–beta region after oxygen absorption. These results indicated that embrittlement of Zircaloy in emergency core cooling could be minimized by staying below or rapidly cooling through the two-phase region.

The effect of reactor irradiation on the internal surface area of corrosion films on Zircaloy-2 and Zr–2.5 Nb alloy has been studied at Harwell.[17] Specimens were exposed to steam or moist CO_2–air at 300 to 480°C in the DIDO reactor. Surface areas were determined from the adsorption of ^{133}Xe at 77°K. In the absence of radiation, the surface area of the oxide remained essentially constant for weight gains ranging from 9 to 141 mg/dm^2. On the other hand, the surface area of the irradiated specimens increased with increasing weight gain and was 2 to 40 times that of unirradiated specimens. Weight gains of the irradiated specimens ranged from 16 to 150 mg/dm^2. These results suggested that irradiation caused embrittlement and breakdown of the oxide film, although it should be noted that no increase in area was detected when unirradiated specimens experienced transition from a cubic to a linear oxidation rate.

The stress-corrosion-cracking behavior of zirconium and its alloys in methanol solutions is being studied at Chalk River.[18] Unstressed and stressed specimens of crystal-bar zirconium, Zircaloy-2, Zr–2.5 Nb, and Zr–2.5 Nb–0.5 Cu have been exposed to anhydrous (<0.1 wt.% H_2O) and commercial methanol (1 to 2 wt.% H_2O) and to methanol containing 0.001 to 1 wt.% iodine and 0.5 wt.% (HCl/3 vol.% H_2O) or

0.2 wt.% (HCl/0.6 vol.% H_2O) (but not in all combinations of alloys and environments). Cracking and embrittlement of stressed and unstressed specimens occurred in essentially all the environmental-alloy combinations studied. The cracks were intergranular in methanol/iodine solutions and initiated intergranularly in methanol/HCl solutions but propagated transgranularly in highly stressed specimens.

REFERENCES

1. R. W. Staehle, A. J. Forty, and D. van Rooyen (Eds.), Proceedings of Conference on Functional Aspects of Stress-Corrosion Cracking, Columbus, Ohio, September 11-15, 1967, National Association of Corrosion Engineers, 1969.
2. Atomic Energy of Canada Limited, unpublished data.
3. T. J. Kabele and J. L. Daniel, Corrosion Product Study by Scanning Electron Microscope, USAEC Report BNWL-1184, Battelle–Northwest, November 1969.
4. R. S. Ondrejcin, Silicates as Inhibitors of Aluminum Corrosion in Savannah River Reactors, USAEC Report DP-1197, Savannah River Laboratory, December 1969.
5. A. J. Jacobs and G. G. Bentle, The Effects of Point Defects and Dislocations on the Stress-Corrosion Susceptibility of Aluminum Alloys, Final Report R-7882, Rocketdyne Division of North American Rockwell, Aug. 29, 1969.
6. J. F. Hildebrand, Tests Relating to Corrosion Protection for Tendons of the Public Service Company of Colorado Prestressed Concrete Reactor Vessel, USAEC Report GA-9356, Gulf General Atomic, Aug. 6, 1969.
7. T. S. Humphries and E. E. Nelson, Stress-Corrosion Cracking Evaluation of Several Precipitation Hardening Stainless Steels, Report N-69-38232, National Aeronautics and Space Administration, Marshall Space Flight Center, Sept. 12, 1969.
8. C. A. Zimmerman and D. W. Rhodes, Integrity of Stainless Steel Cladding on EBR-II Fuel in Water, USAEC Report IN-1331, Idaho Nuclear Corp., October 1969.
9. C. T. Ward, D. L. Mathis, and R. W. Staehle, Intergranular Attack of Sensitized Austenitic Stainless Steel by Water Containing Fluoride Ions, *Corrosion*, 25(9): 394-396 (September 1969).
10. M. L. Holzworth and A. E. Symonds, Inhibition of Stress Corrosion in Type 304 Stainless Steel by Lithium Silicate, *Corrosion*, 25(7): 287-288 (July 1969).
11. J. J. Royuela, T. L. Raredon, E. Serrate, C. R. Morin, R. V. Farrar, and R. W. Staehle, Effect of Alloy Composition on the Stress-Corrosion Cracking of Fe–Cr–Ni Base Alloys, USAEC Report COO-1319-81, Ohio State University, Jan. 9, 1970.
12. H. C. Burghard, E. B. Norris, and R. D. Wylie, Examination of Upper Liquid Level Line from Elk River Reactor, USAEC Report SWRI-1228-P9-16, Southwest Research Institute, Feb. 27, 1969.
13. D. V. Subrahmanyam and R. W. Staehle, Stress-Corrosion Cracking and General Corrosion of Iron, Nickel, Chromium and Their Alloys in Caustic Solutions, USAEC Report COO-2018-4, Ohio State University, Feb. 2, 1970.
14. P. Patriarca (Comp.) and D. J. Rucker (Ed.), Fuels and Materials Development Program Quarterly Progress Report for Period Ending September 30, 1969, USAEC Report ORNL-4480, Oak Ridge National Laboratory, February 1970.
15. B. G. Parfenov, V. V. Gerasimov, and G. L. Venediktova, Corrosion of Zirconium and Zirconium Alloys, USAEC Report AEC-tr-6978, 1969, from the Soviet book of the same title, Atomizdat, Moscow, 1967.
16. E. D. Covington (Ed.), Reactor Engineering Branch Annual Report, Fiscal Year 1969, USAEC Report IN-1335, Idaho Nuclear Corp., November 1969.
17. R. C. Asher and J. F. White, Effect of Reactor Irradiation on the Internal Surface Area of Corrosion Films on Zirconium Alloys, *Nature*, 223(5205): 497 (Aug. 2, 1969).
18. Atomic Energy of Canada Limited, Chemistry and Materials Division, Progress Report, October 1–December 31, 1969, Canadian Report AECL-3521.

Section VII

Reactor Materials

Oxidation of Refractory Metals

By B. C. Allen

OXIDATION OF UNCOATED REFRACTORY METALS

Niobium

The oxidation of niobium in the form of 0.25-in.-diameter single-crystal spheres has been studied in 400 torrs of dry oxygen at 550 to 925°C at the University of Liverpool.[1] The results indicate that suboxide platelets were present below 600°C and produced lines of pores in the scale in a manner similar to that reported for tantalum. These lines of pores produced characteristic scale failures. Above 600°C, failure modes were different, and oxidation appeared to be isotropic.

Hafnium

The oxidation of hafnium in air or 1 atm of pure oxygen has been measured by the U. S. Air Force[2] at 600 to 1250°C using a thermogravimetric technique. Oxidation was essentially linear from 600 to 800°C and partially linear at higher temperatures. The activation energy for oxidation was 0.90 eV for 99.7 wt.% hafnium and 0.42 eV for 99.96 wt.% electron-beam-refined hafnium. Impurities (Zr, Si, W, and Mn) in the less-pure hafnium had substantial effects on oxidation behavior. X-ray diffraction and electron microscopy showed monoclinic HfO_2 above 550°C and preferential (associated with epitaxial dislocations) and random oxidation of hafnium above 600°C at 10^{-5} torr.

Oxidation of binary hafnium alloys containing 10 to 50 wt.% niobium has been studied[3a] at 800 to 1300°C. The oxygen pressure was generally 10 torrs, but the pressure was varied from 10^{-3} to 760 torrs for Hf–35 Nb. Experimental methods included thermogravimetric measurements and the use of X-ray diffraction, metallography, and electron microprobe. The major reaction products were HfO_2, Nb_2O_5, and $Nb_2O_5 \cdot 6HfO_2$. The relative amounts were a function of temperature, oxygen pressure, and reaction time. At 10 torrs of oxygen and above, oxidation of the alloys exhibited an irregular temperature dependence, with a maximum in the range 950 to 1000°C and an increasing rate above 1100°C. In the vicinity of the maximum, the rates approximated those of unalloyed niobium. Below 0.1 torr of oxygen, the maximum was absent. The maximum was interpreted as a result of interplay between relative rates of formation of HfO_2 and Nb_2O_5 and their subsequent reaction to form $Nb_2O_5 \cdot 6HfO_2$.

Tantalum

Bell Laboratories[4] has presented results for oxidation of sputtered tantalum films between 100 and 525°C. These films consisted of body-centered cubic tantalum, beta tantalum, porous beta tantalum, and Ta_2N, and showed parabolic oxidation behavior with the formation of adherent Ta_2O_5 or tantalum oxynitride films. The first three films dissolved about 12 at.% oxygen, which is higher than the oxygen solubility in bulk tantalum. Furthermore, they showed a different degree of suboxide formation compared with bulk tantalum. Activation energies for oxygen diffusion in the metal and for oxide growth were 1.2 and 1.4 eV, respectively. The dielectric properties of the oxide scales were discussed in terms of defects in the oxide.

Tungsten

The oxidation of tungsten containing typically 10 wt.% chromium and 1 wt.% palladium has been investigated in British work.[3b] Typical lives for 0.5-cm-diameter cylinders were 500 hr at 1200°C, 100 hr at 1400°C, and 1 hr at 1800°C. The alloys showed weight-gain rates during their oxidation life in the range 0.01 to 1.5 mg/(cm^2)(hr), but they eventually failed catastrophically. The oxidation resistance was unaffected by severe thermal cycling, and the alloys showed good self-healing characteristics. The protection mechanism appeared to depend on an oxidation-resistant palladium-rich phase that formed at the surface.

Flash desorption plus mass spectrograph,[5] field ion emission,[6] mass spectrograph,[7] and secondary ionic–ionic emission[8] were used to investigate tungsten–oxygen interactions. A theoretical quasi-equilibrium treatment of gas–solid reactions has been applied to published flash-desorption data.[9] Contamination studies of interstitials in tungsten, tantalum, and tantalum alloys have been reported[10,11a] in a variety of vacuums at temperatures up to 1800°C.

Chromium

The transition kinetics during linear to parabolic oxidation of chromium in moist hydrogen have been measured thermogravimetrically.[11b] On the basis of a cation-deficit defect structure for Cr_2O_3, the transition followed a model first proposed by C. Wagner. Under conditions not far removed from the Cr, Cr_2O_3, H_2O–H_2 equilibrium, the linear region of oxidation was controlled by the adsorption and dissociation of H_2O on Cr_2O_3. The phase-boundary reaction was dependent on the concentration of cation vacancies at the Cr_2O_3/gas-phase boundary.

PROTECTION OF REFRACTORY METALS BY COATING

T-222 and FS-85 Alloys

In its continuing coating development and evaluation program, Solar[12] investigated a series of silicided Mo–W–Ti–V modifier alloys for their ability to protect T-222 tantalum and FS-85 niobium. One of the better modifier alloys, 50 W–20 Mo–15 Ti–15 V, yielded a silicide coating that provided protection (1) in cyclic (room temperature to 1315°C) furnace oxidation for over 800 hr at 1315°C in air, (2) up to 10 hr at 870 and 1315°C after ballistic impacting at 170 ft/sec at room temperature or at 870°C, (3) during 22 slow thermal cycles from 450 to 1260°C, and (4) in oxidation–erosion rig tests at Mach 0.85 at 1315°C for over 200 1-hr cycles (room temperature to 1315°C) in JP-5 fuel and air. Bend and tensile tests on samples before and after exposures of 800 hr at 1315°C revealed that the 0.030-in.-thick substrates had considerable room-temperature ductility (1-T 90° bend or 10 to 20% elongation).

Coatings were applied by slurry spraying the metallic elements and hydrides, vacuum sintering, and then siliciding by pack cementation. Maintaining the oxygen content of the modifier under 0.2 wt.% by using vanadium and titanium hydrides was advantageous; maintaining the combined titanium plus vanadium near 30% in the slip produced a well-bonded and sintered coating. The coating was sintered at above 1315°C to remove a significant portion of those elements through vaporization; however, retention of some vanadium was needed to prevent 870°C failure. The addition of small amounts of iron, nickel, or palladium to promote activated sintering did not give satisfactory coatings for a sintering temperature of 1205°C. Coating uniformity was adequate for elemental powder sizes under 3 μ, whereas prealloyed powder size could be as large as 12 μ. Dip coatings provided less protection than spray coatings but offered potential for further development.

Nb–Ti Alloys

The oxidation behavior of silicided Nb–Ti alloys has been studied by United Aircraft Corp.[13] Titanium-modified niobium disilicide coatings, prepared by pack-siliciding niobium, Nb–5 Ti, Nb–10 Ti, and Nb–15 Ti, were evaluated in air or argon atmospheres between 800 and 1200°C. The oxidation resistance of the coatings increased as the titanium content of the substrate increased (as shown in Fig. VII-1). Oxidation resistance was related to the composition of the oxide formed on the coating and to thermal-crack formation. The titanium-modified disilicides were less diffusionally stable than $NbSi_2$. Above 1000°C, a titanium-rich ternary MSi phase formed in substantial amounts both as a dispersion within the MSi_2 phase and as a discrete layer between MSi_2 and M_5Si_3 layers in the

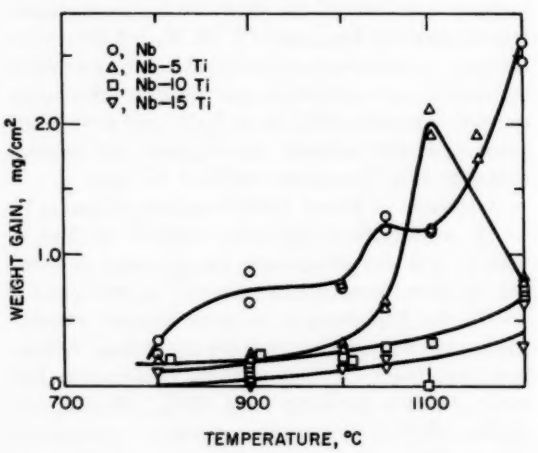

Fig. VII-1 Weight gain in 10 hr for silicided Nb–Ti alloys in air.[13]

coating. The MSi phase was less oxidation resistant than MSi_2 and presented a potential failure mechanism above 1200°C.

Hafnium-Base Alloys

The investigation of the oxidation behavior and tensile properties of hafnium-base alloys containing tantalum plus other minor additions has continued at IIT Research Institute.[14] The intended use for such alloys lies in structural components or claddings for other refractory metals. Cyclic oxidation tests were conducted on the three most oxidation-resistant alloys developed in previous programs. The alloys are Hf–24.5 Ta–1.5 Cr–0.66 B, Hf–24.5 Ta–1.2 Cr–0.66 B–0.12 Al, and Hf–23.5 Ta–1.8 Cr–1.1 Si. Weight-gain curves for all three alloys followed similar patterns. They increased linearly with time at constant temperature in the range 650 to 980°C and parabolically in the range 1090 to 1480°C. Scale-growth behavior of the three alloys was also similar, measured thicknesses being on the order of 8 mils after 100 hr at 1200°C and 15 mils after 100 hr at 1370°C.

The change from linear to parabolic oxidation was the result of precipitation of the alpha-hafnium phase from the beta matrix caused by oxygen, followed by preferential oxidation of the alpha-rich areas. The resulting subscale provided a buffer to stresses caused by expansion mismatch of the surface oxide and substrate. Since the length of thermal cycle used (2 and 12 hr) gave essentially the same results, oxidation life apparently was not affected by cycling through the temperature range of linear oxidation. Preoxidation for 10 to 20 hr at 1370°C permitted exposure of the alloys, generally up to 100 hr at 650 to 980°C, with almost no measurable weight gain. The solidus of the three alloys ranged between 1650 and 1705°C compared with 2150°C for the Hf–25 Ta binary alloy.

Extrapolation of IIT Research Institute test results indicated that an expected life for a 20-mil-thick cladding would be about 1000, 300, and 100 hr at 1200, 1370, and 1480°C, respectively. A composite consisting of Ta–10 W cladding with 20 mils of Hf–24.5 Ta–1.2 Cr–0.66 B–0.12 Al survived 300 hr at 1370°C. The projected life thus was essentially realized in the composite, although visible cracks were present in a welded-seam closure of the cladding after 20 hr of exposure.

Mo–0.5 Ti Alloy

According to a British investigation,[15] boron-modified silicide coatings were more protective on Mo–0.5 Ti alloy than the unmodified silicide, particularly under cyclic conditions. Silicon and boron were deposited on alloy specimens, respectively, from gaseous $SiCl_2$ and BF. The weight of boron deposited was nominally 10% of the silicon deposited. Isothermal air-oxidation resistance of the unmodified silicide 2 mils thick was nominally 700 hr at 1200°C. The resistance in 20-min cycles from room temperature to 1200°C was 30 to 150 cycles. In comparison, the isothermal life of the boron-modified silicide was 4 times longer and the cyclic life was 50 times greater. On the basis of cyclic oxidation and past oxidation tests in a simulated engine-exhaust environment, the modified coating had a lower life at 1100°C maximum temperature than at 1200°C. Specimens that failed in 1100°C tests showed that oxidation occurred through microcracks and pinholes in the coating. Specimens in 1200°C tests failed by diffusion consumption, resulting from the formation of the less oxidation-resistant Mo_5Si_3 phase. On the basis of metallography, electron probe, and X-ray analysis, the beneficial effect of boron appears associated with the formation at 1200°C of a thermally stable cristobalite phase containing small amounts of boron and molybdenum. Miniature Charpy impact tests indicated that coated unnotched specimens behaved similarly to notched uncoated specimens by exhibiting brittle behavior up to 200°C.

Seminar Proceedings

The results of worldwide research in the general field of coatings for high-temperature metals have been published as a result of the Sixth Plansee Seminar held in June 1968 in Reutte/Tyrol, Austria.[3]

REFERENCES

1. J. Stringer, The Oxidation of Niobium Single Crystals, *Acta Met.*, 17: 1227-1246 (1969).
2. F. W. Vahldiek, Hafnium II. Oxidation, *J. Less-Common Metals*, 19: 305-314 (1969).
3. *High Temperature Materials*, Sixth Plansee Seminar, June 24–28, 1968, Reutte/Tyrol, Austria, F. Benesovsky (Ed.), Metallwerk Plansee AG, Reutte/Tyrol, Austria or Springer-Verlag, New York, 1969 (CONF-680603).
   a. P. Kofstad and I. Kvernes, Studies of High Temperature Oxidation of Hafnium–Niobium Alloys, pp. 291-316.
   b. D. S. Evans, Oxidation Characteristics of Tungsten–Chromium–Palladium Alloys, pp. 42-56.
4. C. A. Steidel and D. Gerstenberg, Thermal Oxidation of Sputtered Tantalum Thin Film Between 1000 and 525°C, *J. Appl. Phys.*, 40: 3828-3835 (1969).
5. R. E. Grace and R. F. Kassner, Transition Kinetics During Linear to Parabolic Oxidation of Chromium, *Acta Met.*, 18: 247-251 (1969).

6. V. N. Ageev and N. I. Ionov, Interaction Between Oxygen and Tungsten (in Russian), *Zh. Tekh. Fiz.*, 28: 1149-1156 (July 1968).
7. J. C. Polk, Field Ion-Emission Studies of the Initial Stages of Tungsten Oxidation, Thesis, Illinois Institute of Technology, 1968.
8. J. D. McKinley, Jr., Mass Spectrometric Investigation of the Surface Reaction of Tungsten with Chlorine–Oxygen Mixtures, in *Reactivity of Solids,* Symposium Proceedings, Schenectady, N. Y., Aug. 25–30, 1968, pp. 345-351, J. W. Mitchell, R. C. DeVries, R. W. Roberts, and P. Cannon (Eds.), Wiley-Interscience, A Division of John Wiley & Sons, 1969 (CONF-680833).
9. V. F. Rybalko, V. Y. Kolot, and Y. M. Fogel, Effect of Oxygen Pressure on the Oxidation Process of Tungsten, *Sov. Phys.–Solid State (English Transl.),* 11: 1142-1143 (November 1969).
10. J. C. Batty and R. E. Stickney, Quasi-Equilibrium Treatment of Gas–Solid Reactions. II. Flash Desorption of Oxidation Products from a Tungsten Surface, *J. Chem. Phys.*, 51: 4485-4492 (November 1969).
11. *Transactions of the International Vacuum Metallurgy Conference,* Conference Proceedings, Beverly Hills, Calif., June 10–13, 1968, R. B. Barrow and A. Simkovich (Eds.), American Vacuum Society, New York, 1968 (CONF-680623).
    a. R. F. Bunshah, Contamination of Reactive Metals in Vacuum Heat-Treating at Various Vacuum Levels, pp. 611-619.
    b. R. W. Harrison and E. E. Hoffman, Contamination of Tantalum and Tantalum Alloys in Low-Pressure Oxygen Environments, pp. 29-57.
12. H. E. Shoemaker and A. R. Stetson, Silicide Coatings for Tantalum and Columbium Alloys, Report NASA-CR-72519, Solar Division, International Harvester Company, August 1969.
13. E. J. Felten, Oxidation Behavior of Silicided Columbium–Titanium Binary Alloys, *Electrochem. Technol.*, 6: 438-447 (1968).
14. V. L. Hill, Development of Oxidation-Resistant Hafnium Alloys, Report IITRI-B-6090-4, IIT Research Institute, September 1969.
15. C. Hayman and J. E. Restall, Improved Silicide Coatings for the Protection of Molybdenum–0.5% Titanium Alloy, *J. Less-Common Metals,* 19: 9-21 (September 1969).

Section VIII

Reactor Materials

Corrosion by Liquid Metals and Fused Salts

By E. M. Simons

CORROSION BY SODIUM

Corrosion of Stainless Steels by Sodium

At Brookhaven[1] an attempt was made to define the corrosion mechanism of stainless steels by studying the corrosion and interaction of pure Co, Fe, Ni, and Cr in sodium. A continuous string of polished specimens arranged in repeated groups of four in the order listed was exposed for 1000 hr to 660 to 760°C sodium in the hot leg of a 316 stainless-steel thermal-convection loop (~3 cm/sec sodium velocity). The diffusion-type cold trap was maintained at 110, 200, or 400°C, giving measured oxygen levels in the sodium of 4, 10, or 110 ppM, respectively. The following observations resulted:

1. All specimens were etched by grain-boundary attack except for the chromium specimens exposed to 110-ppM-oxygen sodium. These showed a dark gray surface film.

2. Nickel specimens lost weight (up to 2 mg/cm^2), whereas iron and cobalt specimens gained weight (up to 0.8 mg/cm^2). Chromium specimens showed little or no weight change.

3. All four elements migrated. As the oxygen content of the sodium was increased from 4 to 110 ppM, deposition of iron increased sharply, deposition of nickel did not change, deposition of chromium increased slightly, and only traces of cobalt deposition were found.

To explore the limits of performance at potential hot-spot conditions in an LMFBR, workers at General Electric[2] extended their previous 650°C maximum-temperature loop studies to 705°C. Corrosion specimens of 304 and 316 stainless steels were exposed for periods up to 3000 hr to sodium containing <10 ppM oxygen and flowing at up to 30 ft/sec with a cold-leg temperature of 425°C. The researchers summarized their findings as follows:

1. Corrosion rates at sodium velocities less than ~15 ft/sec are approximately linearly dependent on velocity. Increasing sodium velocity in the 15 to 30 ft/sec range produces a progressively smaller increase in corrosion until 30 ft/sec, above which corrosion appears independent of velocity.

2. Corrosion rates measured at a single velocity but at successive positions downstream (with resultant increasing saturation of the sodium with corrosion products) were found to decrease by 50 to 75%.

3. Changing sodium mass flow in the range 0.5 to 1.0 gal/min at the same sodium velocity (~3 ft/sec with Reynolds' number <10,000) produced <10% increase in corrosion rate.

4. Significant reductions in chromium, nickel, and manganese were observed on surfaces of corrosion samples. The relative amount of loss for each was dependent on exposure conditions. In separate experiments that differed in sodium velocity and, therefore, in total corrosion, the pattern of movement of chromium and nickel was different but manganese stayed the same. Nickel movement was more sensitive to velocity than chromium, showing a greater loss at higher sodium velocities.

5. An experiment comparing corrosion of pure iron surfaces to corrosion of 316 stainless-steel surfaces in a loop hot leg showed that alloy composition played a significant role in the corrosion process. The iron surfaces gained weight and approached a composition near that of the stainless-steel surfaces.

6. Turbulence and activity of alloy constituents in sodium solution played the dominant role in cold-leg deposition. An increase of sodium velocity from 5 to 10 ft/sec resulted in 85% increase in rate of deposition of corrosion products.

7. Various carbides ($M_{23}C_6$,M_7C_3) and $NaCrO_2$ have been identified in the deposits from the cold leg.

8. Nucleation of particulates in the sodium stream upon cooling and subsequent deposition on cold-leg surfaces are believed to be a more likely process than diffusion of elemental species to surfaces followed by nucleation.

9. Contrary to equilibrium considerations, carbon transport was observed from high- to lower-temperature regions. A correlation was found in two separate

test runs between movements of carbon and chromium. Carbon loss as high as 79% was measured for 316 stainless steel at 1300°F (705°C).

10. Microstructural changes were observed in all alloys and appeared to be dependent upon corrosion rate and alloy composition. Three general changes were seen: (1) ferritic surface phase, (2) a zone adjacent to the surface and depleted in carbon, and (3) localized and enhanced elemental leaching at grain boundaries.

11. Carbon movement had a profound effect on microstructural changes, by reducing the normal carbide precipitation and enhancing formation of intermetallic phases. Continued development of these changes implies major effects on long-term creep and rupture properties.

Hopenfeld at Atomics International[3] conducted loop experiments in which high-purity 650°C sodium was saturated with corrosion products at the inlet to the 316 stainless-steel test section, and the test-section surface was subjected to a constant heat flux of $\sim 10^6$ Btu/(hr)(ft^2) by internal heating to produce a 30°C temperature rise along its 3.5-in. length. The objective was to note the effects of velocity (10 and 20 ft/sec) and temperature on corrosion without introducing extraneous system-dependent effects. From the observed velocity effects, it was concluded that the corrosion rate is controlled by liquid diffusion.

Using the difference between the concentration of dissolved metal in sodium next to the surface and of the dissolved metal in the bulk of the liquid as the driving force for metal dissolution, Hopenfeld derived expressions for the maximum corrosion rates at various locations along the test section and compared them with the measured rates. Reasonable agreement was obtained when he used the lowest published solubility data of iron in sodium, indicating that the theory may be useful for predicting the maximum corrosion rate of cladding under reactor operating conditions.

Effects of Sodium on Mechanical Properties of Component Materials

Other investigators at Atomics International[4] conducted loop tests to evaluate the effects of steady and cyclic heat fluxes [0.8 and 10 x 10^6 Btu/(hr)(ft^2)] on creep behavior of 304 and 316 stainless-steel tubes immersed in high-purity 650°C sodium flowing at 20 ft/sec. Mass transfer was observed under steady internal heating for up to 600 hr, but there was no difference in creep behavior from that of tubes stress-rupture tested in static sodium. Cyclic heating reduced the rupture life by a factor of 2 and produced large changes in microstructure, strain profile, and strain at failure. These effects were relatively insensitive to the magnitude of the cyclic heat flux. However, an increase in frequency reduced the life of both annealed and cold-worked 304 stainless steel and had the opposite effect on cold-worked 316 stainless steel.

The analysis indicates that repeated thermal-stress relaxation, as a result of heat-flux cycling, produces an increment of plastic strain for each cycle, superimposed on conventional biaxial creep due to pressure. Although this study is inadequate to establish design criteria for cyclic action, it does point to danger in designing fuel sheaths on the basis of steady-state behavior. The numerous reactor transients that will be experienced during service could be sufficient to produce end-of-life ductility limits of irradiated cladding.

Mine Safety conducted an extended study on the effects of sodium and helium on design properties of 304 and 316 stainless steels to see whether the ASTM allowable-code values for stainless steels in air could be extended to cover the design of an LMFBR system. Test conditions included stress-free exposures to high-oxygen sodium, high-carbon sodium, clean sodium, and helium at 1200 and 1400°F (650 and 760°C); tensile tests in air at 1200 and 1400°F; and creep-rupture tests at 1200°F in flowing (20 ft/sec) clean sodium for times up to 4000 hr. The summary report[5] concluded that, on the basis of the tensile data and extrapolated creep data, 304 stainless-steel code values could be applied to an LMFBR design with allowances being made for the anticipated losses in ductility. For 316 stainless steel, however, some reduction in code values would be warranted, with attention still given to the ductility losses noted.

It was recommended that, for both steels, long-term (>10,000 hr) creep data be obtained to determine the true longer-term creep behavior instead of relying on extrapolation of 4000-hr data. The 316 stainless steel appeared stronger than the 304 in most cases during short-time testing. However, when the data were extrapolated, the strength differences were less apparent. In fact, in some cases, the 304 alloy appeared stronger. Of course, the fact that the results are based on single heats of material and long extrapolations suggests that they should not be considered final.

On the basis of measurements of the room-temperature and 650°C mechanical properties of a single heat of 316 stainless steel during exposure to air, helium, and low-oxygen sodium, Kirschler and Andrews[6] observed the following:

Test	Environment		
	Air	Helium	Sodium
Cyclic strain	Fewest cycles to failure	Most cycles to failure	Intermediate
Stress rupture	No significant difference in rupture strength; ductility perhaps better in sodium		
Creep	Lowest rate	Highest rate	Intermediate
Tensile strength	Small differences (<6%)		

When the quantitative data from these tests were compared with ASM Metals Handbook data from several heats of 316 stainless steel tested in air, it was noted that the variations in properties due to environmental differences were substantially less than the variations due to differences from heat to heat of the steel. This is apparent from the following tabulation:

Source	MSAR	ASM data
Heats of 316 stainless steel	1	13
Exposure environments	Air, He, Na	Air
Temperature	650°C	650°C
Ultimate tensile strength, ksi	48–51	42–64
0.2% offset yield strength, ksi	26–27	12–39
Elongation, %	44–48	23–63

One approach to the design of sodium systems for extended service is to make "corrosion allowances" in the dimensions of the components or in the design stresses. The magnitudes of these allowances are estimated from laboratory corrosion tests in which the influences of various simulated-service environmental factors on corrosion rates and mechanical properties have been measured. Corrosion effects include uniform surface removal as functions of distance downstream from heater, sodium velocity, oxygen level, and temperature; mass transfer, including selective leaching of surface constituents, carburization, and decarburization; and intergranular attack. Using published corrosion and mass-transfer test results from the United Kingdom and Mine Safety, workers at United Nuclear[7] estimated allowances for surface removal (mils/year) and recommended multiplication factors to be applied to ASME mechanical-property data for 304 and 316 stainless steels and for 2.25 Cr–1 Mo steel as LMFBR piping materials.

A similar study at General Electric[8] was directed toward materials for sodium-system components, such as fuel cladding and heat exchangers. Materials considered were austenitic stainless steels, Nickel 200, Nimonic 80A, Inconel 600, and hard-facing alloys. Corrosion allowances for the nickel-base alloys were up to 3.4 times those for the stainless steels. In view of the considerable extrapolation and guesswork required to establish the allowances, General Electric recommended extensive further studies to increase the degree of confidence not only in the data but also in the scale-up from laboratory loops to large reactor systems.

Workers at General Electric[9] studied the application of Section VIII of the *ASME Boiler and Pressure Vessel Code* to the determination of allowable design stresses for low-alloy steels in bimetallic sodium systems. The decarburization that occurs during operation of such systems, coupled with the corrosion and creep, leads to progressively lower material strength and higher stresses. The initial design features of a model system were determined for three different cases under conditions at which the strain rate was the controlling parameter. The rate of decarburization to the equilibrium level influences the results. Since this is controlled by geometry and fluid dynamics, presence of other alloys, temperature profile, sodium chemistry, and other factors, calculations were made for both rapid and slow decarburization.

Table VIII-1 shows the results for each case. The initial design stress for an expected lifetime of 100,000 hr depends on the case and ranges from 69 to 78% of the code-allowable stress. Note that the thin wall in case I leads to end-of-life strains and strain rates that would probably exceed the capabilities of the alloy. Case II leads to end-of-life strain rates that are higher than the code-allowable value of 0.01%/1000 hr. The use of total accumulated strain as the controlling criterion (case III), although requiring the greatest wall thickness, appears to be the most practical choice.

Effects of Sodium on EBR-II Materials

Workers at Argonne[10] conducted metallographic examinations of a large number of samples of the 304L stainless-steel cladding from spent EBR-II fuel elements to determine the effects of the 370 to 595°C reactor primary sodium and sodium-removal operations on the microstructure of cladding and encapsulation materials. The usual procedure for removal of residual sodium from the surfaces prior to exposing a subassembly to air for examination is by conversion of the sodium to sodium oxide and sodium hydroxide with humidified

Table VIII-1 Summary of Design Features and Operating Behavior of Low-Alloy Steel for Different Interpretations of ASME Code[9]

Model System

Temperature = 900°F (482°C)
Pressure = 1800 psi (1.27 kg/mm^2)
Initial OD of tubing = 1.50 in. (38.1 mm)
Expected lifetime = 100,000 hr
Corrosion rate of steel in sodium = 0.003 in. (0.076 mm)/100,000 hr

ASME Code interpretation	Initial wall thickness, in. (mm)	Initial design stress, psi (kg/mm^2)	End of life: Estimated operating stress, psi (kg/mm^2)	End of life: Total strain, %	End of life: Strain rate, %/1000 hr
Slower rate of decarburization					
Case I*	0.106 (2.69)	13,100 (9.21)	15,994 (11.24)	10.3	0.33
Case II†	0.133 (3.38)	10,150 (7.14)	10,596 (7.45)	1.0	0.032
Case III‡	0.149 (3.78)	9,060 (6.37)	9,303 (6.54)	0.3	0.01
More rapid rate of decarburization					
Case I*	0.106 (2.69)	13,100 (9.21)	19,081 (13.41)	20.3	0.33
Case II†	0.142 (3.61)	9,507 (6.68)	9,910 (6.96)	1.0	0.0175
Case III‡	0.149 (3.78)	9,060 (6.37)	9,368 (6.58)	0.65	0.01

*Initial strain rate at startup = 0.01%/1000 hr.
†Total creep strain after 100,000 hr = 1%.
‡Strain rate at end of life = 0.01%/1000 hr.

argon and air. Subsequently the oxidized sodium is removed by flowing water through the subassembly.

The examinations revealed no changes that could be attributed to either the reactor sodium or the sodium-removal operation. The sensitization (carbide precipitation at the grain boundaries) observed was attributed to the heat-treatment of the cladding during reactor operation, and its extent was governed by the original carbon content of the steel.

Eight subassemblies containing 15 alloys used in the primary system of EBR-II and shield graphite canned in 304 stainless steel are being irradiated in the EBR-II core at 700°F (370°C) for varying periods of time and neutron dosages.[11] Most of the alloy specimens are exposed directly to reactor sodium, and the remainder are sealed in helium. The alloys include aluminum bronze; Stellite 6B; Inconel X-750; T-1 tool steel; beryllium copper; 304, 347, 416, and 420 stainless steels (the 304 in four variations); 17-4PH stainless steel; and tantalum.

The first subassembly (SURV-I) has been removed and examined after 671 days in the reactor and an estimated average fluence of 3×10^{19} neutrons/cm^2 at energy levels >0.82 MeV. Of the materials exposed, only the beryllium copper and tantalum experienced appreciable weight loss and thus appear to be unsuitable for use in contact with sodium under the conditions of the test. The 340 and 347 stainless steels and the graphite assemblies experienced no significant changes in mechanical or physical properties. Preliminary examinations of specimens from SURV-II, which have also been removed, likewise showed no significant deleterious effects of exposure on the stainless steels and graphite.[12-15] The other materials experienced appreciable changes in mechanical properties and/or metallurgical structure, but, in the absence of thermal-effects control samples, the relative importance of the effects of neutron dosage and long exposures at reasonably elevated temperature cannot be established conclusively for these materials.

Fusible seals of eutectic Bi–Sn alloy (58 wt.% bismuth) are used in the EBR-II rotating shield plugs. Because the seal is exposed to sodium vapor, solids resulting from the reaction of the sodium with the alloy eventually precipitate out and cause problems. Argonne[16] found that the solubility of sodium in the Bi–Sn eutectic is 0.35 wt.% at 177°C (the seal operating temperature). The addition of 1 wt.% indium to the eutectic increases this to 0.50 wt.%. It takes about 4 months of EBR-II operation to reach the saturation concentration in eutectic Bi–Sn and 6 months in the indium-doped alloy. It was suggested that about

two-thirds of the seal alloy be drained periodically and replaced with new alloy to reduce the sodium concentration when precipitation begins. Two such consecutive dilutions could reduce the concentration to about 0.16 wt.% sodium and minimize the precipitation of solids. A blanket of silicone oil on the seal surface was recommended to slow down the dross formation. No corrosion of the 304 stainless-steel seal trough by the Bi–Sn–In or Bi–Sn alloy is anticipated, on the basis of a 15,000-hr static test at 177°C.

Corrosion of Vanadium Alloys by Sodium

As part of a program to study interstitial mass transport between stainless steel and vanadium, workers at Oak Ridge[17] are exposing 40-mil sheet vanadium tensile specimens for 500 hr to 700 and 800°C low-oxygen sodium in stainless-steel containers. Two grades of vanadium—commercial and high purity—were tested. The high-purity material increased in oxygen, carbon, and nitrogen, whereas the commercial material gained only carbon and nitrogen. The transport of carbon and nitrogen from 304L stainless steel to the vanadium was substantially greater at 800°C than at 700°C. Interstitial transport from titanium-stabilized 321 stainless steel was negligible at 700°C, compared with that from 304L stainless steel. Room-temperature tensile ductilities of both grades of vanadium were reduced by the sodium exposures in 304L stainless-steel containers. In contrast, testing in 321 stainless steel produced no measurable change in either strength or ductility compared with the properties of the control specimens after exposure to 700°C argon for 500 hr.

In similar studies at Westinghouse[18] with vanadium-alloy inserts in pumped low-oxygen sodium loops made of 316 stainless-steel tubing and operating between 675 and 800°C, the inserts gained weight as a result of major increases in nitrogen, carbon, and oxygen, particularly near the exposed surfaces. For example, after 1500 hr in 785°C sodium containing <10 ppM oxygen and flowing at 5 ft/sec, the 0.5-mil surface layer of a Vanstar-9 sample (V–6.4 Fe–5.3 Nb–1.3 Zr–0.06 C) showed the following increases in interstitial content: nitrogen went from 80 to 21,000 ppM; carbon went from 600 to 5500 ppM; and oxygen went from 550 to over 6000 ppM. The 316 stainless-steel containment tubing, on the other hand, showed severe depletion of both nitrogen and carbon at the sodium-exposed surface and nitrogen enrichment at the air-exposed surface. Using available interstitial diffusion data, the researchers calculated the theoretical weight loss of interstitials in the stainless steel under test-loop conditions and got excellent agreement with the measured weight gain in the vanadium alloy. This provides a method of predicting the effects of material and surface-area changes on the behavior of vanadium alloys in sodium.

Argonne workers[19] exposed vanadium and selected higher-strength vanadium-base alloys to sodium cold trapped at two temperatures (~110 and 175°C, corresponding to ~6 and 13 ppM oxygen, respectively). Both static (oxygen-refreshed autoclave) and dynamic (pumped loop) exposures were made at temperatures from 450 to 700°C. Linear rates of weight loss with time were noted at the higher oxygen level, whereas much lower weight and dimensional changes were observed at the lower oxygen level. Typical curves are shown in Fig. VIII-1. Unlike the Oak Ridge and Westinghouse results, pickup of interstitials by the vanadium alloys was modest, especially for nitrogen and carbon. Oxygen was the major impurity transferred to the specimens. Titanium as an alloying element caused increased impurity pickup and concentrated the impurities in a subsurface band 10 to

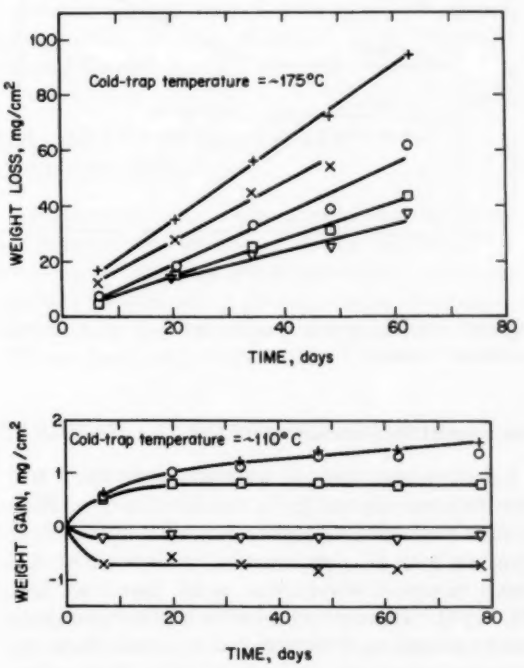

Fig. VIII-1 Corrosion of vanadium alloys by cold-trapped sodium in static oxygen-refreshed autoclaves.[19] x, V; +, V–20 Ti; ▽, V–10 Cr; ○, V–15 Ti–7.5 Cr; □ V–15 Cr–5 Ti.

100 μ thick. The V–Cr binary alloy was the most corrosion resistant and appears to offer promise as a fuel cladding.

Comparison of static and dynamic (6.1 m/sec velocity) corrosion rates for oxygen levels of 15 to 20 ppM in the sodium at 650°C showed that an increase in velocity resulted in an acceleration of the corrosion process for the V–20 Ti alloy. However, the corrosion rate was much more sensitive to cold-trap temperature than to sodium velocity. Thus very low-oxygen sodium may attack vanadium alloys quite slowly, regardless of flow velocity. At Argonne, velocity effects are being looked at separately.[20] A disk of vanadium was rotated at different speeds in 600°C sodium containing 16 ppM oxygen. Periodic weighings of the disk showed that at any given rotational speed the rate of weight loss was constant, increasing as the square root of the speed above about 50 rpm (Fig. VIII-2). This type of dependency suggests that the dissolution is a liquid-diffusion-controlled process.

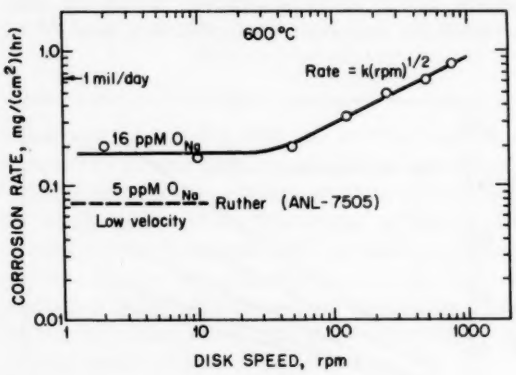

Fig. VIII-2 Effect of disk speed on linear corrosion rate of vanadium in sodium.[20]

Inertness of Molybdenum to Sodium

A molybdenum-clad, tantalum, control-rod test specimen was exposed by General Electric[21] to 550°C sodium containing <10 ppM oxygen for 1000 hr in a dynamic loop (3 m/sec velocity) to demonstrate the noble nature of molybdenum under Fast Flux Test Facility (FFTF) conditions before in-pile experiments were undertaken. Following the exposure, visual appearance, gas-pressure leak check, X-ray check, ultrasonic check, weight check, and dimensional check all indicated that the specimen had undergone absolutely no change.

CORROSION IN RANKINE-CYCLE SPACE POWER SYSTEMS

Lithium–Potassium Systems

A popular concept for nuclear spacecraft propulsion involves an electric generator driven by a potassium-vapor turbine. The potassium is vaporized in a boiler by heat from reactor-heated lithium. The Jet Propulsion Laboratory[22] constructed and tested a two-loop Li–K facility to simulate the major elements of this system. All material that came in contact with fluids above 815°C was Nb–1 Zr, with the exception of tungsten valve facings, hot-trap getters, and the TZM (Mo–0.5 Ti–0.08 Zr–0.02 C) turbine wheel.

Initial operation of the system for about 1000 hr at lithium temperatures up to 1150°C with a 10% bypass yttrium hot trap in the lithium loop and 2200 ppM nitrogen and 700 ppM oxygen in the lithium produced only minor grain-boundary notching of the Nb–1 Zr tubing. No evidence of mass transfer of the yttrium was encountered, despite thinning of the yttrium plates in the hot trap and analyses indicating 5 wt.% yttrium in the lithium. Subsequent operation of the system at similar temperatures and times without hot trapping resulted in extensive mass transfer of niobium throughout the system and extensive contamination and corrosion of the Nb–1 Zr tubing.

Operation of the potassium loop both with and later without a full-flow zirconium hot trap produced little change in the interstitial content of the system tubing. Corrosion after both modes of operation was minimal. Vapor quality had a marked effect on erosion of the tubing. Low-quality vapor (50 to 80%) eroded the outside radii of the tubing and the throat of the turbine nozzle. Higher-quality vapor had no observable erosive effect, even when run longer and at higher temperatures.

A comprehensive review of the compatibility of structural materials with molten lithium is included in a Lawrence Radiation Laboratory treatise[23] on lithium as a nuclear reactor coolant. It covers virtually all recorded lithium corrosion research using static and dynamic systems, with base metals, refractory metals, ceramics, and cermets. There are special sections on the effects of lithium on mechanical properties of refractory alloys, the resistance of materials to erosion and wear in lithium, and the solubility of containment metals in lithium.

Advanced tantalum alloys for Rankine-cycle space-power systems are being tested by General Electric[24]

for resistance to attack by 1030 to 1315°C lithium in thermal-convection capsules. Specimens of T-111 (Ta–8 W–2 Hf), ASTAR 811C (Ta–8 W–1 Re–0.7 Hf–0.03 C), and ASTAR 811CN (Ta–8 W–1 Re–1 Hf–0.015 C–0.01 N) were exposed for 5000 hr and then bend tested and analyzed chemically and metallographically. Included were some specimens that had been purposely contaminated with oxygen in both the welded and unwelded conditions.

In almost every case, the posttest oxygen content dropped to below 10 ppM (from as much as 387 ppM in oxygen-contaminated T-111, 248 ppM in oxygen-contaminated 811C, and 59 ppM in noncontaminated 811C). The greatest corrosive attack was observed in welded, oxygen-contaminated 811C specimens that had been exposed as welded. Apparently excess oxygen was free to combine with the lithium to produce platelet-type (intragranular) attack up to 15 mils deep, as well as intergranular attack throughout. Similar specimens given a 1315°C heat-treatment for 1 hr to combine all the oxygen with hafnium prior to lithium exposure were not attacked. On the basis of Nb–1 Zr technology, if there is more oxygen in the alloy than the amount needed to oxidize all the getter (hafnium, in the case of these tantalum alloys) present, these alloys would be attacked by lithium regardless of heat-treatment.

Mass transfer of interstitials (carbon, nitrogen, and oxygen) from the hottest portion of the capsule walls to the cooler end was observed. A loss in stress-rupture life of the exposed 811CN specimens tested at 20 ksi and 1315°C was attributed to heat-treatment effects rather than corrosive attack by the lithium.

The observed drastic increase in the apparent solubility of niobium in 600°C potassium as a result of increasing the oxygen content of the potassium is commonly attributed to the formation of potassium niobates. As an alternative explanation, Klueh[25] analyzed the case where no ternary oxides exist at equilibrium and the higher solubility stems from a reduction in the activity of the niobium by virtue of interactions between the two solutes (oxygen and niobium) in the melt. By applying Wagnerian interaction parameters, he was able to obtain order-of-magnitude agreement with measured oxygen distribution coefficients. Also, by use of the phase rule at equilibrium at 600°C, he showed that there would be no partitioning of added oxygen if a third condensed phase (ternary oxide) were present. Since partitioning definitely occurs, then the presence of the ternary oxide is ruled out.

Mercury Systems

Extensive testing of 9 Cr–1 Mo steel for the tubes of a NaK-heated mercury boiler for the SNAP-8 Rankine-cycle power-conversion system revealed that this material was not sufficiently resistant to mercury corrosion at 595°C. In view of the very low solubility of tantalum in mercury, workers at Aerojet-General[26] studied the feasibility of substituting tantalum for the 9 Cr–1 Mo steel. The results of a fabrication and corrosion-test program indicated considerable promise for bimetallic tubes consisting of a tantalum liner bonded by hot coextrusion to the ID surface of a 316 stainless-steel tube. An alternative tube configuration, which also appears acceptable for a 40,000-hr operating life, consists of a circular tantalum tube inside an oval-section tantalum tube with stagnant NaK between them and a circular 321 stainless-steel tube around the outer one. Mercury flows in the inner tube, and NaK flows in the outer annulus.

In another part of the same program, it was noted that mercury-loop contamination by air of Mix 4P3E, an organic fluid used for lubrication and cooling in SNAP-8, resulted in the formation of reaction products on the tantalum tube surface that interfered with heat transfer. A six-step chemical cleaning procedure, with distilled-water flushing after each step, effectively removed the surface film.

SOLUBILITY OF MATERIALS IN LIQUID METALS

Because solubility is a basic parameter which may be important in understanding the mechanism of corrosion of materials by liquid metals, numerous solubility studies are continually being undertaken. Some results that have become available since mid-1969 are presented in Table VIII-2.

LIQUID-METAL CORROSION REVIEW

A 1968 Soviet treatise on corrosion by liquid metals is now available in English translation.[31] It begins with a review of the theories of the various kinds of corrosion by sodium (destruction of surface films, dissolution, intergranular penetration, and mass transfer). A chapter is devoted to corrosion of steels and nickel-base alloys in static isothermal systems. This is followed by a chapter on corrosion under dynamic polythermal conditions, including correlations with test results on steels, nickel-base alloys, and refractory metals. A rather extensive discussion of carbon transfer

Table VIII-2 Solubility of Various Materials in Liquid Metals

Solvent	Solute	Solubility equation	Temp. range, °K	Heat of solution, kcal/mole	Ref.
K	Mo	log (wppM Mo) = 2.21 ± 0.13 − (1472 ± 156)/T(°K)	1040–1316	6.7 ± 0.8	27
K	W	log (wppM W) = 5.02 ± 0.21 − (3851 ± 243)/T(°K)	1055–1328	17.6 ± 1.2	27
Pb–55.5 Bi	Cu	log (wppM Cu) = 6.41 − 1920/T(°K)	673–823	8.78 ± 0.27	28
Pb–55.5 Bi	Co	log (wppM Co) = 5.30 − 2834/T(°K)	673–823	12.97 ± 0.50	28
Pb–55.5 Bi	Ni	log (wppM Ni) = 5.70 − 1000/T(°K)	753–823	4.57 ± 0.53	28
Pb–55.5 Bi	Cr	log (wppM Cr) = 3.98 − 2280/T(°K)	673–823	10.43 ± 2.28	28
Na	Cu	log (wppM Cu) = 5.6362 − 3199.5/T(°K)	595–999	14.6 ± 0.7	29
Na	Bi	log (at.% Bi) = 1.188 − 2100/T(°K)	398–563	9.6	30
Na	Bi	log (at.% Bi) = 4.900 − 4178/T(°K)	563–923	19.1	30
Na	Mo	<2 wppM Mo (insufficient analytical sensitivity)	973–1278		30
Na	Ti	1 to 16 wppM (no regular temperature dependence)	873–1173		30
Na	Cr	~1 to 200 wppM (large scatter)	873–1273		30

in sodium systems ensues, with Nevzorov's conclusion that carbon migrates as CO, which forms as a result of interaction of dissolved oxygen ions in the sodium with carbon ions in the steel. The final chapter reviews various physicochemical mechanisms of corrosion and carbon transfer in sodium and other liquid metals, with emphasis on the importance of the ionic nature of nonmetallic impurities in the melts. This book represents a good summary of Soviet corrosion research over the past decade, and the author's approach to the general theory of corrosion by liquid metals is noteworthy.

CONTAINMENT OF MOLTEN URANIUM FUELS

Experiments at NASA–Lewis[32] demonstrated that single-crystal tungsten and possibly a polycrystalline W–Hf alloy can contain molten uranium for relatively long times under isothermal conditions up to 1500°C without excessive attack. However, several problems would have to be overcome before these materials could be used as containers in a molten-uranium-fueled reactor.

In the capsule tests the excellent wetting of the tungsten by the uranium caused the uranium to climb up the capsule walls and attack grain boundaries in the closure weld, ultimately penetrating through the weld. Indeed, polycrystalline tungsten specimens inside the single-crystal capsules exhibited extensive intergranular attack after only 10 hr at 1200°C. Although the addition of 1.5 wt.% of hafnium to the tungsten showed promise of reducing intergranular attack, some mass transfer of metal occurred from the capsule walls to dendrites which formed near the uranium meniscus.

Another problem is that cracks developed in all the capsules during cooling after the uranium had solidified. These apparently resulted from the difference in thermal expansion and the strong bonding between the uranium and the capsule walls. Thus, even if corrosive attack were not limiting, it appears that tungsten and the W–1.5 Hf alloy cannot be used to contain molten uranium for more than one thermal cycle.

Studies at Ames[33] showed that eutectic Pb–Bi (55.5 wt.% Bi) did not attack 2.25 Cr–1 Mo steel in an isothermal dynamic system at temperatures below 700°C. Above 700°C the molten alloy attacked the steel with increasing severity until at 900°C only long fingers of ferrite remained in place of the original metal surface. When uranium fuel, a zirconium getter, and fission-product elements (Mg, Mo, Ce, Nd, and La) were added to the eutectic Pb–Bi to simulate conditions in a liquid-metal-fueled reactor, the temperature could be raised to 800°C before corrosion was detected. Above 800°C the attack increased with temperature as before.

CORROSION BY FUSED FLUORIDE SALTS

Two decades of corrosion testing and operating experience with the Molten Salt Reactor Experiment

have demonstrated the excellent compatibility of Hastelloy N and graphite with fluoride salts containing LiF, BeF_2, ThF_4, and UF_4. The fertile–fissile salt for a molten-salt breeder will contain these same fluorides, so only proof-testing will be required for the primary reactor circuit. However, several improvements are needed to ensure a 30-year plant life. These are: Hastelloy N with improved resistance to embrittlement by thermal neutrons, graphite with better dimensional stability in a fast-neutron flux, lower-permeability graphite, and a secondary coolant that is inexpensive and has a melting point around 400°C. The programs in progress to meet these needs are described in a nine-author paper from Oak Ridge.[34]

The TZM alloy (Mo–0.5 Ti–0.08 Zr–0.02 C) is a candidate container material for the reprocessing of fused-salt fuel by vacuum distillation at 1000°C. To get an indication of its suitability, Oak Ridge workers[35] exposed samples of TZM in a TZM capsule partially filled with $LiF–BeF_2–ThF_4–UF_4$ (68–20–11.7–0.3 mole %) at 1100°C for 1011 hr. Slight corrosion was observed in the form of leaching of titanium and possibly zirconium from the TZM. Submerged samples became partially recrystallized, whereas those in the salt vapors did not. The recrystallization was attributed to the removal of titanium and zirconium, which, if continued, would cause the strength of the TZM alloy to approach that of unalloyed molybdenum. On the basis of this single test, neither the light corrosion nor the slow weakening effect appears to pose a serious threat to long-term use of TZM for vacuum distillation of Molten Salt Breeder Reactor fuels.

Posttest evaluation of lithium fluoride-filled capsules fabricated from the niobium alloys Nb–1 Zr, FS-85 (Nb–28 Ta–10.5 W–0.9 Zr), and SCb-291 (Nb–10 Ta–10 W) which were cycled between 815 and 1040°C for times up to 5000 hr revealed no evidence of corrosion.[36] No significant change in microstructure, chemical analysis, or tensile strength was observed. The only significant change in properties was an increase in the ductile-to-brittle transition temperature of the FS-85. However, the capsule was severely distorted by the exposure. This was attributed to stresses resulting from the 30% change in volume of the lithium fluoride during each melting and freezing cycle. The General Electric workers concluded that the strength of the niobium-base containment alloy was a more important selection criterion than its corrosion resistance. Hence the strongest of the test alloys, FS-85, was recommended for cyclic service up to 1040°C.

REFERENCES

1. A. H. Fleitman and H. S. Isaacs, The Corrosion and Mass Transfer of Pure Iron, Nickel, Chromium, and Cobalt in 660 to 760°C Sodium, USAEC Report BNL-14230, Brookhaven National Laboratory, 1969.
2. P. Roy and M. F. Gebhardt, Corrosion and Mass Transport of Stainless Steels in Sodium Systems, USAEC Report GEAP-13548, General Electric Company, Breeder Reactor Development Operation, September 1969.
3. J. Hopenfeld, Corrosion of Type 316 Stainless Steel with Surface Heat Flux in 1200°F Flowing Sodium, USAEC Report AI-AEC-12898, Atomics International, Nov. 30, 1969.
4. J. H. Shively and M. W. Mahoney, Thermal Gradient Effects on Stress-Rupture Behavior of Thin-Walled Tubing, USAEC Report AI-AEC-12896, Atomics International, Jan. 2, 1970.
5. L. H. Kirschler, R. H. Hiltz, and R. C. Andrews, The Effects of High Temperature Sodium and Helium Environments on the Design Properties of 304 and 316 Stainless Steels, Topical Report No. 18, USAEC Report MSAR-70-38, MSA Research Corp., March 1970.
6. L. H. Kirschler and R. C. Andrews, A Limited Comparison of the Mechanical Strength of Austenitic Steel in 1200°F Sodium, Air, and Helium, *J. Basic Eng.*, **91**: 785-791 (December 1969).
7. United Nuclear Corp., Corrosion and Erosion Considerations for Sodium Piping in LMFBR Plants, Memorandum 316, USAEC Report UNC-SPLM-953, June 3, 1969.
8. G. P. Wozadlo and C. N. Spalaris, Corrosion of Stainless Steel and Deposition of Particulates in Flowing Sodium Systems. Task VI. Evaluation of Mass Transfer State-of-the-Art and Analysis of FFTF Fuel Cladding, Piping, and Closed Loop Material Degradation Rates, USAEC Report GEAP-13544, General Electric Company, Breeder Reactor Development Operation, September 1969.
9. F. A. Comprelli and J. L. Krankota, Interpretation of the ASME Code for Low-Alloy Steels in Bimetallic Sodium Systems, USAEC Report GEAP-13545, General Electric Company, Breeder Reactor Development Operation, September 1969.
10. R. V. Strain, Effects of Sodium and Sodium Removal on the Microstructure of Type 304 Stainless Steel Tubing, USAEC Report ANL/EBR-6, Argonne National Laboratory, August 1969.
11. S. Greenberg (Comp.), The EBR-II Materials-Surveillance Program. I. Program and Results of SURV-I, USAEC Report ANL-7624, Argonne National Laboratory, September 1969.
12. Argonne National Laboratory, Reactor Development Program Progress Report, September 1969, USAEC Report ANL-7618, Oct. 27, 1969.
13. Argonne National Laboratory, Reactor Development Program Progress Report, November 1969, USAEC Report ANL-7640, Dec. 31, 1969.
14. Argonne National Laboratory, Reactor Development Program Progress Report, December 1969, USAEC Report ANL-7655, Jan. 29, 1970.
15. Argonne National Laboratory, Reactor Development Program Progress Report, January 1970, USAEC Report ANL-7661, Feb. 25, 1970.

16. C. C. Crothers, Investigation of Metallurgical Problems Associated with the EBR-II Fusible Seals, USAEC Report ANL-7589, Argonne National Laboratory, September 1969.
17. P. Patriarca (Comp.) and D. J. Rucker (Ed.), Fuels and Materials Development Program Quarterly Progress Report for Period Ending September 30, 1969, USAEC Report ORNL-4480, Oak Ridge National Laboratory, February 1970.
18. G. A. Whitlow and S. L. Schrock, Interstitial Transfer in a Vanadium Alloy/Stainless-Steel Bimetallic Liquid-Metal System, *Trans. Amer. Nucl. Soc.*, **12**(2): 615-616 (November 1969).
19. W. E. Ruther, The Corrosion of Vanadium and Vanadium-Base Alloys in Sodium, USAEC Report ANL-7505, Argonne National Laboratory, May 1969.
20. Argonne National Laboratory, Reactor Development Program Progress Report, October 1969, USAEC Report ANL-7632, Nov. 25, 1969.
21. General Electric Company, AEC Fuels and Materials Development Program Progress Report No. 79, USAEC Report GEMP-1013, June 30, 1969.
22. W. M. Phillips, Some Alkali Metal Corrosion Effects in a Rankine Cycle Test Loop, Technical Report 32-1457, Jet Propulsion Laboratory, paper presented at the AIME Liquid Metals Corrosion Meeting, Philadelphia, Pa., Oct. 13, 1969.
23. J. O. Cowles and A. D. Pasternak, Lithium Properties Related to Use as a Nuclear Reactor Coolant, USAEC Report UCRL-50647, Lawrence Radiation Laboratory, University of California, Apr. 18, 1969.
24. R. W. Harrison, Advanced Refractory Alloy Corrosion Loop Program, Quarterly Progress Report 18, Report GESP-376 (NASA-CR-72620), General Electric Company, Nuclear Systems Programs, Space Division, Oct. 23, 1969.
25. R. L. Klueh, The Effect of Oxygen on the Compatibility of Niobium with Potassium, *Corrosion*, **25**(10): 416-422 (October 1969).
26. H. Derow et al., Evaluation of Tantalum for Mercury Containment in the SNAP-8 Boiler, Aerojet-General Corp., Report NASA-CR-72651 (Aerojet 3680), November 1969.
27. S. Stecura, Solubilities of Molybdenum and Tungsten in Liquid Potassium, Report NASA-TN-D-5504 (N69-40053), National Aeronautics and Space Administration, Lewis Research Center, October 1969.
28. J. R. Wilson and G. Rosenblatt, The Solubilities of Several Transition Metals in Liquid Lead–Bismuth Eutectic, Canadian Paper, Centre for Metal and Mineral Technology, Queen's University, 1970.
29. R. A. Walker and J. N. Pratt, The Solubility of Copper in Liquid Sodium, *J. Nucl. Mater.*, **32**: 340-345 (1969).
30. R. L. Eichelberger, D. C. Gehri, and R. J. Sullivan, Solubility Experiments with Bi, Mo, Ti, and Cr in Liquid Sodium, *Trans. Amer. Nucl. Soc.*, **12**(2): 614 (November 1969).
31. B. A. Nevzorov, Corrosion of Structural Materials in Sodium, USAEC Report AEC-tr-6984, 1970.
32. P. D. Takkunen, Compatibility Tests of Molten Uranium with Tungsten and Tungsten–1.5 Percent Hafnium, Report NASA-TN-D-5076, National Aeronautics and Space Administration, Lewis Research Center, March 1969.
33. R. L. Suchanek and G. Burnet, Corrosion of a Low Alloy Steel in a Simulated Liquid-Metal-Fuel Mixture, *Nucl. Met., Met. Soc. AIME*, **15**: 453-466 (1969); also USAEC Report IS-T-318, Ames Laboratory, March 1969.
34. H. E. McCoy et al., New Developments in Materials for Molten-Salt Reactors, *Nucl. Appl. Technol.*, **8**: 156-168 (February 1970).
35. J. W. Koger and A. P. Litman, Compatibility of Molybdenum-Base Alloy TZM with $LiF–BeF_2–ThF_4–UF_4$ (68–20–11.7–0.3 mole %) at 1100°C, USAEC Report ORNL-TM-2724, Oak Ridge National Laboratory, December 1969.
36. R. W. Harrison and W. H. Hendrixson, Corrosion Tests of Lithium Fluoride in Contact with Columbium Alloys, Topical Report I, The Compatibility of Columbium Base Alloys with Lithium Fluoride, Report GESP-261, General Electric Company, Nuclear Systems Programs, Space Division, Sept. 19, 1969.

Section
IX
Reactor Materials

Cladding Behavior in Loss-of-Coolant Accidents

By H. S. Rosenberg

Workers at General Electric[1] have continued the study of the failure of internally pressurized tubes under dynamic heating conditions. Specimens of 304L stainless-steel cladding material 5.1 to 6.35 cm long with a 1.27-cm inside diameter and a 0.076-cm wall thickness were heated in argon at constant internal pressure at a predetermined constant heating rate until failure (expansion) was indicated by a sharp fluctuation in sample temperature. The results of the tests are shown in Table IX-1. When compared with similar results on Zircaloy-4, these results are consistent with the higher strength of stainless steel. At a given internal pressure and heating rate, the failure temperature for 304L stainless steel is 300 to 400°C higher than that for Zircaloy-4.

Argonne[2] is studying the fragmentation of molten materials being quenched in a liquid. Drops of molten stainless steel at 1600 to 2400°C were dropped from a height of 2 ft into molten sodium, and the mean diameter of the fragments was calculated using the volume-surface mean particle size, or Sauter mean diameter. The diameter of the fragments decreased from 1.26 mm to 0.27 mm as the temperature of the molten steel was increased from 1600 to 2200°C at a constant sodium temperature of 250°C. Also, the diameter of the fragments decreased from 0.27 mm to 0.19 mm as the temperature of the sodium was increased from 250 to 820°C at a constant steel temperature of 2200°C.

British workers[3] used a pulse laser to heat up metal-foil samples under water. They then examined the resulting vapor-generation rates. The most significant parameters were the temperature of the foil and the degree of its dispersion. The observed modes of dispersion of material into the coolant were: (1) explosive boiling on a surface, (2) vapor-bubble collapse on a surface, (3) vapor-bubble collapse near a surface, (4) vapor-blanket collapse on a surface, and (5) disintegration while the target was vapor blanketed. Hot-metal particles remained suspended above a cool liquid surface by vapor generation with consequent low rates of energy transfer. The authors have termed this

Table IX-1 Results of Dynamic Tests of 304L Stainless-Steel Tubing in an Argon Atmosphere[1]

Heating rate, °C/sec	Internal pressure		Effective stress,* kg/mm²	Maximum test temp., °C	Expansion, %
	psig	kg/mm²			
0.3	304	0.214	1.55	1185	23
0.3	500	0.351	2.54	1098	32
20	500	0.351	2.54	1278	34
20	750	0.527	3.82	1190	34
20	750	0.527	3.82	1164	21
0.3	750	0.527	3.82	994	34
0.3	1000	0.703	5.10	950	31
0.3	1000	0.703	5.10	977	31
20	1000	0.703	5.10	1055	11
20	1000	0.703	5.10	1098	34
0.3	1500	1.054	7.60	888	29
20	1500	1.054	7.60	998	34

*Based on initial 1.27-cm inside diameter and 0.076-cm wall thickness.

new phenomenon the inverse Leidenfrost phenomenon.

Workers in Germany[4] have investigated the reaction of sodium and water in tubes in order to design a pressure-relief system for the KNK reactor. They found that, when pressurized water enters a sodium-filled tube, the water is supported by reaction products and ejects the sodium into the pressure-relief system. A cone of hydrogen is formed between the sodium and the water which reduces the reaction rate after strong initial reactions. A thin layer of sodium remains on the tube wall and reacts with the water flowing into the tube.

REFERENCES

1. General Electric Company, Missile and Space Division, AEC Fuels and Materials Development Program Progress Report No. 79, USAEC Report GEMP-1013, June 30, 1969.
2. Argonne National Laboratory, Reactor Development Program Progress Report, June 1969, USAEC Report ANL-7581, July 29, 1969.
3. A. J. Clare, R. B. Duffey, R. S. Hall, T. S. Playle, and D. H. Poole, Metal-Coolant Thermal Interactions at High Temperatures: Preliminary Results from a Laser Heating Experiment, British Report RD/B/N-1448, September 1969.
4. K. Dumm, H. Mausbeck, and W. Schnitker, The Reaction of Sodium and Water in Tubes, *Atomkernenergie*, 14: 309-318 (September–October 1969).

Index

Reactor Materials

Volume 13

The page range for each of the three issues of Vol. 13 is as follows:

No. 1, pages 1 to 60
No. 2, pages 61 to 106
No. 3, pages 107 to 154

3HK5S
  corrosion by liquid Na in contact with 316 stainless steel, 50

A

Actinides
  diffusion in UO_2, 118
Admiralty brass
  corrosion in low-oxygen flowing neutral water from 65 to 205°C, 46
Alumel
  thermoelectric properties, effect of irradiation on, 32
Aluminum
  annealing of irradiation damage in, effect of small amounts of Mg on, 34
  corrosion in Savannah River reactors, 135
  diffusion of Ce, La, Nd, Pi, and Sm in, 19
  diffusion of H_2 in, 122
  diffusion of Nb in, 120
  irradiation-induced swelling, effect of temperature on, 35
  solid solubility in Zr, 109
  tensile properties of silica-fiber-reinforced, effect of irradiation on, 32
Aluminum (2219)
  coating with Ni by vapor deposition, 99
Aluminum (6061)
  coating with Ni by vapor deposition, 99
  welding, 95–96
Aluminum (7075)
  stress-corrosion cracking, effect of point defects on, 135
Aluminum alloy (13Cr/4Al)
  corrosion in steam, 45
Aluminum alloys
  stress-corrosion cracking, 135
  thermal–mechanical treatment, DMIC review of Soviet literature on, 107
Aluminum alloys (Al–Cr–Hf–Ta)
  oxidation and tensile properties of, 141
Aluminum alloys (Al–Cr–Fe)
  irradiation embrittlement, 27
Aluminum alloys (Al–Cr–Fe–Y)
  mechanical properties, improvement by adding Mo, Nb, Ta, or W, 110
Aluminum alloys (Al–Hf–Nb–Ta–Ti–W)
  oxidation behavior, 114
Aluminum alloys (Al–Fe)
  magnetic properties, effect of irradiation on, 32
Aluminum alloys (Al–Li)
  grain growth of irradiated, 129
Aluminum alloys (Al–Mg)
  structural stability of tubes, effect of cyclic thermal treatment on, 1
Aluminum alloys (Al–Mg–Zr)
  phase diagram, 1
Aluminum alloys (Al–Mo)
  diffusion studies, 120
Aluminum alloys (Al–Mo–Nb–Sn–Zr)
  development for pressure-tube applications, 4
Aluminum alloys (Al–Mo–Zr)
  development for pressure-tube applications, 3–4
Aluminum alloys (Al–Nb)
  diffusion studies, 120
Aluminum alloys (Al–Sn–Ti)
  tensile properties of irradiated, 32
Aluminum alloys (Al–U)
  roll-separating forces during rolling of, 93
Aluminum bronze
  corrosion by liquid Na, 146
Aluminum composites (Al–Pm_2O_3)
  cold pressing into pellets, 92
Aluminum dispersions (Al–Al_2O_3)
  mechanical properties of, 1
Aluminum oxide dispersions (Al–Al_2O_3)
  mechanical properties of, 1
Armco iron
  corrosion by liquid Zn, 55–56
ASTAR 811C
  corrosion by liquid Li, 148–49
ASTAR 811CN
  corrosion by liquid Li, 148–49

B

B-1900
  longtime stability of carbide and intermetallic phases in, 9–10
Beryllium
  corrosion, effect of alloy additions, 86
  creep behavior of high-purity cast and extruded polycrystalline, 83–84
  diffusion in Ti and Zr, 120
  electroless-nickel deposition on, residual stresses resulting from, 84
  metallography of, 85
  powder metallurgy of, 84–85
  radiation effects, 85
  yield strength of wrought ingot, effect of Cu and Ag additions on, 83
Beryllium alloys (Be–Cr)
  powder metallurgy of, 83
Beryllium alloys (Be–Cu)
  corrosion by liquid Na, 146
  powder metallurgy of, 83
Beryllium alloys (Be–Cu–Zn)
  aging characteristics of neutron irradiated, 34
Beryllium alloys (Be–Fe)
  hardness and structure of arc melted and induction melted, effect of solution treating and aging on, 83
  powder metallurgy of, 83
Beryllium alloys (Be–Mn)
  powder metallurgy of, 83
Beryllium alloys (Be–Nb)
  powder metallurgy of, 83
Beryllium alloys (Be–Ti)
  powder metallurgy of, 83
Beryllium alloys (Be–Zr)
  powder metallurgy of, 83
Beryllium oxide (BeO)
  particles, coating with Ni by thermal decomposition of $Ni(CO)_4$, 99
Bismuth
  solubility in liquid Na, 149–50
Bismuth alloys (Bi–Pb)(liquid)
  corrosion of Cr–Mo steel, 150
  solubility of Cr in, 149–50
  solubility of Co in, 149–50
  solubility of Cu in, 149–50
  solubility of Fe in, 54–55
  solubility of Ni in, 149–50
  solubility of Ti in, 55
  solubility of Zr in, 55
Bismuth alloys (Bi–Sn)
  corrosion by liquid Na, 146–47
Boiling
  nucleate vs. film, eddy-current system for detection of, 102

This index was prepared by Theodore F. Davis of AEC's Division of Technical Information Extension, Oak Ridge, Tenn.

Books
"Corrosion of Zirconium and Zirconium Alloys", 137
"Defects and Radiation Damage in Metals", 32
"Liquid Metals", 52
Borides
pressure sintering, 92
Boron alloys (B–Cu)
irradiation embrittlement, 31
Boron alloys (B–Zr)
annealing of irradiated, 129
Boron carbide (B_4C)
compatibility with Na and 316 stainless steel, 89
irradiation swelling, 90
Boron nitride
hot pressing of powders, sintering during, 92
Boron nitride (BN)
compatibility with 316 stainless steel, 89
preparation of high-purity powders of, 90
Boron silicate systems (Cr–B_4Si–Si)
development as protective coatings for Mo, 48
Boron systems (B–graphite)
deposition of, 98
Braze alloy (Nicrobraz 30)
corrosion by liquid Na, 52
Braze alloy (Nicrobraz 50)
corrosion by liquid Na, 52

C

Cadmium alloys (Cd–Zn)
electrodeposition, 100–1
Carbides
pressure sintering, 92
Carbon
diffusion in Hf, 121
diffusion in Nb, Ta, and V, 19
diffusion in UC, 118
solubility in beta Zr, 2
Carbon systems (C–Hf–Re–W)
development for high-temperature applications, 14
Carbon systems (C–U)
phase studies, 65
Cb-753
creep properties, 15–16
Ceramics
corrosion by liquid Li, 148
Cerium
diffusion in Al, 19
Cermets
corrosion by liquid Li, 148
pressure sintering, 92
Cesium iodide
diffusion of ^{135}Xe in, 20
Chemical plating
interactions of vacuum-evaporated metals and solid-metal substrates, 96
review of vacuum evaporation, ion plating and sputtering techniques, 96
vacuum accelerated-ion deposition, 96
vapor deposition of metals by disproportionation reactions, 96
Chromel
thermoelectric properties, effect of irradiation on, 32
Chromium
corrosion by liquid Na, 143
density, 117
diffusion in Cr–Ni–Nb austenitic steel, 19
ductility, effect of addition of Cr on, 16
oxidation, 47, 140
solubility in liquid Bi–Pb, 149–50
solubility in liquid Na, 149–50
stress-corrosion cracking, 137
thermal expansion, 117
Chromium-51
diffusion into Nb, 18–19
Chromium alloys
stress-corrosion cracking, 137
Chromium alloys (Al–Cr–Hf–Ta)
oxidation and tensile properties of, 141
Chromium alloys (Al–Cr–Fe)
irradiation embrittlement, 27
Chromium alloys (Al–Cr–Fe–Y)
mechanical properties, improvement by adding Mo, Nb, Ta, or W, 110
Chromium alloys (Be–Cr)
powder metallurgy of, 83
Chromium alloys (Cr–Hf–Ta)
oxidation and tensile properties of, 141
Chromium alloys (Cr–Fe–Mo–Ni–Ti)
structure and properties of, effect of B additions on, 111
Chromium alloys (Cr–Fe–Ni)
stress-corrosion cracking, 135–36
Chromium alloys (Cr–Fe–Ni–Ti)
stress-rupture properties of irradiated tubing of, 26–27
Chromium alloys (Cr–Fe–Zr)
ductility, effect of autoclaving on, 23
ductility, effect of irradiation on, 23
tensile strength, effect of autoclaving on, 23
tensile strength, effect of irradiation on, 23
Chromium alloys (Cr–Mo)
corrosion by liquid Na in contact with 316 stainless steel, 50
Chromium alloys (Cr–Mo–V)(Nb stabilized)
corrosion by liquid Na in contact with 316 stainless steel, 50
Chromium alloys (Cr–Mo–V)(Ti stabilized)
corrosion by liquid Na in contact with 316 stainless steel, 50
Chromium alloys (Cr–Mo–V)(Zr stabilized)
corrosion by liquid Na in contact with 316 stainless steel, 50
Chromium alloys (Cr–Ni)
effect of W content on the transformation of the gamma prime to the stable eta phase, 111
morphology of the gamma prime precipitate in, effect of W additions on, 10
Chromium alloys (Cr–Pd–W)
oxidation, 139
Chromium alloys (Cr–Ti–V)
compatibility with PuO_2–UO_2, 62
corrosion by liquid Na, 147
density, 118
thermal conductivity, 117
thermal expansion, 117
Chromium alloys (Cr–U)
properties, 74
viscosity of liquid, effect of Cr content on, 73
Chromium alloys (Cr–V)
compatibility with PuO_2–UO_2, 62
corrosion by liquid Na, 147
Chromium alloys (Cr–Y)
oxidation, 47
Chromium alloys (Cr–Zr)
hardness of temperature aged, effect of Cr content on, 4
Chromium alloys (Co–Cr–Fe–Ni)
corrosion by liquid Na, 52–53
Chromium systems (Cr–B_4Si–Si)
development as protective coatings for Mo, 48
Chromium systems (Cr–Hf–Si–Ta)
oxidation and tensile properties, 141
Chromium systems (Cr–Fe–Si)
development as protective coating for D-43 alloy, 47–48
Chromium systems (Cr–UN)
phase studies, 68
Cladding materials
behavior in loss-of-coolant accidents, 59, 153–54
metallurgy of, 1–11, 107–11
Cobalt
corrosion by liquid Na, 143
solubility in liquid Bi–Pb, 149–50
Cobalt alloys
corrosion by liquid Hg, inhibition of, 53
corrosion by liquid Na, 52–53
Cobalt alloys (Co–Cr–Fe–Ni)
corrosion by liquid Na, 52–53
Cobalt alloys (Co–Fe)
magnetic properties, effect of irradiation on, 32
Cobalt alloys (Co–Fe–Ni)
ternary diffusion in, 121
Cobalt cermets (WC–Co)
fatigue behavior, effect of Co content on, 40
mechanical properties, dependence of carbide–carbide particle contacts on, 40
strength, theory of, 40
Concrete
creep behavior of moisture sealed at high temperatures, 42
creep in cylindrical prestressed pressure vessels exposed to a radial temperature gradient and internal pressure, numerical techniques for estimating redistribution of stresses due to, 42
development of low-radioactivity, 42
use as reactor containment structures, 133–34
Conferences and meetings
(see also Symposia)
on explosive metalworking, 101
on stress-corrosion cracking, 135
on Zr and Zr alloys, 107
Copel
thermoelectric properties, effect of irradiation on, 32
Copper
corrosion by liquid Bi, 55–56
heat capacity of, effect of irradiation on, 130
irradiation-induced swelling, effect of temperature on, 35
irradiation studies, 77
solubility in liquid Bi–Pb, 149–50
solubility in liquid Na, 149–50
tensile properties, effect of fast-neutron irradiation on, 33
thermoelectric properties, effect of irradiation on, 32
Copper alloys
thermal–mechanical treatment of, DMIC review of Soviet literature on, 107
Copper alloys (102)
weldability of, 94
Copper alloys (109)
weldability of, 94
Copper alloys (120)
weldability of, 94

Copper alloys (Be–Cu)
corrosion by liquid Na, 146
powder metallurgy of, 83
Copper alloys (Be–Cu–Zn)
aging characteristics of neutron irradiated, 34
Copper alloys (B–Cu)
irradiation embrittlement, 31
Copper alloys (Cu–Fe–Zr)
hydrogen absorption and embrittlement resistance of, 4
room-temperature mechanical properties, 109
Copper alloys (Cu–Ni)
corrosion in low-oxygen flowing neutral water from 65 to 205°C, 46
yield strength, effect of irradiation on, 33–34
Copper alloys (Cu–Nb–Zr)
mechanical properties of, 107
stress-corrosion cracking in methanol solutions, 137–38
Constantan
thermoelectric properties, effect of irradiation on, 32
Croloy 5
corrosion by liquid Na in contact with 316 stainless steel, 50
Croloy 5T1
corrosion by liquid Na in contact with 316 stainless steel, 50
Croloy 9M
corrosion by molten fluoride salts, 56–57

D

D-43 alloy
development of silicide coatings for, 47–48
precipitation behavior, 114–15
Diffusion studies
in ceramic fuels, 118
of gases in solids, 19–20, 121–22
in refractory metals, 18–19, 118–19
in structural materials, 120–21
Dysprosium oxide (Dy_2O_3)
elastic properties, 132–33

E

EI-872
corrosion by liquid Na, 56–57
Erbium oxide (Er_2O_3)
elastic properties, 132–33
Explosive metalworking, 101

F

Forges
design for determining the high-temperature formability and ductility of refractory metals, 93
FS-85
corrosion by fluoride salts, 151
protective coatings for, 140
Fuel plates
"dogboning" during rolling, methods for reducing, 93
electron-beam welding, 95–96
Fuel rods (UO_2)
fission-gas release during irradiation, 62
performance in Big Rock Point Reactor after central core melting, 62
Fuels
irradiation studies, 76–77

G

Gadolinium systems (Gd–H)
phase studies, 87–88
Gallium alloys (Ga–Pu)
mechanical properties, 75
Gold
thermoelectric properties, effect of irradiation on, 32
Gold alloys
stress-corrosion cracking, 135
Gold alloys (Au–Pd)
thermoelectric properties, effect of irradiation on, 32
Graphite
brazing to Hastelloy N, 95
brazing to Mo with Nb–Ti–Zr alloy, 95
brazing with Nb–Ti–Zr alloy, 95
coatings of, formation by the thermal decomposition of methane, 99
compatibility with fluoride salts, 150–51
effects of irradiation on boronated, 90
interaction with vacuum-deposited coatings of Mo, Nb, and Ti, 96
Poco, tensile properties, 132
pyrolytic, deposition at high temperatures and under fast-neutron irradiation, 98
tubes of, coating with SiC, 97–98
Graphite composites (NbC–graphite)
elastic properties, 132
Graphite systems (B–graphite)
deposition of, 98

H

Hafnium
diffusion of C in, 121
oxidation, 139
purification by electron-beam melting, 88–89
Hafnium alloys (Al–Cr–Hf–Ta)
oxidation and tensile properties of, 141
Hafnium alloys (Al–Hf–Nb–Ta–Ti–W)
oxidation behavior, 114
Hafnium alloys (Cr–Hf–Ta)
oxidation and tensile properties of, 141
Hafnium alloys (Hf–Mn)
phase diagram, 89
Hafnium alloys (Hf–Nb)
oxidation, 139
Hafnium alloys (Hf–W)
compatibility with molten U, 150
Hafnium boride (HfB_2)
bend strength of hot pressed, 90
Hafnium systems (C–Hf–Re–W)
development for high-temperature applications, 14
Hafnium systems (Cr–Hf–Si–Ta)
oxidation and tensile properties of, 141
Hastelloy C
corrosion in hot seawater vapor, 45
Hastelloy N
brazing to graphite, 95
compatibility with fluoride salts, 150–51
corrosion by molten fluoride salts, 56–57
diffusion of Ti in, 121
stress-rupture life of irradiated, effect of additions of Ti, 28
Hastelloy N (Ti modified)
corrosion by molten fluoride salts, 56–57
stress-rupture properties, 110
Hastelloy X
tensile properties of irradiated, effect of preirradiation thermomechanical treatments on, 28
welds, corrosion in steam, 137
Holmium oxide (Ho_2O_3)
elastic properties, 132–33
HS-25
corrosion by liquid Hg, 53
microstructure and precipitation kinetics, effect of high-temperature aging on, 10
Hydrogen
diffusion in Al, 122
diffusion in W, 19–20
diffusion through Pd, 121–22
Hydrogen systems (Gd–H)
phase studies, 87–88
Hydrogen systems (H–Zr)
phase studies, 86

I

IN-100
longtime stability of carbide and intermetallic phases in, 9–10
IN-102
welds, corrosion in steam, 137
Inco-713C
longtime stability of carbide and intermetallic phases in, 9–10
Incoloy 800
corrosion in steam, 45
creep properties of irradiated, 124, 126
ductility of irradiated, effect of preirradiation aging on, 28
welds, corrosion in steam, 137
Inconel
electrodeposition of TiB_2 on, 90
Inconel 102
tensile properties of He impregnated, 29–30
Inconel 600
corrosion by high-temperature borated water, 45
corrosion by NH_4OH water, 135
corrosion by liquid Na, 145
corrosion in the NPD Reactor, 135
irradiation-induced swelling, 35
welding, effect of minor alloying elements on hot cracking during, 94
Inconel 625
precipitation behavior and mechanical properties of, 110
rupture properties of irradiated, 125
tensile properties of irradiated, effect of preirradiation thermomechanical treatments on, 28
welds, corrosion in steam, 137
Inconel 718
brazing with Nicrobraz 50 alloy, 94
longtime stability of carbide and intermetallic phases in, 9–10
longtime stability of, effect of grain size on, 111
precipitation strength of, 111
rupture properties of irradiated, 125
stability of, effect of thermal–mechanical treatment on, 111
tensile properties of irradiated, effect of preirradiation thermomechanical treatments on, 28

Inconel X-750
corrosion by liquid Na, 146
tensile properties of He impregnated, 29–30
Indium
electrodeposition, 101
Iridium
coupled with W, interdiffusion studies of, 18
Iron
corrosion by liquid Na, 143
diffusion in V, isotope effect on, 120–21
diffusion of O_2 in, 122
flow stress of irradiated, effect of N on, 33
mechanical properties, effect of irradiation on, 32
neutron-radiation hardening of polycrystalline, 129–30
postirradiation and co-irradiation annealing of, 34
solubility in Bi–Pb alloys, 54–55
stress-corrosion cracking, 137
stress–strain properties of irradiated single crystals containing small amounts of C, 33
thermoelectric properties, effect of irradiation on, 32
Iron alloys
stress-corrosion cracking, 137
Iron alloys (Al–Cr–Fe)
irradiation embrittlement, 27
Iron alloys (Al–Cr–Fe–Y)
mechanical properties, improvement by adding Mo, Nb, Ta, or W, 110
Iron alloys (Al–Fe)
magnetic properties, effect of irradiation on, 32
Iron alloys (Be–Fe)
hardness and structure of arc melted and induction melted, effect of solution treating and aging on, 83
powder metallurgy of, 83
Iron alloys (Cr–Fe–Mo–Ni–Ti)
structure and properties of, effect of B additions on, 111
Iron alloys (Cr–Fe–Ni)
stress-corrosion cracking, 135–36
Iron alloys (Cr–Fe–Ni–Ti)
stress–rupture properties of irradiated tubing of, 26–27
Iron alloys (Cr–Fe–Zr)
ductility, effect of autoclaving on, 23
ductility, effect of irradiation on, 23
room-temperature mechanical properties, 109
tensile strength, effect of autoclaving on, 23
tensile strength, effect of irradiation on, 23
Iron alloys (Co–Cr–Fe–Ni)
corrosion by liquid Na, 52–53
Iron alloys (Co–Fe)
magnetic properties, effect of irradiation on, 32
Iron alloys (Co–Fe–Ni)
ternary diffusion in, 121
Iron alloys (Cu–Fe–Zr)
hydrogen absorption and embrittlement resistance of, 4
Iron alloys (Fe–Mo)
diffusion of Mo in, 120
Iron alloys (Fe–Ni)
magnetic properties, effect of irradiation on, 32
Iron alloys (Fe–Ni–Nb–Sn–Zr)
room-temperature mechanical properties, 109
Iron alloys (Fe–U)
roll-separating forces during rolling of, 93
welding, hot cracking during, 94
Iron alloys (Fe–V–Zr)
room-temperature mechanical properties, 109
Iron systems (Cr–Fe–Si)
development as protective coating for D-43 alloy, 47–48
Iron systems (Fe–Si)
magnetic properties, effect of irradiation on, 32

L

L-605
cavitation damage in liquid Na, effect of temperature and pressure on, 51–52
Lanthanum
diffusion in Al, 19
Lead alloys (Bi–Pb)(liquid)
corrosion of Cr–Mo steel, 150
solubility of Cr in, 149–50
solubility of Co in, 149–50
solubility of Cu in, 149–50
solubility of Fe in, 54–55
solubility of Ni in, 149–50
solubility of Ti in, 55
solubility of Zr in, 55
Lead alloys (Pb–Pu)
phase studies, 75
Lead alloys (Mg–Pb–Zr)
use as fuel-element can, 1
Liquid metals
book on, 52
Lithium
growth of single crystals of, 87
Lithium alloys (Al–Li)
grain growth of irradiated, 129
Lithium hydride
radiation decomposition, 87
Lithium–plutonium oxides (Li_4PuO_5)
crystal structure and thermal stability of, 63
Lithium–plutonium oxides (Li_8PuO_6)
crystal structure and thermal stability of, 63
Lucalox
tensile properties, 132

M

Magnesium alloys (Al–Mg)
structural stability of tubes, effect of cyclic thermal treatment on, 1
Magnesium alloys (Al–Mg–Zr)
phase diagram, 1
Magnesium alloys (Mg–Pb–Zr)
use as fuel-element can, 1
Magnesium alloys (Mg–Pu)
diffusion interactions with Al–Mg, Ga–Mg, Ge–Mg, Pb–Mg, Mg–Si, or Mg–Sn alloys, 75
Magnesium oxide (MgO)
diffusion of Th in, 118
Magnetic alloys
effect of irradiation on, 32
Magnox alloy
corrosion in CO_2 at 20 atm and above 500°C, 45–46
Manganese alloys (Be–Mn)
powder metallurgy of, 83
Manganese alloys (Hf–Mn)
phase diagram, 89
MAR-M200
longtime stability of carbide and intermetallic phases in, 9–10
MAR-M246
longtime stability of carbide and intermetallic phases in, 9–10
Metal crystals
mechanism for sweeping up of loops by glide dislocations during deformation of irradiated, 32–33
Metal hydrides
book on, 86
Metals
corrosion by liquid Li, 148
defects and irradiation damage in, book on, 32
thermal–mechanical treatment of, DMIC review of Soviet literature on, 107
Microscopes
development of infrared, 102
Molybdenum
brazing to graphite with Nb–Ti–Zr alloy, 95
coating with pore-free layer of $MoSi_2$, 97
coating with thin films of Nb, Ta, and V, 96
corrosion by liquid Na, 52
diffusion in Fe–Mo alloy, 120
diffusion of N_2 in, 122
electrodeposition, 100
electron-beam welding to Kh18N10T stainless steel, 95
electron-beam welding to Nb, 95
irradiation-induced swelling, effect of temperature and fluence on, 35
preparation from $MoCl_5$, 96
solubility in liquid K, 149–50
solubility in liquid Na, 149–50
surface self-diffusion of, effect of crystallographic orientation on, 118–19
thermoelectric properties, effect of irradiation on, 32
vapor deposition, 98
Molybdenum alloys
corrosion by liquid Na, 52–53
development of silicide coatings for, 48
hot hardness of irradiated, 127
use in alkali-metal Rankine-cycle systems, 53
Molybdenum alloys (Al–Mo)
diffusion studies, 120
Molybdenum alloys (Al–Mo–Nb–Sn–Zr)
development for pressure-tube applications, 4
Molybdenum alloys (Al–Mo–Zr)
development for pressure-tube applications, 3–4
Molybdenum alloys (Cr–Fe–Mo–Ni–Ti)
structure and properties of, effect of B additions on, 111
Molybdenum alloys (Cr–Mo)
corrosion by liquid Na in contact with 316 stainless steel, 50
Molybdenum alloys (Cr–Mo–V)(Nb stabilized)
corrosion by liquid Na in contact with 316 stainless steel, 50
Molybdenum alloys (Cr–Mo–V)(Ti stabilized)
corrosion by liquid Na in contact with 316 stainless steel, 50
Molybdenum alloys (Cr–Mo–V)(Zr stabilized)
corrosion by liquid Na in contact with 316 stainless steel, 50

Molybdenum alloys (Fe–Mo)
diffusion of Mo in, 120
Molybdenum alloys (Mo–Nb)
diffusion studies, 120
Molybdenum alloys (Mo–Nb–Sn–Zr)
development for pressure-tube applications, 3–4
Molybdenum alloys (Mo–Re–W)
corrosion by liquid Li, 54
nitriding, effect of Hf content on, 117
Molybdenum alloys (Mo–Sn–Zr)
development for pressure-tube applications, 4
Molybdenum alloys (Mo–Ti)
protective coatings, 141
siliconizing and boriding by reaction with $SiCl_2$ and BF vapors, 96–97
Molybdenum alloys (Mo–U)
casting of cylinders of, 92
irradiation behavior, effect of Al and Sn additions on, 73
properties, 74
Molybdenum systems (Mo–Nb–Si–Sn–Zr)
development for pressure-tube applications, 4
Molybdenum systems (Mo–Si–Ti)
development as protective coatings for Ta, 48
Mo-TZM
corrosion by liquid K, 53
Monel
corrosion in low-oxygen flowing neutral water from 65 to 205°C, 46
Monel 400
corrosion in the NPD Reactor, 135

N

Neodymium
diffusion in Al, 19
Nichrome
thermoelectric properties, effect of irradiation on, 32
Nickel
corrosion by liquid Na, 143
diffusion in Cr–Ni–Nb austenitic steel, 19
diffusion of O_2 in, 122
electrodeposition, 100
electroless deposition on 6061 and 2219 Al, 99
irradiation-induced swelling, effect of temperature on, 35
irradiation-induced voids in, 125
solubility in liquid Bi–Pb, 149–50
stress-corrosion cracking, 137
vapor deposition, 98
Nickel 200
corrosion by liquid Na, 145
irradiation-induced swelling, 35
Nickel 270
irradiation-induced swelling, 35
Nickel alloy (13Cr/4Al)
corrosion in steam, 45
Nickel alloy (16/75)
corrosion in steam, 45
Nickel alloys
corrosion by liquid Na, 52–53
irradiation embrittlement of precipitation hardened, 24–26
irradiation embrittlement of solid-solution hardened, 24–26
phase transformation in, effect of W additions on, 10
stability of precipation hardened, effect of W additions on, 10
thermal–mechanical treatment of, DMIC review of Soviet literature on, 107
Nickel alloys (Cr–Fe–Mo–Ni–Ti)
structure and properties of, effect of B additions on, 111
Nickel alloys (Cr–Fe–Ni)
stress-corrosion cracking, 135–37
Nickel alloys (Cr–Fe–Ni–Ti)
stress-rupture properties of irradiated tubing of, 26–27
Nickel alloys (Cr–Ni)
morphology of the gamma-prime precipitate in, effect of W additions on, 10
Nickel alloys (Co–Cr–Fe–Ni)
corrosion by liquid Na, 52–53
Nickel alloys (Co–Fe–Ni)
ternary diffusion in, 121
Nickel alloys (Cu–Ni)
corrosion in low-oxygen flowing neutral water from 65 to 205°C, 46
yield strength, effect of irradiation on, 33–34
Nickel alloys (Fe–Ni)
magnetic properties, effect of irradiation on, 32
Nickel alloys (Fe–Ni–Nb–Sn–Zr)
room-temperature mechanical properties, 109
Nicrobraz 30
corrosion by liquid Na, 52
Nicrobraz 50
corrosion by liquid Na, 52
Nimonic 80A
mechanical properties, effect of cold working before solution annealing on, 9
Niobium
chemical deposition onto Mo, 96
corrosion by liquid Na, 52
corrosion by liquid K, 149
creep properties, 15–16
creep-rupture data compilation on, 17
deposition onto UC, 99
diffusion in Al, 120
diffusion in W, 119
diffusion of C into, 19
diffusion of ^{51}Cr into, 18–19
electron-beam welding to Mo, 95
oxidation, 139
preparation from $NbCl_5$, 96
Niobium alloys
corrosion by liquid Na, 52–53
creep-rupture data compilation on, 17
hot hardness of irradiated, 127
room-temperature mechanical properties, 109
use in alkali-metal Rankine-cycle systems, 53
Niobium alloys (Al–Hf–Nb–Ta–Ti–W)
oxidation behavior, 114
Niobium alloys (Al–Mo–Nb–Sn–Zr)
development for pressure-tube applications, 4
Niobium alloys (Al–Nb)
diffusion studies, 120
Niobium alloys (Be–Nb)
powder metallurgy of, 83
Niobium alloys (Cu–Nb–Zr)
mechanical properties of, 107
stress-corrosion cracking in methanol solutions, 137–38
Niobium alloys (Hf–Nb)
oxidation, 139
Niobium alloys (Mo–Nb)
diffusion studies, 120
Niobium alloys (Mo–Nb–Sn–Zr)
development for pressure-tube applications, 3–4
Niobium alloys (Nb–Ta)
corrosion in HCl, HNO_3, and H_2SO_4, 47
Niobium alloys (Nb–Ta–Zr)
room-temperature mechanical properties, 109
Niobium alloys (Nb–Ti)
corrosion in air, O_2, and N_2 at 650 to 1000°C, 47
corrosion in KOH, 47
protective coatings for, 140–41
Niobium alloys (Nb–W)
properties of, effect of small chemical additions on, 93
Niobium alloys (Nb–TZM)
creep-rupture properties, effect of fabrication variables on, 115
Niobium alloys (Nb–U)
properties, 74
Niobium alloys (Nb–U–Zr)
properties, 74
TTT diagram for, 73–74
Niobium alloys (Nb–V–Zr)
development for pressure-tube applications, 3–4
Niobium alloys (Nb–Zr)
corrosion by fluoride salts, 151
corrosion by liquid Hg, 53
corrosion by liquid Na, 53
corrosion by Li–K vapor, 148
corrosion by steam, effect of irradiation on, 137
corrosion in the NPD Reactor, 135
crystallographic texture after rolling at several temperatures, 93
development for pressure-tube applications, 4
effect of changing the corrosive medium from 200 atm of steam to 1 atm of air on oxidation of, 44
fatigue-crack growth and propagation in pressure tubing, 6–7
mechanical properties, 107
mechanical properties and structure of, effect of internal oxidation on, 16
performance in high-temperature steam, effect of irradiation on, 3–4
postirradiation deformation, effect of irradiation temperature on, 23
stress-corrosion cracking in methanol solutions, 137–38
stress-rupture properties, effect of internal oxidation on, 16
stress-rupture properties of pressure tubes, 5–7
structural transformations in, 109
tensile strength, effect of O_2 content, Nb content, and cold working on, 5–6
Niobium carbide (NbC)
elastic properties, 132
external friction at high temperatures in a vacuum, 39
thermal expansion, 132
Niobium carbide composites (NbC–graphite)
elastic properties, 132
Niobium systems
phase studies, 68
Niobium systems (Mo–Nb–Si–Sn–Zr)
development for pressure-tube applications, 4
Nitrides
pressure sintering, 92
Nitrogen
diffusion in Mo, 122

O

Oxides
pressure sintering, 92

Oxygen
diffusion in Fe, 122
diffusion in Ni, 122
Oxygen systems (O–Pu–U)
lower limit of PuO_2 concentration for the two-phase boundary in, 63–64
phase studies, 63
Ozhennite
mechanical properties of, 109
performance in high-temperature steam, effect of irradiation on, 3–4

P

Palladium
diffusion of H_2 through, 121–22
hydrogenated, irradiation effect on serrated yielding in, 129–30
thermoelectric properties, effect of irradiation on, 32
Palladium alloys (Au–Pd)
thermoelectric properties, effect of irradiation on, 32
Palladium alloys (Cr–Pd–W)
oxidation, 139
Platinum
thermoelectric properties, effect of irradiation on, 32
Platinum alloys (Pt–Rh)
thermoelectric properties, effect of irradiation on, 32
Plutonium
elastic constant measurements, 74
high-pressure studies of the crystal growth of alpha, 74
Russian monograph on properties, metallurgy, and technology of, 72–73
Plutonium (liquid)
solubility of La in, 75
Plutonium-236
electrodeposition, 101
Plutonium-238
electrodeposition, 101
Plutonium alloys
elastic and anelastic behavior of delta-stabilized, 74–75
irradiation studies, 76
Plutonium alloys (Ga–Pu)
mechanical properties, 75
Plutonium alloys (Pb–Pu)
phase studies, 75
Plutonium alloys (Mg–Pu)
diffusion interactions with Al–Mg, Ga–Mg, Ge–Mg, Pb–Mg, Mg–Si, or Mg–Sn alloys, 75
Plutonium alloys (Pu–U–Zr)
irradiation studies, 75
Plutonium alloys (Pu–Zr)
delta stabilized, chemical diffusivities of, 118
Plutonium carbide systems (PuC–UC)
irradiation studies, 66–67
Plutonium carbide systems (PuC_2–UC_2)
immiscibility, 65
Plutonium carbide systems (Pu,U)C
compatibility with austenitic stainless steels, effect of Na bonding on, 65
pellet fabrication problems, 65
Pu volatilization from, 92
sintering, use of Ni and PuC as aids in, 66
Plutonium carbides
bar fabrication by extrusion, French patents for, 65–66
irradiation studies, 76
preparation of high-density, French patent for, 65
Plutonium carbides (Pu_2C_3)
vapor-pressure studies, 65
Plutonium nitride systems
compatibility with stainless steel, 69
Plutonium nitride systems (PuN–UN)
fabrication, 69
Plutonium nitride systems ((Pu,U)N)
irradiation studies, 70
Plutonium oxide ($^{238}PuO_2$)
effective alpha activity of microspheres of, 63
impact tests of plasma-fired microspheres of, 63
Plutonium oxide (PuO_2)
heat content from 1225 to 1885°C, 63
preparation of microparticles of, 64
vapor pressure, effect of stoichiometry on, 62–63
Plutonium oxide (Pu_2O_3)
coating with pyrolytic carbon, 99
Plutonium oxide systems (PuO_2–UO_2)
compatibility with Cr–Ti–V alloy, 62
compatibility with Cr–V alloy, 62
compatibility with Re–W alloy, 62
compatibility with 304 stainless steel, 62
irradiation studies, 64–65
irradiation studies of vibratory-compacted fuel elements of, 64
O_2 migration in, from 1200 to 2000°C, 62
preparation of single-phase, sintering parameters for, 63
production of microspheres, sol-gel techniques for, 64
Plutonium oxides
irradiation studies, 76
Plutonium–sodium oxides (Na_4PuO_5)
crystal structure and thermal stability of, 63
Plutonium–sodium oxides (Na_5PuO_6)
crystal structure and thermal stability of, 63
Plutonium systems (Pu–U–O)
phase studies, 63
lower limit of PuO_2 concentration for the two-phase boundary in, 63–64
Potassium (liquid)
solubility of Mo and W in, 149–50
Praseodymium
diffusion in Al, 19
Promethium oxide composites (Al–Pm_2O_3)
cold pressing into pellets, 92

R

R512C
development as protective coating for Ta, 48
R512E
development as protective coating for D-43 alloy, 47–48
Radioisotope heat sources
development of diffusion barriers between inner and outer claddings of, 18
Rare-earth hydrides
review on, 86
Reactor containment structures
use of concrete for, 42, 133–34
Reactor pressure tubes
development of Zr-base alloys for, 3–4
fatigue-crack growth and propagation in Zr–Nb alloys, 6–7
gauging equipment, 102
stress-rupture properties of Zr–Nb alloy, 5–7
Reactors (Fast Flux Test Facility)
fuel preparation for, 64
Reactors (LMFBR)
component materials for, survey of limitations and requirements of, 107
Refractory metals
corrosion by aqueous and gaseous media, 47–48, 139–41
corrosion by liquid Li, 148
corrosion by liquid, Cs, Li, Hg, K, and Na, 53
high-temperature formability and ductility of, design of forge for measurement of, 93
metallurgy of, 14–17, 114–17
protective coatings, seminar on, 141
thermal–mechanical treatment of, DMIC review of Soviet literature on, 107
Rene 41
cavitation damage in liquid Na, 52
longtime stability of carbide and intermetallic phases in, 9–10
Rhenium
corrosion in HNO_3, H_3PO_4, H_2SO_4, and KoH, 47
coupled with 304 stainless steel, development of Al_2O_3 and B_6Si diffusion barriers for, 18
coupled with W, interdiffusion studies of, 18
creep-rupture data compilation on, 17
deposition on expendable microspherical substrates to form thin-walled microballoons, 99
high-temperature recovery of irradiated, 130
oxidation, 47
stress in electroplates of, method for reducing, 100
tensile creep of high-purity polycrystalline, 15
thermoelectric properties, effect of irradiation on, 32
Rhenium alloys
creep-rupture data compilation on, 17
Rhenium alloys (Mo–Re–W)
corrosion by liquid Li, 54
nitriding, effect of Hf content on, 117
Rhenium alloys (Re–W)
compatibility with PuO_2–UO_2, 62
coupled with 304L stainless steel, development of Al_2O_3 and B_6Si diffusion barriers for, 18
nitriding, effect of Hf content on, 117
vapor deposition, 98
Rhenium systems (C–Hf–Re–W)
development for high-temperature applications, 14
Rhodium
coupled with W, interdiffusion studies of, 18
thermoelectric properties, effect of irradiation on, 32
Rhodium alloys (Pt–Rh)
thermoelectric properties, effect of irradiation on, 32
Ruthenium
reaction with UN to form URu_3 and N_2, 68
thermoelectric properties, effect of irradiation on, 32

S

Samarium
diffusion in Al, 19

SCb-291
corrosion by fluoride salts, 151
Seminars
on protective coatings for refractor metals, 141
Silicides
pressure sintering, 92
Silicon carbide (SiC)
creep behavior in air between 1000 and 1300°C, 39–40
fracture strength, effect of multiaxial stresses on, 39
impact resistance, effect of specimen geometry and structure on, 39
KT, tensile properties, 132
Silicon systems (Cr–B_4Si–Si)
development as protective coatings for Mo, 48
Silicon systems (Cr–Hf–Si–Ta)
oxidation and tensile properties of, 141
Silicon systems (Cr–Fe–Si)
development as protective coating for D-43 alloy, 47–48
Silicon systems (Fe–Si)
magnetic properties, effect of irradiation on, 32
Silicon systems (Mo–Nb–Si–Sn–Zr)
development for pressure-tube applications, 4
Silicon systems (Mo–Si–Ti)
development as protective coatings for Ta, 48
Silicon systems (Si–U)
roll-separating forces during rolling of, 93
Silver alloys
stress-corrosion cracking, 135
Sodium (liquid)
solubility of Bi, Cr, Cu, Mo, and Ti in, 149–50
Sodium–plutonium oxides (Na_4PuO_5)
crystal structure and thermal stability of, 63
Sodium–plutonium oxides (Na_6PuO_6)
crystal structure and thermal stability of, 63
Special fabrication techniques, 92–102
Stainless steel (1Kh18N10T)
weld joints of tubing of, corrosion by liquid Li, 54
Stainless steel (2Kh13)
weld joints of tubing of, corrosion by liquid Li, 54
Stainless steel (4Kh13)
corrosion by liquid Bi–Pb alloys, 55
Stainless steel (15-5PH)
stress-corrosion cracking in 3.5 wt.% NaCl solution, 136
Stainless steel (15/15)
corrosion in steam, 45
Stainless steel (16/13)
radiation-induced embrittlement, effect of cold working on, 125
Stainless steel (17-4PH)
corrosion by liquid Na, 146
Stainless steel (18-8)
mechanical properties, effect of heat treatment on, 11
Stainless steel (18/11)
corrosion in steam, 45
Stainless steel (18-18-2)
tensile properties, effect of C-contaminated liquid Na on, 49–50
tensile properties, effect of O_2-contaminated liquid Na on, 49–50
Stainless steel (19-9L)
tensile properties of He impregnated, 28–29
Stainless steel (20/25)
corrosion in steam, 45
Stainless steel (20/25 Nb)
corrosion in steam, 45
oxidation, reactions between individual oxides formed during, 45
Stainless steel (20/35)
corrosion in steam, 45
Stainless steel (20Cr–25Ni–Nb)
creep-fracture damage of irradiated, annealing of, 35–36
Stainless steel (304)
biaxial stress-rupture behavior in Cu-contaminated liquid Na, 50
compatibility with PuO_2–UO_2, 62
corrosion by fuel-storage-basin water, 136
corrosion by liquid Na, 143–44, 146
corrosion in the NPD Reactor, 135
corrosion by NH_4OH water, 135
corrosion by O_2-contaminated liquid Na, 49
corrosion by H_2O containing fluoride ions, 136
creep properties, 8
creep-rupture properties, effect of C additions on, 8
creep-rupture properties of irradiated, 26
density, 117
fatigue life, effect of strain-hold time on, 8
fatigue life, prediction method for, 8–9
irradiation-induced swelling, effect of temperature and fluence on, 34–35
mechanical properties of irradiated, data compilation on, 124
notched high-strain behavior of, 112
rupture properties, 8
stress-corrosion in water, 136
stress-fatigue behavior in liquid Na, 49
stress-rupture behavior in liquid Na, 49, 144–45
stress-rupture properties of the impregnated, 28–29
tensile properties, 8
tensile properties of irradiated, 24
thermal conductivity, 117
thermal expansion, 117
ultrasonic-shear velocity of irradiated, correlation with room-temperature ductility, 29–30
Stainless steel (304)(Ti modified)
helium-induced embrittlement, effect of heat treatment on, 29
tensile properties of irradiated, effect of irradiation temperature on, 23–24
Stainless steel (304L)
behavior as fuel-cladding material during loss-of-coolant accidents, 153
corrosion by liquid Na, 145–46
corrosion by molten fluoride salts, 56–57
coupled with Re, Ta, W, TZM, and Re–W alloys, development of Al_2O_3 and B_4Si diffusion barriers for, 18
deep-grain boundary attack by C-contaminated liquid Na, 50
diffusion in U–Fs alloys, 118–19
void density in irradiated, 124, 127
Stainless steel (304L)(Ti modified)
production of tubes for LMFBR cladding, 92–93
tensile properties of irradiated, effect of irradiation temperature on, 23–24
Stainless steel (316)
burst strength of tubes of, effect of surface defects on, 109
carbide precipitation in, 8
cavitation damage in liquid Na, 52
cold work in, determination by ultrasonic critical-angle reflectivity tests, 110
corrosion by liquid Na, 143–44
corrosion by O_2-contaminated liquid Na, 49
corrosion by H_2O containing fluoride ions, 136
creep properties, 8
creep rate of irradiated tubing of, 26–27
creep-rupture properties of irradiated, 26
cyclic-strain fatigue life, 27–28
cyclic-strain fatigue life of irradiated, 27–28
density, 117
fatigue life, effect of O_2 pressure on, 8–9
mechanical properties of irradiated, data compilation on, 124
rupture properties, 8
stress-fatigue behavior in liquid Na, 49
stress-rupture behavior in liquid Na, 49, 144–45
tensile properties, 8
tensile properties of irradiated, 24
tensile properties of irradiated, effect of irradiation temperature on, 23–24, 124–25
thermal conductivity, 117
thermal expansion, 117
tube fabrication by planetary swaging, 110
Stainless steel (316)(Ti modified)
tensile properties of irradiated, effect of irradiation temperature on, 23–24
Stainless steel (316L)
tensile properties of irradiated, effect of irradiation temperature on, 23–24
Stainless steel (316L)(Ti modified)
tensile properties of irradiated, effect of irradiation temperature on, 23–24
Stainless steel (318)
cavitation damage in liquid Na, 52
Stainless steel (321)
creep properties, 8
rupture properties, 8
tensile properties, 8
Stainless steel (340)
corrosion by liquid Na, 146
Stainless steel (347)
corrosion by liquid Na, 146
creep properties, 8
cyclic-strain fatigue life of irradiated, 27–28
rupture properties, 8
tensile properties, 8, 23–25
tensile properties of irradiated, 23–25
Stainless steel (410)
corrosion in NPD Reactor, 135
Stainless steel (416)
corrosion by liquid Na, 146
Stainless steel (420)
corrosion by liquid Na, 146
Stainless steel (A-286)
stress-corrosion cracking in 3.5 wt.% NaCl solution, 136
Stainless steel (Almar 362)
stress-corrosion cracking in 3.5 wt.% NaCl solution, 136

Stainless steel (Kh18N10T)
electron-beam welding to Mo, 95
Stainless steel (PH13-8Mo)
stress-corrosion cracking in 3.5 wt.% NaCl solution, 136
Stainless steel (PH14-8Mo)
stress-corrosion cracking in 3.5 wt.% NaCl solution, 136
Stainless steel (Unitemp 212)
stress-corrosion cracking in 3.5 wt.% NaCl solution, 136
Stainless steels
compatibility with (U,Pu)N, 69
corrosion by liquid Na, 52
electrochemical machining, 101
tensile properties of irradiated, effect of irradiation temperature on, 24–25
thermal–mechanical treatment, DMIC review of Soviet literature on, 107
Stainless steels (austenitic)
compatibility with (U,Pu)C, effect of Na bond on, 65
corrosion by liquid Na, 145
corrosion by liquid Na in contact with austenitic stainless steel, 50–51
creep-rupture properties of irradiated, 26
hydrogen embrittlement, 9
irradiation embrittlement, 24–26
irradiation embrittlement, effect of addition of Ti on, 23
stress-corrosion cracking in high-temperature water, 44–45
tensile and impact properties, 7
tensile properties of irradiated, 26
Stainless steels (ferritic)
corrosion by liquid Na in contact with austenitic stainless steel, 50–51
Stainless steels (molten)
quenching in molten Na, effect of temperature on fragment sizes produced by, 153
Steel (2RM2)
properties, 111
Steel (A-302B)
fatigue-crack growth rates, 11
low-cycle fatigue deformation, effect of mean stress on, 112
mechanical properties, effect of long-time heat treatment on, 11
tempering properties, 11
Steel (A-350LF1)(modified)
notch-ductility response, effect of irradiation and annealing cycles on, 30–31
Steel (A421-65, Type BA)
corrosion, 135–36
Steel (A-533B)
plane-strain fracture properties, 11
Steel (RMO)
properties, 111
Steel (T1 tool)
corrosion by liquid Na, 146
Steels
mechanical properties, effect of irradiation on, 32
postirradiation and co-irradiation annealing of, 34
stress-corrosion cracking, 135
thermal–mechanical treatment of, DMIC review of Soviet literature on, 107
Steels (carbon)
corrosion by liquid Na in contact with austenitic stainless steel, 50–51
mechanical properties, effect of heat treatment on, 11
Steels (Cr–Mo)
corrosion by liquid Bi–Pb alloy, 150
Steels (Cr–Mo–Ni–V)
fracture strength, 11
Steels (Cr–Mo–V)
creep and rupture properties of large steam-turbine rotor forgings, improvement of, 10–11
Steels (Cr–Ni–Nb)
diffusion of Cr and Ni in, 19
irradiation-induced precipitation in, 125–26
Steels (ferritic)
corrosion by liquid Bi–Pb alloys, 54–55
corrosion by liquid Na, 52–53
development for use with austenitic stainless steels in liquid Na, 10
irradiation embrittlement, effect of Cr content on, 27
radiation-induced change in ductile-to-brittle transition, prediction of, 34
Steels (ferritic–pearlitic)
corrosion by liquid Na, 52
Steels (low alloy)
corrosion by liquid Na, 145–46
corrosion by liquid Na in contact with austenitic stainless steel, 50–51
Steels (low carbon)
notched high-strain behavior of, 112
Steels (martensitic)
irradiation embrittlement, 24–26
Steels (mild)
corrosion in NH_4OH water, 135
Steels (pearlitic)
corrosion by liquid Na, 52
Steels (pressure vessel)
(see also Steel (A-302B), Steel (A-350LF1)(modified), Steel (2RM2), and Steel (RMO))
neutron-irradiation embrittlement, 31, 126–27, 131
Stellite 6B
corrosion by liquid Na, 146
Structural materials
radiation effects on, 21–36, 124–30
Symposia
(see also Conferences and meetings)
"Irradiation Effects in Structural Alloys for Thermal and Fast Reactors", 124

T

T-111
corrosion by liquid Hg, 53
corrosion by liquid Li, 148–49
high-temperature creep data, 115–16
T-222
high-temperature creep data, 115–16
protective coatings for, 140
Tantalum
chemical deposition onto Mo, 96
corrosion by CO_2 at 700 to 950°C, 47
corrosion by liquid Na, 146
corrosion by Hg vapor, 149
coupled with 304 stainless steel, development of Al_2O_3 and B_6Si diffusion barriers for, 18
coupled with W, interdiffusion studies of, 18
creep properties, 15–16
creep-rupture data compilation on, 17
diffusion in W, 119
diffusion of C into, 19
diffusion of W into, 119
oxidation, 139
preparation from $TaCl_5$, 96
solid-solution strengthening and precipitation hardening, effect of additions of C, Hf, Mo, Nb, Re, and W on, 16
tensile properties of irradiated, 127–28
thermoelectric properties, effect of irradiation on, 32
vapor deposition, 98
Tantalum alloys
corrosion by liquid Na, 52–53
creep-rupture data compilation on, 17
development of silicide coatings for, 48
hot hardness of irradiated, 127
use in alkali-metal Rankine-cycle systems, 53
Tantalum alloys (Al–Cr–Hf–Ta)
oxidation and tensile properties, 141
Tantalum alloys (Al–Hf–Nb–Ta–Ti–W)
oxidation behavior, 114
Tantalum alloys (Cr–Hf–Ta)
oxidation and tensile properties of, 141
Tantalum alloys (Nb–Ta)
corrosion in HCl, HNO_3, and H_2SO_4, 47
Tantalum alloys (Nb–Ta–Zr)
room-temperature mechanical properties, 109
Tantalum alloys (Ta–W)
tensile properties of irradiated, 127, 129
Tantalum carbide (TaC)
external friction at high temperatures in a vacuum, 39
Tantalum couples (C–Ta)
diffusion studies, 121
Tantalum nitride (TaN)
solubility in UN, 68
Tantalum systems
phase studies, 68
properties, 68
Tantalum systems (Cr–Hf–Si–Ta)
oxidation and tensile properties of, 141
Testing (nondestructive), 101–2
Thermocouples
effect of irradiation on, 32
Thorium
diffusion in MgO, 118
electrical conductivity, 72
Russian monograph on properties, metallurgy, and technology of, 72–73
thermal conductivity, 72
Thorium alloys (Th–U)
physical properties, 71–72
Thorium carbide (ThC)
preparation of high-density, French patent for, 65
Thorium carbide (ThC_2)
preparation, sol-gel process for, 66
Thorium carbide systems $(Th,U)C_2$
preparation, sol-gel process for, 66
Thorium oxide (ThO_2)
coating of particles with pyrolytic carbon, 99
preparation of porous, 61
surface diffusion measurements in, 61
Thorium oxide systems (ThO_2–UO_2)
surface diffusion measurements in, 61
thermal conductivity from 20 to 500°C, 61
Tin alloys (Al–Mo–Nb–Sn–Zr)
development for pressure-tube applications, 4
Tin alloys (Al–Sn–Ti)
tensile properties of irradiated, 32
Tin alloys (Bi–Sn)
corrosion by liquid Na, 146–47
Tin alloys (Fe–Ni–Nb–Sn–Zr)
room-temperature mechanical properties, 109

Tin alloys (Mo–Nb–Sn–Zr)
development for pressure-tube applications, 3–4
Tin alloys (Mo–Sn–Zr)
development for pressure-tube applications, 4
Tin systems (Mo–Nb–Si–Sn–Zr)
development for pressure-tube applications, 4
Titanium
cryogenic tensile properties of commercial 55A, effect of irradiation and postirradiation annealing on, 32
density, 118
diffusion of Be in, 120
diffusion in Hastelloy N, 121
solubility in liquid Bi–Pb alloys, 55
solubility in liquid Na, 149–50
thermal conductivity, 117
thermal expansion, 117
Titanium alloys
stress-corrosion cracking, 135
thermal–mechanical treatment of, DMIC review of Soviet literature on, 107
Titanium alloys (Al–Hf–Nb–Ta–Ti–W)
oxidation behavior, 114
Titanium alloys (Al–Sn–Ti)
tensile properties of irradiated, 32
Titanium alloys (Be–Ti)
powder metallurgy of, 83
Titanium alloys (Cr–Fe–Mo–Ni–Ti)
structure and properties of, effect of B additions on, 111
Titanium alloys (Cr–Fe–Ni–Ti)
stress-rupture properties of irradiated tubing of, 26–27
Titanium alloys (Cr–Ti–V)
compatibility with PuO_2–UO_2, 62
corrosion by liquid Na, 147
density, 118
thermal conductivity, 117
thermal expansion, 117
Titanium alloys (Mo–Ti)
protective coatings for, 141
siliconizing and boriding by reaction with $SiCl_2$ and BF vapors, 96–97
Titanium alloys (Nb–Ti)
corrosion in air, O_2, and N_2 at 650 to 1000°C, 47
corrosion in KOH, 47
protective coatings for, 140–41
Titanium alloys (Ti–W)
oxidation, 47
Titanium alloys (Ti–V)
corrosion by liquid Na, 147–48
density, 118
thermal conductivity, 117
thermal expansion, 117
Titanium boride (TiB_2)
electrodeposition onto Inconel, 90
Titanium carbide cermets (TaC–TiC–WC)
substitution of HfC and NbC for TaC in, 40
Titanium systems (Mo–Si–Ti)
development as protective coatings for Ta, 48
TRW-NASA IVY
longtime stability of carbide and intermetallic phases in, 9–10
TRW-NASA VIA
longtime stability of carbide and intermetallic phases in, 9–10
Tungsten
annealing of radiation damage in, 130
brazing of, alloy development for, 94–95
compatibility with molten U, 150
coupled with 304 stainless steel, development of Al_2O_3 and B_6Si diffusion barriers for, 18
coupled with Ir, Re, Rh, and Ta, interdiffusion studies of, 18
creep-rupture data compilation on, 17
deposition on expendable microspherical substrates to form thin-walled microballoons, 99
diffusion in Ta, 119
diffusion of H_2 into, 19–20
diffusion of Nb into, 119
diffusion of Ta into, 119
diffusion of U into, 19
grain size of vacuum-arc-cast, reduction by Mo addition, 116–17
grain structure and texture of sheets, effect of additions of ThO_2 on, 14–15
hot pressing of powders, 92
irradiation-induced swelling, effect of temperature and fluence on, 35
nitriding, effect of Hf content on, 117
oxidation, 140
sheets, preparation by vapor deposition of, 98
solubility in liquid K, 149–50
surface pores in, filling with W from the decomposition of $W(CO)_6$, 96
tensile fracture stress of equiaxed-grain polycrystalline wire, effect of temperature on, 15
thermoelectric properties, effect of irradiation on, 32
vapor deposition, 97–98
Tungsten alloys
corrosion by liquid Na, 52–53
creep-rupture data compilation on, 17
hot hardness of irradiated, 127
Tungsten alloys (Al–Hf–Nb–Ta–Ti–W)
oxidation behavior, 114
Tungsten alloys (Cr–Pd–W)
oxidation, 139
Tungsten alloys (Hf–W)
compatibility with molten U, 150
Tungsten alloys (Mo–Re–W)
corrosion by liquid Li, 54
nitriding, effect of Hf content on, 117
Tungsten alloys (Nb–W)
oxidation, 47
properties of, effect of small chemical additions on, 93
Tungsten alloys (Re–W)
compatibility with PuO_2–UO_2, 62
coupled with 304L stainless steel, development of Al_2O_3 and B_6Si diffusion barriers for, 18
nitriding, effect of Hf content on, 117
vapor deposition, 98
Tungsten alloys (Ta–W)
tensile properties of irradiated, 127, 129
Tungsten alloys (Ti–W)
oxidation, 47
Tungsten carbide
electrodeposition, 100
Tungsten carbide (WC)
grain growth at high temperature, 39
morphology of crystals of, 39
plastic properties, 39
recrystallization and sintering at high temperatures, 39
Tungsten carbide cermets (TaC–TiC–WC)
substitution of HfC and NbC for TaC in, 40
Tungsten carbide cermets (WC–Co)
fatigue behavior, effect of Co content on, 40
mechanical properties, dependence of carbide–carbide particle contacts on, 40
strength, theory of, 40
Tungsten cermets (W–UN)
irradiation studies, 70–71
Tungsten cermets (W–UO_2)
brazing with W–Os filler alloy, 95
irradiation studies, 70, 78
Tungsten powders
hot pressing of, 92
Tungsten systems (C–Hf–Re–W)
development for high-temperature applications, 14
TZC
creep-rupture properties, effect of fabrication variables on, 115
TZM
compatibility with fluoride salts, 151
coupled with 304 stainless steel, development of Al_2O_3 and B_6Si diffusion barriers for, 18
deformation and fracture behavior from 200 to 1850°C, 116
high-temperature creep data, 115–16
TZM alloys (Nb–TZM)
creep-rupture properties, effect of fabrication variables on, 115

U

U-700
longtime stability of carbide and intermetallic phases, 9–10
Ultrasonic testing, 101–2
Unitemp AF2-1D
longtime stability of carbide and intermetallic phases in, 9–10
Uranium
corrosion and protection of, British bibliography on, 72–73
diffusion into W, 19
ductile–brittle transitions in, effect of heat treatments on, 72
electrochemical machining, 101
electroless-nickel-plating methods for, 97
electroplating with Ni, 100
irradiation behavior, effect of dilute alloy additions and heat treatment on, 73
machining of, corrosion during, 72
roll-separating forces during rolling of, 93
Russian monograph on properties, metallurgy, and technology of, 72–73
Uranium (molten)
containment by W and Hf–W alloys, 150
Uranium-238
electrodeposition, 101
Uranium alloys
irradiation studies, 76
roll-separating forces during rolling of, 93
Uranium alloys (Cr–U)
properties, 74
viscosity of liquid, effect of Cr content on, 73
Uranium alloys (Fe–U)
diffusion of 304L stainless steel in, 118–19
Uranium alloys (Fe–U)
roll-separating forces during rolling of, 93
welding, hot cracking during, 94
Uranium alloys (Mo–U)
casting of cylinders of, 92
coring effects and homogenization methods in cast, 74
irradiation behavior, effect of Al and Sn additions on, 73
properties, 74

Uranium alloys (Nb–U)
properties, 74
Uranium alloys (Nb–U–Zr)
properties, 74
TTT diagram for, 73–74
Uranium alloys (Pu–U–Zr)
irradiation studies, 75
Uranium alloys (Th–U)
physical properties, 71–72
Uranium alloys (U–Zr)
properties, 74
Uranium carbide (UC)
coating with Nb, 99
coating with SiC, 99
diffusion of C in, 118
irradiation studies, 67–68, 78
plasma-flame melting, 66
preparation of high-density, French patent for, 65
preparation, sol-gel process for, 66
Uranium carbide systems (PuC_2–UC_2)
immiscibility, 65
Uranium carbide systems (PuC–UC)
irradiation studies, 66–67
Uranium carbide systems (Pu,U)C
compatibility with austenitic stainless steels, effect of Na bonding on, 65
pellet fabrication problems, 65
Pu volatilization from, 92
sintering, use of Ni and PuC as aids in, 66
Uranium carbide systems (Th,U)C_2
preparation, sol-gel process for, 66
Uranium carbide systems (UC–UN)
melting point, 68
Uranium carbides
bar fabrication by extrusion, French patents for, 65–66
irradiation studies, 76
Uranium nitride (UN)
evaporation, 69
fabrication, 69
irradiation studies, 69–70
reaction with Ru to form URu_3 and N_2, 68
Uranium nitride (U_2N_3)
properties, 68
Uranium nitride cermets (W–UN)
irradiation studies, 70–71
Uranium nitride systems (Cr–UN)
phase studies, 68
Uranium nitride systems (Nb–UN)
phase studies, 68
Uranium nitride systems (PuN–UN)
fabrication, 69
Uranium nitride systems ((Pu,U)N)
compatibility with stainless steel, 69
irradiation studies, 70
Uranium nitride systems (UC–UN)
melting point, 68
Uranium nitride systems (Ta–UN)
phase studies, 68
properties, 68
Uranium nitride systems (UN–V)
phase studies, 68
Uranium nitride systems (U_2N_3–UO_2)
isopleth of, 68
Uranium oxide (UO_2)
coating of particles with pyrolytic carbon, 99
diffusion of actinide elements in, 118
diffusion of O_2 in, from 885 to 1835°C, 61
irradiation studies, 62, 78
irradiation swelling, comparison of swaged and compacted, 61–62
preparation by compaction, effect of random wave vibration on density of, 61
preparation of sintered, British patent on, 61
preparation of sintered, French patent on, 61
reactions following loss-of-coolant accidents, 75–76
steam oxidation kinetics from 885 to 1835°C, 61
surface diffusion measurements in, 61
Uranium oxide (U_3O_8)
use of high-fired and burned as fuel materials, 71
Uranium oxide cermets (W–UO_2)
brazing with W–Os filler alloy, 95
irradiation studies, 70
Uranium oxide cermets (UO_2–W)
irradiation studies, 78
Uranium oxide systems (PuO_2–UO_2)
compatibility with Cr–Ti–V alloy, 62
compatibility with Cr–V alloy, 62
compatibility with Re–W alloy, 62
compatibility with 304 stainless steel, 62
O_2 migration in, from 1200 to 2000°C, 62
preparation of single-phase, sintering parameters for, 63
production of microspheres, sol-gel techniques for, 64
Uranium oxide systems (ThO_2–UO_2)
surface diffusion measurements in, 61
thermal conductivity from 20 to 500°C, 61
Uranium oxide systems (U_2N_3–UO_2)
isopleth of, 68
Uranium oxide systems (UO_2–Zr)
phase equilibra above 1600°C, 75
Uranium oxides
irradiation studies, 76
Uranium systems (C–U)
phase studies, 65
Uranium systems (Pu–U–O)
lower limit of PuO_2 concentration for the two-phase boundary in, 63–64
phase studies, 63
Uranium systems (Si–U)
roll-separating forces during rolling of, 93

V

Vanadium
chemical deposition onto Mo, 96
corrosion by liquid Na, 146–47
density, 117
deposition from VCl_4 and VF_5, 98–99
diffusion of C into, 19
diffusion of Fe into, isotope effect on, 120–21
electrorefining, 100
irradiation-induced swelling, effect of temperature and fluence on, 35
microhardness, 32
microhardness of irradiated, 32
O_2 and N_2 content of arc-melted, methods for reducing, 92
thermal conductivity, 117
thermal expansion, 117
vapor deposition, 98
void density and hardness of irradiated, effect of postirradiation annealing on, 127, 129
Vanadium alloys
corrosion by liquid Na, 52–53
hot hardness of irradiated, 127
mechanical and thermal properties, 117
Vanadium alloys (Cr–Mo–V)(Nb stabilized)
corrosion by liquid Na in contact with 316 stainless steel, 50
Vanadium alloys (Cr–Mo–V)(Ti stabilized)
corrosion by liquid Na in contact with 316 stainless steel, 50
Vanadium alloys (Cr–Mo–V)(Zr stabilized)
corrosion by liquid Na in contact with 316 stainless steel, 50
Vanadium alloys (Cr–Ti–V)
compatibility with PuO_2–UO_2, 62
corrosion by liquid Na, 147
density, 118
thermal conductivity, 117
thermal expansion, 117
Vanadium alloys (Cr–V)
compatibility with PuO_2–UO_2, 62
corrosion by liquid Na, 146
Vanadium alloys (Fe–V–Zr)
room-temperature mechanical properties, 109
Vanadium alloys (Nb–V–Zr)
development for pressure-tube applications, 3–4
Vanadium alloys (Ti–V)
corrosion by liquid Na, 147–48
density, 118
thermal conductivity, 117
thermal expansion, 117
Vanadium alloys (V–Zr)
beta–alpha transformation in, effect of V content on, 4
Vanadium carbide (VC)
mechanical properties of B doped, 39
Vanadium systems (UN–V)
phase studies, 68
Vanstar-9
corrosion by liquid Na, 146

W

Wah Chang 3015 alloy
oxidation behavior, 114
properties, 115
Waspaloy
longtime stability of carbide and intermetallic phases in, 9–10

X

Xenon-133
diffusion in CsI, 10

Y

Yttrium
corrosion by liquid Cr–U alloys, 55
Yttrium alloys (Al–Cr–Fe–Y)
mechanical properties, improvement by adding Mo, Nb, Ta, or W, 110
Yttrium alloys (Cr–Y)
oxidation, 47
Yttrium oxide (Y_2O_3)
elastic properties, 132–33

Z

Zinc alloys (Be–Cu–Zn)
aging characteristics of neutron irradiated, 34
Zinc alloys (Cd–Zn)
electrodeposition, 100–1
Zircaloy
orientation of hydride platelets in,

determination by microhardness impressions, 108
hydride precipitation in, effect of quenching temperature on, 108
in-pile creep of tubing, 36
in-pile deformation of, moded for, 21
mechanical properties of, effect of texture on, 107
Zircaloy-2
burst strength of tubes, effect of bending on, 2
corrosion in degassed deionized water at 232 to 316°C, 44
corrosion and hydriding behavior in H_2O at 340°C, 44
corrosion in NH_4OH water, 135
corrosion in steam, 137
corrosion in steam (D_2O) at 300 to 340°C, 44
corrosion in NPD Reactor, 135
crack propagation in tubing, 2
ductility, effect of H_2 on, 3
effect of thermal treatment on element distribution in, 2
embrittlement by exposure to steam, 108
fracture strength, effect of cold working, H_2 content, and irradiation on, 22–23
growth of oxide films on, morphology and mechanism of, 44
hardness of cold work, effect of irradiation and annealing temperature on, 22
hydride precipitation in, kinetics of, 3
in-pile steady-state creep rate of cold worked, 21–22
irradiation damage, annealing of, 23
mechanical properties of, 107
neutron-irradiation damage, 21–22
nonhomogeneous deformation of tubing, 2
stress-corrosion cracking in methanol solutions, 137–38
tensile properties, effect of H_2 on, 3
transformation and structure changes during continuous cooling, kinetics of, 107
weld cracks in, effect of H_2 on, 108
Zircaloy-4
corrosion in degassed deionized water at 232 to 316°C, 44
corrosion and hydriding behavior in H_2O at 340°C, 44
corrosion in the NPD Reactor, 135
corrosion in steam (D_2O) at 300 to 340°C, 44
high-temperature deformation and burst characteristics of recrystallized tubes of, 108
mechanical properties of, 107
texture of tubing, effect of fabrication processes on, 93
Zirconium
coatings of, production from mixed iodide vapors, 96
corrosion, book on, 137
corrosion by liquid Na, 52
diffusion of Be in, 120
growth of oxide films on, morphology and mechanism of, 44
hydride platelets in, habit planes of, 1
in-pile creep, effect of additions of rare earths, 21
prismatic slip in hexagonal close packed, 1
solubility of Al in, 109
solubility of C in beta phase, 2
solubility in liquid Bi–Pb alloys, 55
stress-corrosion cracking in methanol solutions, 137–38
yield strength, effect of H_2 on, 1
Zirconium alloys
corrosion, book on, 137
development for use in pressurized water, boiling water, or CO_2, 5
Zirconium alloys (Al–Mg–Zr)
phase diagram, 1
Zirconium alloys (Al–Mo–Nb–Sn–Zr)
development for pressure-tube applications, 4
Zirconium alloys (Al–Mo–Zr)
development for pressure-tube applications, 3–4
Zirconium alloys (Be–Zr)
powder metallurgy of, 83
Zirconium alloys (B–Zr)
annealing of irradiated, 129
Zirconium alloys (Cr–Fe–Zr)
ductility, effect of autoclaving on, 23
ductility, effect of irradiation on, 23
room-temperature mechanical properties, 109
tensile strength, effect of autoclaving on, 23
tensile strength, effect of irradiation on, 23
Zirconium alloys (Cr–Zr)
hardness of temperature aged, effect of Cr content on, 4
Zirconium alloys (Cu–Fe–Zr)
hydrogen absorption and embrittlement resistance of, 4
Zirconium alloys (Cu–Nb–Zr)
mechanical properties of, 107
stress-corrosion cracking in methanol solutions, 137–38
Zirconium alloys (Fe–Ni–Nb–Sn–Zr)
room-temperature mechanical properties, 109
Zirconium alloys (Fe–V–Zr)
room-temperature mechanical properties, 109
Zirconium alloys (Mg–Pb–Zr)
use as fuel-element can, 1
Zirconium alloys (Mo–Nb–Sn–Zr)
development for pressure-tube applications, 3–4
Zirconium alloys (Mo–Sn–Zr)
development for pressure-tube applications, 4
Zirconium alloys (Nb–Ta–Zr)
room-temperature mechanical properties, 109
Zirconium alloys (Nb–U–Zr)
properties, 74
TTT diagram for, 73–74
Zirconium alloys (Nb–V–Zr)
development for pressure-tube applications, 3–4
Zirconium alloys (Nb–Zr)
corrosion by fluoride salts, 151
corrosion by liquid Hg, 53
corrosion by liquid Na, 53
corrosion by Li–K vapor, 148
corrosion by steam, effect of irradiation on, 137
corrosion in the NPD Reactor, 135
crystallographic texture after rolling at several temperatures, 93
development for pressure-tube applications, 4
effect of changing the corrosive medium from 200 atm of steam to 1 atm of air on oxidation of, 44
fatigue-crack growth and propagation in pressure tubing, 6–7
mechanical properties of, 107
mechanical properties and structure of, effect of internal oxidation on, 16
performance in high-temperature steam, effect of irradiation on, 3–4
postirradiation deformation, effect of irradiation temperature on, 23
stress-corrosion cracking in methanol solutions, 137–38
stress-rupture properties, effect of internal oxidation on, 16
stress-rupture properties of pressure tubes, 5–7
structural transformation in, 109
tensile strength, effect of O_2 content, Nb content, and cold working on, 5–6
texture of, effect of rolling temperature on, 109
Zirconium alloys (Pu–U–Zr)
irradiation studies, 75
Zirconium alloys (Pu–Zr)
delta stabilized, chemical diffusivities of, 118
Zirconium alloys (U–Zr)
properties, 74
Zirconium alloys (V–Zr)
beta–alpha transformation in, effect of V content on, 4
Zirconium boride (ZrB_2)
bend strength of hot pressed, 90
Zirconium carbide (ZrC)
vapor deposition of, 97
Zirconium couples (C–Zr)
diffusion studies, 121
Zirconium hydrides
compressive deformation, 87
deformation behavior and fracture of, 86–87
fracture of, 87
Zirconium oxide (ZrO_2)
erosion in gas streams at high temperatures, 40
mechanical stability, effect of percentage of monoclinic phase on, 40
plasticity, enhancement of during monoclinic to tetragonal transformation, 40
thermal shock resistance of partially stabilized, theory of improvement of, 40
Zirconium systems (H–Zr)
phase studies, 86
Zirconium systems (Mo–Nb–Si–Sn–Zr)
development for pressure-tube applications, 4
Zirconium systems (UO_2–Zr)
phase equilibra above 1600°C, 75

AEC SYMPOSIUM SERIES

Available for $3.00 each from the Clearinghouse for Federal Scientific and Technical Information, National Bureau of Standards, U. S. Department of Commerce, Springfield, Virginia 22151

1 **Progress in Medical Radioisotope Scanning (TID-7673)**
Oak Ridge Institute of Nuclear Studies, 1963

2 **Reactor Kinetics and Control (TID-7662)**
The University of Arizona, 1964

3 **Dynamic Clinical Studies with Radioisotopes (TID-7678)**
Oak Ridge Institute of Nuclear Studies, 1964

4 **Noise Analysis in Nuclear Systems (TID-7679)**
University of Florida, 1964

5 **Radioactive Fallout from Nuclear Weapons Tests (CONF-765)**
U. S. Atomic Energy Commission, 1965

6 **Radioactive Pharmaceuticals (CONF-651111)**
Oak Ridge Institute of Nuclear Studies, 1966

7 **Neutron Dynamics and Control (CONF-650413)**
The University of Arizona, 1966

8 **Luminescence Dosimetry (CONF-650637)**
Stanford University, 1967

9 **Neutron Noise, Waves, and Pulse Propagation (CONF-660206)**
University of Florida, 1967

10 **Use of Computers in Analysis of Experimental Data and the Control of Nuclear Facilities (CONF-660527)**
Argonne National Laboratory, 1967

11 **Compartments, Pools, and Spaces in Medical Physiology (CONF-661010)**
Oak Ridge Associated Universities, 1967

12 **Thorium Fuel Cycle (CONF-660524)**
Oak Ridge National Laboratory, 1968

13 **Radioisotopes in Medicine: In Vitro Studies (CONF-671111)**
Oak Ridge Associated Universities, 1968

14 **Abundant Nuclear Energy (CONF-680810)**
Oak Ridge Associated Universities, 1969

15 **Fast Burst Reactors (CONF-690102)**
American Nuclear Society, 1969

16 **Biological Implications of the Nuclear Age (CONF-690303)**
Lawrence Radiation Laboratory, 1969

17 **Radiation Biology of the Fetal and Juvenile Mammal (CONF-690501)**
Battelle Memorial Institute, 1969

18 **Inhalation Carcinogenesis (CONF-691001)**
Oak Ridge National Laboratory, 1970

19 **Myeloproliferative Disorders of Animals and Man (CONF-680529)**
Battelle Memorial Institute, 1970

20 **Medical Radionuclides: Radiation Dose and Effects (CONF-691212)**
Oak Ridge Associated Universities, 1970

☆ U.S. GOVERNMENT PRINTING OFFICE: 1970—436194/1

Nuclear Science Abstracts

The U. S. Atomic Energy Commission, Division of Technical Information, publishes *Nuclear Science Abstracts (NSA)*, a semimonthly journal containing abstracts of the literature of nuclear science and engineering.

NSA covers (1) research reports of the U. S. Atomic Energy Commission and its contractors; (2) research reports of government agencies, universities, and industrial research organizations on a worldwide basis; and (3) translations, patents, books, and articles appearing in technical and scientific journals.

Complete indexes covering subject, author, source, and report number are included in each issue. These indexes are cumulated and sold separately.

Availability of NSA

SALE *NSA* is available on subscription from the Superintendent of Documents, U. S. Government Printing Office, Washington, D. C. 20402, at $42.00 per year for the semimonthly abstract issues and $38.00 per year for the cumulated-index issues. Subscriptions are postpaid within the United States, Canada, Mexico, and all Central and South American countries, except Argentina, Brazil, Guyana, French Guiana, Surinam, and British Honduras. Subscribers in these Central and South American countries, and in all other countries throughout the world, should remit $52.50 per year for subscriptions to semimonthly abstract issues and $47.50 per year for the cumulated-index issues. The single-copy price for the abstract issues is $1.75 postpaid, with this exception: Add one-fourth of $1.75 for mailing to the countries to which the $52.50 subscription rate applies.

EXCHANGE *NSA* is also available on an exchange basis to universities, research institutions, industrial firms, and publishers of scientific information. Inquiries should be directed to the Division of Technical Information Extension, U. S. Atomic Energy Commission, P. O. Box 62, Oak Ridge, Tennessee 37830.

TECHNICAL PROGRESS REVIEWS may be purchased from Superintendent of Documents, U. S. Government Printing Office, Washington, D. C. 20402. *Nuclear Safety* at $3.50 per year (six issues) for each subscription or $0.60 per issue; *Reactor Technology* at $3.00 per year (four issues) for each subscription or $0.75 per issue; *Isotopes and Radiation Technology* at $2.50 per year (four issues) or $0.70 per issue. The use of the order form below will facilitate the handling of your order.

POSTAGE AND REMITTANCE: Postpaid within the United States, Canada, Mexico, and all Central and South American countries except Argentina, Brazil, Guyana, French Guiana, Surinam, and British Honduras. For these Central and South American countries and all other countries: add, for each annual subscription, $1.00 for *Nuclear Safety* and $0.75 for each of the other journals; for single issues, add one-fourth of the single-issue price. Payment should be by check, money order, or document coupons, and MUST accompany order. Remittances from foreign countries should be made by international money order or draft on an American bank payable to the Superintendent of Documents or by UNESCO book coupons.

order form

SUPERINTENDENT OF DOCUMENTS
U. S. GOVERNMENT PRINTING OFFICE
WASHINGTON, D. C. 20402

Please send — 1, 2, or 3 years

- ☐ Isotopes and Radiation Technology ____
- ☐ Nuclear Safety ____
- ☐ Reactor Technology ____

Enclosed: document coupons ☐ check ☐ money order ☐

Charge: Superintendent of Documents No. _____

SUPERINTENDENT OF DOCUMENTS
U. S. GOVERNMENT PRINTING OFFICE
WASHINGTON, D. C. 20402

(Print clearly)

_____
Name

_____
Street

_____
City, State, ZIP Code